Electronic Correlations in Li_xCoO_2

By

Chris A Marianetti

Submitted to the Department of Materials Science and Engineering in partial fulfillment of the requirements for the degree of

Doctor of Philosophy in Materials Science and Engineering

at the

MASSACHUSETTS INSTITUTE OF TECHNOLOGY

[February 2004]
January 2004

Author..... 1/29/2004

Department of Materials Science and Engineering
January 29th, 2004

Certified by..... Jan 29, 2004

Gerbrand Ceder
R.P. Simmons Professor of Computational Materials Science
Thesis Supervisor

Accepted by.....

Harry L. Tuller
Professor of Ceramics and Electronic Materials
Chairman, Department Committee on Graduate Students

Electronic Correlations in Li_xCoO_2

by

Chris Marianetti

Submitted to the Department of Materials Science and Engineering on 1/26/2004 in partial fulfillment of the requirements for the degree of Doctor of Philosophy in Materials Science and Engineering

Abstract

The purpose of this thesis is further the understanding of the electronic properties of Li_xCoO_2 using density functional theory (DFT) and the dynamical mean-field theory (DMFT). Three main problems are addressed. First, the influence of hybridization among the e_g and oxygen orbitals is studied using DFT and a modified Hubbard model which is solved within DMFT. It has long been known that doping holes into the t_{2g} bands are accompanied by a rehybridization which causes electron density to be added to the e_g states and hole density to the oxygen states. This so-called rehybridization mechanism has been demonstrated to be a *competition* between the hybridization, which prefers to occupy the e_g orbitals, and the Co on-site coulomb repulsion, which prefers to have the e_g orbitals empty to avoid the strong coulomb interaction. It is also shown that e_g-oxygen hybridization effectively screens the low energy t_{2g} excitations, which has implications for the low energy Hamiltonian corresponding to hydrated $Na_{1/3}CoO_2$. Second, the hereto anomalous first-order metal-insulator transition in Li_xCoO_2 ($0.75 < x < 0.95$) is identified as a Mott transition of impurity states. DFT supercell calculations indicate that for dilute Li vacancy concentrations (ie $x > 0.95$), the vacancy potential binds its hole and forms an impurity state which leads to a Mott insulator. We argue that the first-order transition is due to a decomposition of the impurity band, and is perhaps the only known example of a first-order Mott transition in a doped semiconductor. Third, $LiCoO_2$ possesses a high energy photoemission satellite which hereto could not be predicted by any first-principles method. LDA+DMFT solved within multi-band iterated perturbation theory successfully predicts the satellite.

Thesis Supervisor: Gerbrand Ceder
Title: R.P. Simmons Professor of Computational Materials Science

Acknowledgements

Thanks to the many people who helped me along this journey.

Contents

Chapter 1

Strong Electronic Correlation in Transition-metal Oxides

Transition-metal oxides (TMO) are an important class of materials both from a fundamental and a technological perspective. Technologically, TMO are used as magnetic materials, ferroelectrics, battery cathodes, and many other specialized applications. The material studied within this thesis, $LiCoO_2$, is the predominant material used in rechargeable Li batteries, and thus it has a significant presence in everyday life by powering cell phones and laptop computers. From a more fundamental point of view, TMO play host to some of the more interesting theoretical topics within condensed matter physics, such as high-temperature superconductivity and collosal magneto-resistance. Therefore, it is important to have a fundamental understanding of the electronic structure of TMO.

In any given material, one is faced with a complicated many-body problem which must be solved in order to understand the behavior of the electrons. However, the TMO are particularly challenging given that the valence bandwidth is comparable or smaller than the electron-electron interactions. Therefore, the lowering of the kinetic energy which may be achieved via delocalization is comparable to the gain in energy due to the resulting electron-electron interactions. This is the so-called "strongly correlated" regime, and many standard electron structure tools fail within this regime. Specifically, density functional theory (DFT) within any known approximation tends to fail qualitatively when the correlation becomes too strong. DFT used within the local density approximation (LDA) or the generalized gradient approximation (GGA) has emerged as the primary tool to study the electronic structure of real materials. Although the LDA and the GGA are now rather old developments, there does not yet appear to be new approximations for the exchange-correlation potential which will allow DFT to successfully treat materials with

strong electronic correlations. Therefore, new methods are required in order to treat realistic materials with strong electronic correlations, such as the dynamical mean-field theory (DMFT). The DMFT is a powerful approximation which has been used to reliably solve lattice models, such as the Hubbard model, for essentially any degree of electronic correlation. Additionally, the DMFT has been merged with the LDA in order to more accurately treat strong correlation within TMO. This new approach has already proven successful in describing strongly correlation in TMO, and in this thesis we use DMFT in conjunction with LDA to further the understanding of the electronic properties of $LiCoO_2$.

Chapter 2

Introduction to the Many-Body Problem

2.1 Introduction

In this section, we attempt to cover the highlights of many-body physics which are pertinent to understanding electronic correlations[1-4]. The goal is to give a feeling for why the many-body problem is difficult, and what mathematical tools are typically used in studying the many-body problem. We begin by discussing how the Hamiltonian is diagonalized for the single-body and many-body case, illustrating the inherent difficulties in diagonalizing the many-body problem and motivating the use of Greens functions. Second quantization and the Fock space are then introduced, as they are standard mathematical tools used in the many-body problem. The Hubbard model, which might be considered the "standard model" of strongly correlated electrons, is introduced and discussed. A summary of many-body Greens functions, Dysons equation, and Feynman diagrams is given. Finally, a short discussion of density functional theory is given.

2.2 The Many-Body Hamiltonian

A many-body problem is one in which the Hamiltonian contains terms that couple the coordinates of multiple particles. Much of modern physics is concerned with solving some sort of many-body problem. Within condensed matter physics, interactions among the electrons, the phonons, and between the electrons and phonons all give rise to many-body problems. Within this thesis, the focus is primarily upon the electronic degrees of freedom, and the many-body problem of interest arises from the electron-electron interactions. More specifically, it is assumed that the electron and phonon degrees of freedom may be decoupled using the Born-Oppenheimer approximation[5, 6], resulting in the following electronic Hamiltonian (equation 1):

$$\hat{H} = \sum_{i=1}^{N}\left(\frac{\hat{p}_i^2}{2m} + V(\hat{r}_i)\right) + \sum_{\langle i,j\rangle}^{N}\frac{e^2}{\hat{r}_i - \hat{r}_j} \qquad (1)$$

where m is the mass of the electron, N is the number of particles in the system, e is the charge on the electron, $\hat{r}$ is the position operator for the electron, $\hat{p}$ is the momentum operator for the electron, and V is the potential due to the static nuclei. The first two terms of the Hamiltonian are the kinetic energy of the electrons and the potential energy due to the nuclei. Both of these terms are one-body terms in that each term only involves the coordinates of one electron. The third term is the electron-electron interaction and this is a many body term because it involves the coordinates of two electrons. Defining the commutation relations in equation 2, a specific representation for the operators may be chosen and the Hamiltonian may be written as a differential equation.

$$\left[\hat{r}_i, \hat{p}_j\right] = \hbar i \delta_{ij} \qquad (2)$$

In general, this Hamiltonian is insolvable, and the details of this assertion shall be discussed in depth.

2.3 Solving the One-Body Problem

For certain one-body Hamiltonians, such as the central field or positive background, analytic solutions may be found, and these few cases are exactly solvable. However, for a general one-body Hamiltonian, analytic solutions may not be obtained and computational techniques must be used to solve the Hamiltonian. Perhaps the most common computational procedure is to represent the Hamiltonian in some complete basis set (equation 3) and diagonalize the Hamiltonian, yielding the exact eigenvalues and the exact eigenvectors as some linear combination of the complete basis states.

$$\{|a_1\rangle \ldots |a_n\rangle\} \qquad (3)$$

$$\hat{H} = \sum_{i,j}|a_i\rangle\langle a_i|\hat{H}|a_j\rangle\langle a_j| = \sum_i |e_i\rangle\langle e_i|\hat{H}|e_i\rangle\langle e_i| \qquad (4)$$

In reality, a complete basis set can rarely be used, and the basis set must be truncated such that the Hamiltonian matrix can be diagonalized using some computational

technique. Therefore, one might suggest that *technically* even most one-body problems cannot be solved exactly. However, monitoring the convergence of the solution with respect to the truncation of the basis set will demonstrate when the problem has been solved for practical purposes. Additionally, clever basis sets have been developed, such as FLAPW and LMTO, which are efficient and allow the Hamiltonian to be diaganolized easily[7]. It should be clear that our ability to solve one-body problems directly relies on available computational resources. In the early days of electronic structure (ie. ~1930s), solving even a simple one-body problem with one atom per unit cell, such as Na metal, was a major computational feat due to the primitive state of computation[8]. In the present day, far more complicated one-body problems may be solved. For example, in this thesis a calculation is performed for an effective one-body problem with 512 atoms per unit cell. This dramatic difference is the result of the exponential manner in which computer speed grows with time.

2.4 Solving the Many-Body Problem

The many-body problem is far more difficult to solve than the one-body problem, and even fewer situations arise when an analytical solution is possible. Even in these special situations, usually only certain aspects of the solution may be obtained. In order to illustrate the difficulties of the many-body problem we shall follow the same approach as in the one-body problem and represent the Hamiltonian in a truncated basis and diagonalize it. The first step is to create a proper N-particle Hilbert space. In order to do this, a truncated single particle basis set must first be chosen.

$$\{|a_1\rangle \ldots |a_n\rangle\} \tag{5}$$

Each N-particle base state must be a product of N single-particle base states. For example, if a 3 electron problem was being solved, a few possible 3 particle base states are the following:

$$|a_1\rangle|a_2\rangle|a_3\rangle \qquad |a_1\rangle|a_5\rangle|a_7\rangle \tag{6}$$

Additionally, the *N*-particle base state must be constructed such that it is antisymmetric under the exchange of two electrons (ie. Fermi statistics). The first state given in equation 6 is antisymmetrized as follows.

$$|a_1a_2a_3\rangle = \frac{1}{\sqrt{6}}\left[|a_1\rangle|a_2\rangle|a_3\rangle + |a_2\rangle|a_3\rangle|a_1\rangle + |a_3\rangle|a_1\rangle|a_2\rangle - |a_1\rangle|a_3\rangle|a_2\rangle - |a_2\rangle|a_1\rangle|a_3\rangle - |a_3\rangle|a_2\rangle|a_1\rangle\right] \quad (7)$$

If we project this state onto the position representation, we arrive at the familiar Slater determinant.

$$\langle x_1|\langle x_2|\langle x_3||a_1a_2a_3\rangle = \Psi_{a_1a_2a_3}(x_1,x_2,x_3) = \frac{1}{\sqrt{6}}\begin{vmatrix} \psi_{a_1}(x_1) & \psi_{a_2}(x_1) & \psi_{a_3}(x_1) \\ \psi_{a_1}(x_2) & \psi_{a_2}(x_2) & \psi_{a_3}(x_2) \\ \psi_{a_1}(x_3) & \psi_{a_2}(x_3) & \psi_{a_3}(x_3) \end{vmatrix} \quad (8)$$

$$\psi_{a_1}(x_1) = \langle x_1|a_1\rangle \quad (9)$$

In order to make the *N*-particle basis set complete, all possible permutations of antisymmetric products of *N* single-particle base states must be constructed. In other words, all possible *N*-particle Slater determinants must be constructed. If we define *n* as the number of single particle basis states we have retained, the number of *N* particle base states is $\frac{n!}{N!(n-N)!}$. Clearly, even for small *N* and *n*, there may be an enormous number of *N*-particle base states. In order to fully appreciate this, an example comparing an interacting versus noninteracting problem is in order. Consider a Nitrogen molecule and a truncated atomic basis set including *1s, 2s, 2p,* and *3s* states. If electron interaction were neglected, the Hamiltonian would be a 12x12 matrix. If interactions were included and we constructed all possible *N*-particle base states for the given truncated single-particle basis, the Hamiltonian would be a 792x792 matrix! Symmetry could be used to reduce the number of independent elements in both cases, however the point is that creating a Hilbert space for a many particle problem requires far more states than the for the single particle problem. This simple example illustrates the root of why "brute force" cannot be used on the many-body problem once any degree of sophistication is present. It should also be pointed out that this is not merely a practical limit. Using simple estimates, Van Vleck and others have shown that the wavefunction for a system of on the order 1000 electrons is not even a "scientifically legitimate concept"[9]. They estimate that the wavefunction for such a system would contain more bits than there are particles in the

universe! Barring any fundamental changes in our understanding of physics and/or information theory, such a problem will never be managed by "brute force". However, we shall explain below that this is not necessarily a serious problem, given that knowledge of the many-particle wave functions is not necessary for much of what one would like to know about the many-body problem.

2.5 Second Quantization

When dealing with a many-body problem, it is extremely useful to introduce the concepts of second quantization and the Fock space[4]. We shall begin by attempting to give insight into what a Fock space is. In the one-body problem, the familiar Hilbert space is used to represent the Hamiltonian. In our above example of a many-body problem, we use antisymmetric products of single particle states to create an N-particle Hilbert space. Therefore, both the Hilbert space and the Hamiltonian explicitly depend on the number of particles in the system. This is inconvenient when studying an open system, and it would be helpful to have a representation of the Hamiltonian which is general to any number of particles. This is the purpose of the Fock space and second quantization in the many-body problem. Mathematically, the Fock space is defined as the direct sum of all possible antisymmetric Hilbert spaces.

$$F = H_0 \oplus H_1 \oplus H_2 \oplus \ldots \tag{10}$$

H_N denotes the Hilbert space for a N-particle system. Within the Fock space, any base state may be represented by the so called raising and lowering operators. There action upon the vacuum (the state with no particles) may be defined as follows.

$$c_{a_1}^{\dagger}|0\rangle = |a_1\rangle \qquad c_{a_1}|a_1\rangle = |0\rangle \tag{11}$$

The operator $c_{a_1}^{\dagger}$ creates a particle in the single particle base state a_1, while the operator c_{a_1} destroys a particle in the single-particle base state a_1. Just as the position and momentum operators are related via commutation relations, the raising and lowering operators are related with anit-commutation relations.

$$\left\{c_j, c_i^{\dagger}\right\} = c_i^{\dagger}c_j + c_j c_i^{\dagger} = \delta_{ij} \tag{12}$$

$$\left\{c_j, c_i\right\} = 0 \tag{13}$$

$$\left\{c_j^\dagger, c_i^\dagger\right\} = 0 \tag{14}$$

These anti-commutation relations ensure that the many-particle state is anti-symmetric under exchange of two electrons. To give an example, we shall build the anti-symmetric three-particle state in equation 7, and demonstrate that it is anti-symmetric under exchange using equation 14.

$$\left|a_1 a_2 a_3\right\rangle = c_{a_1}^\dagger c_{a_2}^\dagger c_{a_3}^\dagger \left|0\right\rangle = -c_{a_2}^\dagger c_{a_1}^\dagger c_{a_3}^\dagger \left|0\right\rangle = -\left|a_2 a_1 a_3\right\rangle \tag{15}$$

Within the Fock space, any operator may also be represented by the raising and lowering operators. For example, take the total kinetic energy operator from equation 1.

$$\sum_{i=1}^{N} \frac{\hat{p}_i^2}{2m} = \sum_{kl} \langle k | \frac{\hat{p}^2}{2m} | l \rangle C_k^\dagger C_l \tag{16}$$

We see that the original operator explicitly depends on the number of particles, while the second quantized form is simply a sum over the indices *k,l* which go over all the elements of some complete single-particle basis. Also, we note that kinetic energy is a single particle operator and the corresponding second quantized operator is *quadratic* in the raising and lowering operators. Considering the electron-electron interactions from equation 1, the corresponding second quantized operator is *quartic* in the raising and lowering operators.

$$\frac{1}{2} \sum_{i=1, j=1}^{N} \frac{e^2}{\hat{r}_i - \hat{r}_j} = \sum_{klmn} \langle kl | \frac{e^2}{\hat{r}_1 - \hat{r}_2} | mn \rangle C_k^\dagger C_l^\dagger C_n C_m \tag{17}$$

To conclude, second quantization and the Fock space may be used to represent a many-body problem with an arbitrary number of particles. The anti-symmetry of the many-electron state is automatically accounted for via the anti-commutation relations which the raising and lowering operators satisfy.

2.6 Introducing the Hubbard Model

The Hubbard model is the standard approach which is used to model strongly correlated electrons. It was introduced independently by Kanamori[10], Gutzwiller[11], and Hubbard[12, 13]. All three authors proposed different approximations to solve the Hubbard

model, and each approximation is tailored to a different aspect of the model. The one-band Hubbard model is defined as follows:

$$H = \sum_{ij\sigma} t_{ij} C_{i\sigma}^{\dagger} C_{j\sigma} + \sum_{i} U C_{i\downarrow}^{\dagger} C_{i\downarrow} C_{i\uparrow}^{\dagger} C_{i\uparrow} \tag{18}$$

where the operator C creates an electron in some localized basis orbital, which for example might be an atomic orbital or a Wannier orbital. The indices i,j run over all the sites of the lattice, and σ is the spin index which takes on values of $\uparrow$ and $\downarrow$. The hopping parameters t_{ij} encompass all the one body operators such as the potential of the crystal and the kinetic energy of the electrons. The first term of the Hamiltonian transfers an electron from one site to another. The parameter U is the coulomb interaction between electrons on a given site. The second term is simply a product of the number operators for the up and down electrons on a given site ($\hat{n}_{\sigma} = C_{\sigma}^{\dagger} C_{\sigma}$), and a coulomb interaction of U is felt if both spins are occupied. It should be understood that the Hubbard model is a *minimal* model of strongly correlated electrons. For example, in a more realistic model there will be a coulomb repulsion between electrons on neighboring sites, but this will be smaller than the on-site repulsion and therefore it is neglected. Also, in a model of any realistic material there would be other types of states which hybridize and interact with the correlated states, but these are also left out or treated in some effective manner.

2.7 A modified Hubbard model

There are many variants of the Hubbard model which restore certain aspects of a more realistic Hamiltonian. In this thesis, we introduce a two-band Hubbard model, which also includes oxygen-like orbitals, in order to mimic the relevant physics of Li_xCoO_2 with the simplest possible model. In an effort to familiarize the reader with second quantized Hamiltonians, we shall discuss this model in detail.

$$\begin{aligned} H = & \sum_{i,\sigma} \left[\varepsilon_p p_{i,\sigma}^{\dagger} p_{i,\sigma} + \varepsilon_e e_{i,\sigma}^{\dagger} e_{i,\sigma} + T_{p-e} \left(e_{i,\sigma}^{\dagger} p_{i,\sigma} + p_{i,\sigma}^{\dagger} e_{i,\sigma} \right) \right] + \sum_{i,j,\sigma} w_{i,j} t_{i,\sigma}^{\dagger} t_{j,\sigma} \\ & + U \sum_{i,\sigma} \left[e_{i,\sigma}^{\dagger} e_{i,\sigma} t_{i,\sigma}^{\dagger} t_{i,\sigma} + t_{i,\uparrow}^{\dagger} t_{i,\uparrow} t_{i,\downarrow}^{\dagger} t_{i,\downarrow} + e_{i,\uparrow}^{\dagger} e_{i,\uparrow} e_{i,\downarrow}^{\dagger} e_{i,\downarrow} \right] - \mu \sum_{i,\sigma} \left[p_{i,\sigma}^{\dagger} p_{i,\sigma} + e_{i,\sigma}^{\dagger} e_{i,\sigma} + t_{i,\sigma}^{\dagger} t_{i,\sigma} \right] \end{aligned} \tag{19}$$

This model contains three non-degenerate spin orbitals (p, t, e) which can be analogously thought of as the oxygen p orbitals, the transition metal t_{2g} orbitals, and the

transition metal e_g orbitals. The respective annihilation operators are denoted as *p, e,* and *t*. Let us first concentrate on the unperturbed portion of the Hamiltonian which is the top line of equation 19. The *e* and *p* orbitals are clearly localized with energies ε_e and ε_p, respectively, given that there is no operator which transfers an electron from an *e* orbital on a given site to another site. However, there is an operator which allows the electron to hop from the *e* orbital to the *p* orbital *within* a given site, and this is simply the hybridization. Alternatively, the *t* orbitals are allowed to hop as indicated by the last term on the first line which transfers a *t* electron from one site to another. The first term on the second line is the on-site coulomb repulsion among the *t* and *e* electrons. The last term is equal to $-\mu\hat{N}$, where μ is the chemical potential and $\hat{N}$ is the *total* number of particles in the system. This is simply a legendre transform of the Hamiltonian to a grand canonical ensemble which is a function of μ as opposed to $\hat{N}$, and this is done as a matter of convenience.

2.8 The Anderson Impurity Model

Below it will be demonstrated that the Hubbard model in the limit of infinite spatial dimensions is actually equivalent to an Anderson impurity model (AIM) [14].

$$H_{AIM} = \sum_{k\sigma} \varepsilon_k c_{k\sigma}^{\dagger} c_{k\sigma} + \sum_{k\sigma} V_k \left(c_k^{\dagger} d_{\sigma} + d_{\sigma}^{\dagger} c_k \right) + U d_{\uparrow}^{\dagger} d_{\uparrow} d_{\downarrow}^{\dagger} d_{\downarrow} \qquad (20)$$

The AIM corresponds to a model with a *single* correlated site, *d*, which hybridizes with band electrons, *k*. The band electrons have some dispersion, ε_k, and they may hop onto the correlated site via the matrix element V_k. The last term is the familiar coulomb interaction for the *single* correlated site. Within DMFT, the parameters ε_k and V_k define the effective electron bath which emulates lattice. The AIM is a nontrivial many body problem, but it may be solved nearly exactly using numerical techniques.

2.9 Greens Functions

Above we demonstrated that the number of basis functions in a many-particle system grows rapidly and that diagonalizing the Hamiltonian is often not possible.

Additionally, we discussed the Van Vleck catastrophe, or the fact that the many-particle wave function itself is not tractable once the number of particles becomes appreciable. In the general case we will need a methodology which does not require direct knowledge of the many-particle wave function. Therefore, we shall study the many-particle Greens function, which in general only depends on two sets of electron coordinates and not *N*. The Greens function is a mathematical object which contains much of the information regarding the many-particle system that we would like to know[1]. The ground state energy and the expectation value of any single-particle operator may be determined from the Greens function. The eigenvalues of the *N* particle system may *not* be determined from the Green's function, but the eigenvalues of the N-1 and N+1 particle system are given by the poles of the Greens function. Knowledge of the eigenvalues of the *N*+1 and *N*-1 particle system is useful considering that these are directly probed in photoemission and inverse photoemission experiments.

2.9.1 Definition

The Greens function is defined in *kt*-space as follows:

$$G(k;t_1,t_2) = -i\langle\phi|T\left[c_k(t_2)c_k^{\dagger}(t_1)\right]|\phi\rangle \tag{21}$$

where $|\phi\rangle$ is the exact many-particle ground state vector, $c_k^{\dagger}(t)$ destroys a particle in the state *k* and time *t*, and *T* is an operator which orders the raising and lowering operators such that the earliest time stands to the right . A simple interpretation of the Greens function can be given. At t_1, an electron is added to the ground state in the state *k* via the creation operator. At t_2, an electron in state *k* is removed from the system via the destruction operator. Finally, the resulting state is projected back onto the ground state of the system. Therefore, the greens function is the probability amplitude of adding a particle in the state *k* at time t_1 to the ground state, and then observing the system in the ground state with an added particle in state *k* at time t_2. The Greens function can also be defined in real space as opposed to *k* space

$$G(x_1,t_1;x_2,t_2) = -i\langle\phi|T\left[\psi(x_2,t_2)\psi^{\dagger}(x_1,t_1)\right]|\phi\rangle \tag{22}$$

where $\psi^{\dagger}(x,t)$ creates a particle at position x and time t. An analogous physical interpretation can be given as above.

An important point to notice is that the Greens function is simply the expectation value of a creation and annihilation operator. Above we noted that it was convenient to represent all operators in terms of creation and annihilation operators, and therefore the expectation value of the creation and annihilation operators are needed to determine the expectation value of some arbitrary operator. Given that any single-particle operator is quadratic in the creation and annihilation operator, the expectation value of all single-particle operators in the ground state are known once the Greens function is known. Although not obvious, the expectation value of the product of two creation and two annihilation operators may also be found from the Greens function for certain situations. This allows the total ground state energy to be determined from the Greens function. For example, we give the density in terms of the real space Greens function (equation 23), and the functional relation between the total ground state energy and the real space Greens function (equation 24).

$$\rho(r) = -iG(x,t_1;x,t_1^+) \tag{23}$$

$$E = -i\int dx \lim_{t'\to t^+} \lim_{x'\to x}\left[i\hbar\frac{\partial}{\partial t} - \frac{\hbar^2\nabla^2}{2m}\right]G(x,t;x',t') \tag{24}$$

2.9.2 Lehmann Representation

Much insight can be gained by fourier transforming the greens function to the frequency domain and performing additional manipulations in order to attain the so-called spectral or Lehmann representation.

$$G(k,\omega) = \int d\varepsilon\left[\frac{A(k,\varepsilon)}{\omega-\varepsilon+\mu+i\delta} + \frac{B(k,\varepsilon)}{\omega+\varepsilon+\mu-i\delta}\right] \tag{25}$$

$$A(k,\varepsilon) = \sum_j \left|\langle\phi_{N-1,j}|c_k|\phi_N\rangle\right|^2 \delta(\varepsilon - E_{N-1,j}) \tag{26}$$

$$B(k,\varepsilon) = \sum_j \left|\langle\phi_{N+1,j}|c_k^{\dagger}|\phi_N\rangle\right|^2 \delta(\varepsilon + E_{N+1,j}) \tag{27}$$

where $A(k,\varepsilon)$ and $B(k,\varepsilon)$ are the so-called spectral functions, i is $\sqrt{-1}$, δ is a positive infinitesimal, j is a label for the eigenvalues of the N+1 and N-1 particle systems, $|\phi_N\rangle$ is the ground state wave vector for the N particle system, and $\langle\phi_{N+1,j}|$ is the eigenvector corresponding to the eigenvalue j for the N+1 particle system. Inspecting the equations for $A(k,\varepsilon)$ and $B(k,\varepsilon)$, we see that the spectral functions are a summation of delta functions shifted by a given eigenvalue and weighted by the square of the matrix element of the raising (lowering) operator between the ground state wave vector and the respective eigenfunction for the N+1 (N-1) particle system. Given that the Greens function is an integral over ε, we see that each delta function in $A(k,\varepsilon)$ and $B(k,\varepsilon)$ will give a term of the following form.

$$\frac{\left|\langle\phi_{N-1,j}|c_k|\phi_N\rangle\right|^2}{\omega - E_{N-1,j} + \mu + i\delta} \tag{28}$$

The Greens function contains one such term for each eigenvalue of the N+1 and N-1 particle system. Each of these terms has a pole for given by the respective eigenvalue and the chemical potential. Hence the poles of the Greens function gives the eigenvalues of the N-1 and N+1 particle system.

The spectral function $A(k,\varepsilon)$ is what is measured in a photoemission experiment, while $B(k,\varepsilon)$ is measured in an inverse photoemission experiment. $A(k,\varepsilon)$ is interpreted as the probability density that a hole added to the ground states in the state k has an energy ε, while $B(k,\varepsilon)$ is probability density that an electron added to the ground state in state k has an energy ε. Summing the spectral functions over k, $\sum_k A(k,\varepsilon)$, gives the probability of finding a hole in the ground state with energy ε, and this can be thought of as an analogue of the density-of-states in a many-body system. For a non-interacting system, $A(k,\varepsilon)$ is simply a single delta function, meaning that there is a unique energy associated with each k vector. This should be intuitive given that there is a dispersion relation in a single particle system which relates k and ε.

We now wish to demonstrate that the spectral functions are given by the imaginary part of the Greens function. We begin with the following identity.

$$\mathrm{Im}\left(\frac{1}{x-a\mp i\delta}\right)=\pm\delta(x-a) \tag{29}$$

Applying this to the definition of the Greens function, we arrive at the following equation.

$$imG(k,\omega)=\int d\varepsilon\left[A(k,\varepsilon)\delta(\omega-\varepsilon+\mu)+B(k,\varepsilon)\delta(\omega+\varepsilon+\mu)\right] \tag{30}$$

$$imG(k,\omega)=\begin{matrix}A(k,\omega-\mu) & \omega>\mu\\ -B(k,\mu-\omega) & \omega<\mu\end{matrix}$$

Thus we see that the spectral function, which is an experimentally measurable quantity, is given by the imaginary part of the Greens function.

To conclude, the spectral or Lehmann representation of the Greens function allows one to transparently see the physical information contained within the Greens function. The poles of the Greens function give the eigenvalues of the N-1 and N+1 particle system, while the imaginary part of the Greens function gives the spectral function.

2.9.3 Perturbation Theory

Thus far we have discussed why the Greens function is such a useful quantity, but we have not yet discussed how one calculates it. At first site, it may appear that determining the Greens function will be prohibitively difficult given that the *exact* many-electron ground-state vector appears in the Greens function. However, Feynman-Dyson perturbation theory gives a prescription to determine the Greens function to arbitrary order. A brief outline of the key elements shall be given.

We begin by splitting the Hamiltonian into the one-body operators, H_0, and the many-body operators, H_I. The many body portion of the Hamiltonian will be treated as the perturbation.

$$\hat{H}=\hat{H}_0+\hat{H}_1 \tag{31}$$

We begin by considering the Schrödinger equation and the formal solution to the Schrödinger equation in which we have defined the time translation operator or the propagator, *U*.

$$i\frac{\partial}{\partial t}\left|\psi(t)\right\rangle = \hat{H}\left|\psi(t)\right\rangle \tag{32}$$

$$\left|\psi(t)\right\rangle = \hat{U}(t)\left|\psi(0)\right\rangle \tag{33}$$

The formal solution can be substituted back into the Schrödinger equation to generate a Schrödinger equation for the propagator.

$$i\frac{\partial}{\partial t}\hat{U}(t) = \hat{H}\hat{U}(t) \tag{34}$$

where the formal solution to this equation may be written as

$$\hat{U}(t) = e^{-i\hat{H}t}$$

We now wish to perform an iterative solution of the differential equation for the propagator. However, it is more convenient to have a Schrödinger equation in which only the perturbation appears, as opposed to the entire Hamiltonian. This can be achieved by performing a unitary transformation upon the propagator to what is known as the interaction or Dirac representation.

$$\hat{S}(t,t') = e^{i\hat{H}_0 t}\hat{U}(t-t')e^{-i\hat{H}_0 t'} \tag{35}$$

We now have a new propagator, *S*, which is sometimes referred to as the scattering matrix. Taking the time derivative of *S*, a new Schrödinger equation is found with the desired properties.

$$i\frac{\partial}{\partial t}\hat{S}(t,t_o) = H_I\hat{S}(t,t_o) \tag{36}$$

where

$$H_I(t) = e^{iH_o t}H_1 e^{-iH_o t} \tag{37}$$

Equation 36 may now be solved by iteration. The differential equation may be integrated, and the propagator itself appears in the solution.

$$\hat{S}(t,t_o) = 1 - i\int_{t_o}^{t} dt' H_I(t')\hat{S}(t',t_o) \tag{38}$$

This results may be substituted back in an infinite number of times resulting in an infinite series.

$$\hat{S}(t,t_o) = 1 - i\int_{t_o}^{t} dt' H_I(t') + \int_{t_o}^{t} dt' \int_{t_o}^{t} dt'' H_I(t')H_I(t'') + \ldots\ldots\ldots \tag{39}$$

We now have a pertubative expression for the scattering matrix, and the Greens function may be rewritten in terms of the scattering matrix.

$$G(k;t,t') = \frac{\langle\phi|\hat{S}(-\infty,t_2)c_k(t_2)c_k^{\dagger}(t_1)\hat{S}(t_1,\infty)|\phi\rangle}{\langle\phi|\hat{S}(-\infty,\infty)|\phi\rangle} \tag{40}$$

where $|\phi\rangle$ is the *unperturbed* wave vector and the creation and annihilation have been transformed to the interaction representation. Substituting the expression for the *S* matrix into the greens function, we arrive at an infinite series for the Greens function.

$$G(k;t_1,t_2) = \frac{\sum_{j=0}^{\infty}\frac{(-i)^j}{j!}\int_{-\infty}^{\infty}dt_1.....dt_j\int_{-\infty}^{\infty}\langle\phi|H_1(t_1)....H_1(t_j)c_k(t_2)c_k^{\dagger}(t_1)|\phi\rangle}{\sum_{j=0}^{\infty}\frac{(-i)^j}{j!}\int_{-\infty}^{\infty}dt_1.....dt_j\int_{-\infty}^{\infty}\langle\phi|H_1(t_1)....H_1(t_j)|\phi\rangle} \tag{41}$$

2.9.4 Feynman Diagrams

Fortunately, the above complicated equation (41) for the perturbative expansion of the Greens function often does not need to be dealt with directly given that any term in this expansion can be designated with a clever symbol known as a Feynman diagram. We shall begin by considering a simplest first-order Feynman diagram for the AIM, also known as the Hartree diagram (see Figure 1).

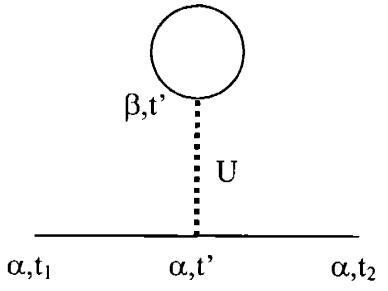

Figure 1 First order Feynman diagram for the multi-orbital AIM

Feynman diagrams are composed of interaction lines which are denoted by dotted or squiggly lines, and propagator lines which are denoted by regular lines. The interaction lines correspond to the electron-electron interaction, which in the case of the Hubbard model or the AIM is simply *U*. The propagator lines correspond to the *unperturbed* Greens function and they are labeled with an orbital index, an initial time, and a final time (or simply a frequency if Fourier transformed). A vertex is defined as the endpoints of the interaction lines, and there must be one propagator line entering and one leaving each vertex. The order of the Feynman diagram is denoted by the number of interaction lines which appear in the diagram. All of the different diagrams for a given order may be obtained by drawing the corresponding number of interaction lines and connecting them in all topologically distinct ways. Once the diagrams have been constructed, they may be translated into equations. All of the individual pieces of the diagrams are simply multiplied together, and any internal variables of the diagram (such as β and t') are summed over or integrated over. The above diagram is translated into equations as follows.

$$\int dt' G_{o,\alpha}(t_1 - t') G_{o,\alpha}(t' - t_2) U \sum_{\beta \neq \alpha} G_{o,\beta}(0) \tag{42}$$

Feynman diagrams are often intuitively thought of as scattering events. In our case, an electron begins in the α orbital at time t_1 and propagates to t'. Then the electron scatters off an electron in the β orbital and propagates to time t_2. However, it should be noted that any given Feynman diagram does not represent a physical event. Only the sum over all Feynman diagrams, which gives the interacting Greens function, represents a physical event. Nonetheless, the Feynman diagram is a useful tool which allows the rather complicated expansion of the Greens function to be written and envisioned in a very intuitive manner.

2.9.5 Finite Temperatures

Thus far we have been discussing Greens functions at zero temperature. Although finite temperature effects are not specifically addressed in this thesis, it is often more convenient to work at nonzero temperatures. This requires the introduction of the

Matsabura formalism, in which the Greens function is studied in imaginary time and/or frequency. Perhaps the easiest avenue towards understanding these concepts arises from comparing the propagator and the density operator for the grand canonical ensemble.

$$\hat{U}(t) = e^{-i\hat{H}t} \tag{43}$$

$$\rho = e^{-\beta(\hat{H}-\mu N)} \tag{44}$$

The trace over the density operator gives the partition function of the system, and therefore all thermodynamic information. Clearly, these two operators bear a striking resemblance, and the density operator can be obtained from the propagator by simply replacing $\hat{H}$ by $\hat{H} - \mu N$ and continuing time to the imaginary axis. Therefore, one can slightly modify the zero temperature procedure and obtain a perturbation expansion for the imaginary time scattering matrix.

The imaginary time Matsabura Greens function can be defined analogously to the real time Greens function.

$$G(k, \tau_2 - \tau_1) = \frac{Tr\left\{e^{-\beta(\hat{H}-\mu N)} T_\tau \left[c_k(\tau_2) c_k^{\dagger}(\tau_1)\right]\right\}}{tr\left\{e^{-\beta(\hat{H}-\mu N)}\right\}}$$

where the raising and lowering operators are now a function of imaginary time, and we follow the usual procedure of constructing finite temperature averages of operators by tracing over the density operator. Totally analogously to the zero temperature Greens function, a Lehmann or spectral representation may be constructed for the finite temperature Greens function on the imaginary frequency axis. Additionally, the Dyson equation for the Matsabura Greens function is identical to the zero temperature Dysons equation (see below). Therefore, these two functions are actually quite similar for our purposes, with one important exception. As noted above, the eigenvalues of the N+1 and N-1 particle system are given by the poles of the zero temperature Greens function. However, the finite temperature Greens function is on the imaginary axis, and therefore it must be "continued" back to the real axis in order to find the excitation energies. If the ananlytical form of the Matsabura Greens function is known, the analytic continuation is trivially replacing $i\omega$ by $\omega+i\delta$, where δ is a positive infinitesimal. However, in realistic calculations one often does not have the analytic form of the Greens function, and then

some numerical routine, such as the maximum entropy method, must be used to perform the analytic continuation. This is a major drawback of some of the finite temperature techniques, such as quantum Monte-Carlo.

2.9.6 Dysons Equation

The diagrammatic expansion of the Greens function in terms of Feynman diagrams can be formally rewritten in order to give the so-called Dyson equation.

$$G(k,i\omega_n) = \frac{1}{G_o^{-1}(k,i\omega_n) - \Sigma(k,i\omega_n)} = \frac{1}{i\omega_n - \varepsilon_k - \Sigma(k,i\omega_n)} \tag{45}$$

where Σ is the self-energy, G_o is the unperturbed Greens function, and ε_k are the eigenvalues of the unperturbed Hamiltonian. The self-energy is the sum over all irreducible Feynman diagrams. If the interactions are zero (ie. $\Sigma = 0$), it should be clear that poles of the Greens function are ε_k, and are therefore the eigenvalues of the unperturbed Hamiltonian. However, once the interactions are switched on, Σ will be nonzero and the poles of the Greens function will move away from ε_k. This suggests that the self-energy is an *effective* potential which modifies the single particle dispersion relation. Thus $H_o + \Sigma(k,i\omega_n)$ can be thought of as an effective single-particle, frequency (or time) dependent Hamiltonian which gives the eigenvalues of the interacting system. Although the Feynman-Dyson prescription indicates how to construct the self-energy to all orders, Σ cannot usually be found exactly because the Feynman diagrams above a few orders become intractable. DMFT can be viewed as a technique to obtain Σ. To summarize, when dealing with a many-body problem, one may replace the many-body term with the self-energy if a reliable approximation for the self-energy exists.

2.10 Density Functional Theory

Above it was noted that all of the ground state properties in addition to the excitations of the system may be determined from the Greens function. Therefore, the ground state energy is a *functional* of the Greens functional shown in equation 24. However, if one is only interested in the ground state energy and not the excitations, the Greens function contains excess information. This can be most easily understood by

considering density functional theory[15, 16], which indicates that the total energy may be written as a functional of the density. As noted above, the density may be written as the equal time and position limit of the Greens function (equation 23), and therefore only this limit of the Greens function is required to know the total energy in principle. Therefore we can view density functional theory as an alternative approach in which we work with the density which a simpler quantity than the Greens function.

Density functional theory essentially consists of three main pieces. First and foremost, the Hohenberg-Kohn theorem states that the total ground state energy is a functional only of the density[15]. Second, Kohn and Sham wrote the density in terms of a set of *single-particle* wavefunctions[16], which may be thought of as a non-interacting reference frame[17].

$$\rho(r) = \sum_i \psi_i^*(r)\psi_i(r) \tag{46}$$

The total energy functional may then be written as follows.

$$E[\rho] = \int \rho(r) v(r) dr + e^2 \iint \frac{\rho(r)\rho(r')}{r-r'} dr dr' + \sum_{i=1}^{N} \int \psi_i^*(r) \frac{-1}{2} \nabla^2 \psi_i(r) dr + E_{xc}[\rho] \tag{47}$$

The first term is simply the potential due to the nuclei, the second term is the Hartree potential, and the third term is the kinetic energy of the effective non-interacting particles which the density is defined in terms of. The last term is called the exchange-correlation energy and it contains everything else which has not been accounted for, such as the remainder of the kinetic energy density and the electron interactions. No exact expression is known for the exchange correlation functional. Minimizing the total energy functional with respect to the single-particle wavefunctions yields the famous Kohn-Sham equation.

$$\left[-\frac{1}{2}\nabla^2 + V_{KS} \right] \psi_i(r) = \varepsilon_i \psi_i(r) \tag{48}$$

The Kohn-Sham potential is defined as follows.

$$V_{KS} = v(r) + e^2 \int \frac{\rho(r')}{r-r'} dr' + v_{xc}(r) \tag{49}$$

The last term is the exchange-correlation potential.

$$v_{xc}(r) = \frac{\delta E_{xc}[\rho]}{\delta \rho(r)} \tag{50}$$

Given that the exchange-correlation functional is unknown, approximations must be used in order to obtain an expression for the exchange-correlation potential. One of the most commonly used approximation is the local density approximation (LDA).

The Kohn-Sham equation is an effective single particle equation which yields a set of single-particle wavefunctions that give the exact ground state density provided the exact Kohn-Sham potential is known. The eigenvalues of the Kohn-Sham are often interpreted as the eigenvalues of the N-1 and N+1 particle system, even though there is no formal justification for this[17]. However, experience has shown that this is often reasonable and the errors are consistent.

Chapter 3

The Dynamical Mean-Field Theory

3.1 Introduction

The DMFT is a powerful approximation used to solve models of strongly correlated electrons[18]. The concept of DMFT arose from probing the properties of the Hubbard model in the limit of infinite spatial dimensions[19]. The essence of infinite dimensions is that the self-energy is local, meaning that it only depends on a *single* site and is therefore independent of k. However, the self-energy still retains frequency dependence, and therefore the limit of infinite dimensions remains a nontrivial limit. Due to the fact that the self-energy is local, the infinite dimensional Hubbard model may be replaced by some effective model which also has a local self-energy. The Anderson impurity model (AIM) satisfies this criterion given that there is only one site with correlations in the model, and therefore the self-energy must be local. Thus an infinite dimensional Hubbard model is equivalent to some AIM.

The DMFT is essentially the replacement of the true self-energy of the lattice model, which is a function of k and ω, by the corresponding infinite dimensional self-energy which only depends on frequency. This local self-energy can then be identified with the self-energy of some AIM, and the parameters of the AIM can be determined self-consistently by demanding that the Greens function of the AIM be identical to the local Greens function of the lattice. In other words, DMFT self-consistently maps the local aspects of the Hubbard model onto an AIM which may be more easily solved, and the non-local aspects are simply neglected.

The above description can be cast into a set of self-consistent equations. We begin with the lattice model which is being solved, such as the Hubbard model.

$$H_{Hub} = \sum_{ij\sigma} t_{ij} d^{\dagger}_{i\sigma} d_{j\sigma} + U \sum_{i} d^{\dagger}_{i\uparrow} d_{i\uparrow} d^{\dagger}_{i\downarrow} d_{i\downarrow} \tag{51}$$

For this Hubbard model, there will be a corresponding Greens function which we can write in the frequency and k-space domain, $G_{Hub}(k, i\omega_n)$. Ultimately, this is the quantity we would like to know, as detailed in chapter 2. We begin the DMFT solution by writing the AIM.

$$H_{AIM} = \sum_{k\sigma} \varepsilon_k c^{\dagger}_{k\sigma} c_{k\sigma} + \sum_{k\sigma} V_k \left(c^{\dagger}_{k} d_{\sigma} + d^{\dagger}_{\sigma} c_k \right) + U d^{\dagger}_{i\uparrow} d_{i\uparrow} d^{\dagger}_{i\downarrow} d_{i\downarrow} \tag{52}$$

The parameters ε_k, V_k are not known a priori and they must be guessed for the first iteration. These will ultimately be determined by the self-consistency conditions which will be defined below. The on site interaction U is an input parameter which is defined in the Hubbard model. Having defined all the parameters of the AIM, the AIM may now be solved. The AIM is still a difficult many-body problem as it contains on-site interactions on the impurity site, given by the quartic term. Therefore, some approximation or numerical technique must be used to find the impurity Greens function for the AIM, $G_{AIM}(i\omega_n)$ (see section 3.3). Once we have $G_{AIM}(i\omega_n)$, the self-energy of the AIM may be determined via Dysons equation. However, we first need to construct the unperturbed Greens function for the AIM, which is also known as the bath function. The bath function emulates the lattice by allowing electrons to hop back forth between the impurity site and the bath, and it may be written in the frequency domain as follows.

$$\mathrm{G}_0^{-1}(i\omega_n) = \left(i\omega_n + \mu - \sum_k \frac{V_k^2}{i\omega_n - \varepsilon_k} \right) \tag{53}$$

Dysons equation may now be used to construct the self-energy for the AIM.

$$\Sigma_{AIM}(i\omega_n) = \mathrm{G}_0^{-1}(i\omega_n) - G_{AIM}^{-1}(i\omega_n) \tag{54}$$

Now the two self-consistency conditions shall be imposed. First, we demand that the self-energy for the AIM be identical to the self-energy for the Hubbard model.

$$\Sigma_{Hub}(i\omega_n) = \Sigma_{AIM}(i\omega_n) \tag{55}$$

Now that we have a self-energy for the Hubbard model, we may construct the Greens function for the Hubbard model using Dysons equation.

$$G_{Hub}(k,i\omega_n) = \frac{1}{i\omega_n - \varepsilon_{latt,k} + \mu - \Sigma_{Hub}(i\omega_n)} \tag{56}$$

The local Greens function of the Hubbard model may now be constructed by averaging the Greens function over *k*-space, and the second self-consistency condition is imposed by setting the impurity Greens function of the AIM equal to the local Greens function for the Hubbard model.

$$G_{AIM}(i\omega_n) = G_{Hub}^{local} = \sum_k G_{Hub}(k,i\omega_n) \tag{57}$$

Dysons equation is then used to construct a new bath function.

$$G_0^{-1}(i\omega_n) = \Sigma_{AIM}(i\omega_n) + G_{AIM}^{-1}(i\omega_n) \tag{58}$$

Therefore, one is left with a new bath function and therefore a new set of parameters for the AIM. This procedure is then iterated until convergence is reached, meaning that the self-energy, the local Greens function, and the bath function are no longer changing appreciably. Once converged, the self-energy can be plugged into equation 56 yielding the Greens function for the Hubbard model within the DMFT.

To summarize, the DMFT can be considered as mapping the lattice model onto a AIM subject to the self-consistency conditions given by equations 55 and 57.

3.2 Detailed DMFT Algorithm for the Hubbard model

In order to appreciate the above general description, we shall outline the DMFT equations for the Hubbard model for the specific case where quantum Monte-Carlo is used to solve the impurity model.

1. Guess $G_0^{-1}(i\omega_n) = \left(i\omega_n + \mu - \sum_k \frac{V_k^2}{i\omega_n - \varepsilon_k} \right)$ (59)

2. $G_0(\tau) = \sum_n e^{i\omega_n \tau} G_0(i\omega_n)$ (60)

3. $G_0(\tau) \xrightarrow{QMC} G_{AIM}(\tau)$ (61)

4. $G_{AIM}(i\omega_n) = \int_0^\beta e^{i\omega_n \tau} G_{AIM}(\tau) d\tau$ (62)

5. $\Sigma_{AIM}(i\omega_n) = G_0^{-1}(i\omega_n) - G_{AIM}^{-1}(i\omega_n)$ (63)

6. $\Sigma_{Hub}(i\omega_n) = \Sigma_{AIM}(i\omega_n)$ (64)

7. $G_{Hub}^{local} = \sum_k \frac{1}{i\omega_n - \varepsilon_{latt,k} + \mu - \Sigma_{Hub}(i\omega_n)}$ (65)

8. $G_{AIM}(i\omega_n) = G_{Hub}^{local}(i\omega_n)$ (66)

9. $G_0^{-1}(i\omega_n) = \Sigma_{AIM}(i\omega_n) + G_{AIM}^{-1}(i\omega_n)$ (67)

10. Return to step 2 and iterate until converged.

The first step is to guess the parameters of the AIM. DMFT maps the local physics of the Hubbard model onto an AIM model, but the parameters of the AIM are not known apriori and must be determined using the above self consistent procedure. In practice, one usually guesses the unperturbed Greens function, also known as the bath function, G_0^{-1} of the AIM as it is a function of the unperturbed AIM parameters. In the second step the bath function is transformed from frequency to time due to the fact that we are using QMC which works in the time domain. In the third step, QMC takes the bath function as input and solves the impurity model, giving the full Greens function of the AIM as output. In the fourth step, the greens function of the AIM is Fourier transformed to frequency because the Dyson equation is need in the fifth step to get the self-energy of the AIM. This is done in the frequency domain because Dysons equation is algebraic in frequency while it is an integral equation in time. In the sixth step, we demand that the self-energy of the Hubbard model is identically the self-energy of the AIM. In the seventh step, the local greens function for the Hubbard model is constructed, and then the Greens function for the AIM is set equal to the local Greens function of the Hubbard model in the eighth step. Finally, a new bath function is constructed using the *new* Greens function for the AIM in addition to the self-energy. Now we have a new bath function and therefore new parameters for the AIM. This procedure is then iterated until the bath function converges.

3.3 Solving the AIM

As noted above, DMFT effectively maps the Hubbard model onto an effective AIM, and therefore one is still left with a difficult many-body problem to solve. Fortunately, the AIM has been studied intensively over the past 30 years, and a number of approximations and numerical techniques exist. A few of the more prominent techniques are QMC, exact diagonalization, and iterated perturbation theory (IPT)[18]. In this thesis, both the QMC method and IPT were used. We shall derive the IPT equations below.

3.3.1 Iterated Perturbation Theory

Iterated perturbation theory corresponds to second order Feynman-Dyson perturbation theory in which the Hartree-Fock contribution to the self-energy has been shifted into the unperturbed Hamiltonian. This is equivalent to evaluating the second order diagram where the free propagators are replaced by the Hartree-Fock Greens function. Thus this procedure corresponds to perturbing around the Hartree-Fock solution with the second order diagram, and it may be considered as the simplest approximation beyond LDA+U which introduces frequency dependence to the self-energy. Specifically, we are concerned with the following diagram.

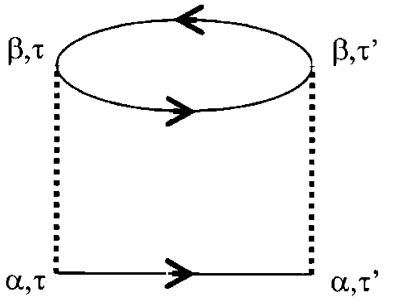

Figure 2 The second order contribution to the self-energy for the AIM. Within IPT, the lines correspond to the Hartree-Fock Greens functions.

The diagram may be translated to an equation as follows.

$$\Sigma_{\alpha}^{IPT}(\tau-\tau') = U^2 \tilde{G}_{o,\alpha}(\tau-\tau') \sum_{\beta\neq\alpha} \tilde{G}_{o,\beta}(\tau-\tau') \tilde{G}_{o,\beta}(\tau'-\tau) \tag{68}$$

where $\tilde{G}_{o,\alpha}$ is the Hartree-Fock Greens function, as opposed to the usual unperturbed Greens function.

$$\tilde{G}_{o,\alpha}(i\omega_n) = \left(G_{o,\alpha}^{-1}(i\omega_n) - \Sigma_{\alpha}^{HF}(i\omega_n)\right)^{-1} \tag{69}$$

This technique has been used extensively for the half-filled Hubbard model. When applied to the particle-hole symmetric Hubbard model, this solution has the unusual property that it is both the strong-coupling and the weak-coupling solution. Therefore, the IPT acts as an interpolation scheme for this particular case, and QMC data is reproduced with remarkable accuracy. This property does not hold when particle-hole symmetry is lost, but nonetheless it still takes an important step beyond Hartree-Fock by introducing frequency dependence to the self-energy.

3.4 LDA+DMFT

Although LDA is very successful in predicting properties of weakly correlated materials, it is known to be qualitatively incorrect if strong correlations are present[20]. In an effort to go beyond LDA, the LDA can be used to construct a Hamiltonian to which correlations can be added, and then this new Hamiltonian can be solved in any number of approximations[21-24]. Practically speaking, LDA is being used to accurately construct a Hubbard model, and it is therefore necessary to define a localized basis. This has made the LMTO method a natural choice as the electronic structure technique used to solve the Kohn-sham equations. In principle, any basis set may be used, but in the end it is necessary to define a Hamiltonian in a localized basis. This is why plane wave basis sets usually require additional work to implement beyond LDA techniques. For the time being, we will take for granted that a localized basis may be constructed independent of the basis set being used. The next decision to be made is which orbitals will be defined as the correlated orbitals (ie. perhaps the atomic-like *d* orbitals). Now the LDA Hamiltonian may be written as follows:

$$H_{LDA} = \sum_{nk\sigma} \varepsilon_{nk} C_{nk\sigma}^{\dagger} C_{nk\sigma} \tag{70}$$

where the operators C create an electron in the eigenstate of the kohn-sham equation, and ε_{nk} are the eigenvalues of the Kohn-Sham for a given band n and k-point. Now on-site correlations, referred to as the interaction term, can be added to Hamiltonian. However, the LDA Hamiltonian already contains on-site coulomb interactions which need to be removed. These shall be referred to as the double-counting terms, because they are already present in LDA and need to be removed. Unfortunately, there is no exact way to do this, and an approximation must be used. This is actually a significant limitation of the entire approach. We are left with the following Hamiltonian:

$$\hat{H}_{LDA+int} = \hat{H}_{LDA} + \sum_{R\alpha\beta\sigma} U_{\alpha\beta} d^{\dagger}_{R\alpha\uparrow} d_{R\alpha\uparrow} d^{\dagger}_{R\beta\downarrow} d_{R\beta\downarrow} - U\left(N_d - \frac{1}{2}\right)\hat{N}_d \tag{71}$$

where the indices α,β run over the correlated orbitals and the index R runs over all the sites of the lattice. The second term is the usual Hubbard interaction, while the third term is the most commonly used double-counting, where $\hat{N}_d$ is the operator for the total number of d electrons and N_d is the expectation value.

Having defined $H_{LDA+int}$, we now write the corresponding Dysons equation.

$$\left[H_{LDA} + \sum_{\alpha,\beta,R} \left|d_{\alpha,R}\right\rangle \left(\Sigma_{\alpha,\beta}(i\omega) - \Sigma_{dc}\right) \left\langle d_{\beta,R}\right|\right] \psi_{k,\omega} = \varepsilon_{k,\omega}\psi_{k,\omega} \tag{72}$$

where the first term is simply the Kohn-Sham Hamiltonian and the second term is the self energy operator for the correlated d states. The indices α and β run over the ten spin orbitals for the d states, while R runs over all the sites in the lattice. $\Sigma_{i,j}(i\omega)$ is the frequency dependent self-energy for the d electrons calculated within DMFT on the imaginary axis. Σ_{dc} is the double-counting correction to the self-energy, and it is given by $\delta_{\alpha\beta}U\left(N - \frac{1}{2}\right)$, which corresponds to the double-counting term which was defined in equation 71. $\varepsilon_{k,\omega}$ and $\psi_{k,\omega}$ are the frequency dependent eigenvalues and quasiparticle wavefunctions, respectively. This equation must be solved at every k-point for a grid of imaginary frequencies. The self-energy is not known a priori, and DMFT is used to calculate it. The same type of DMFT self-consistent equations are used as outlined above. We use the following specific procedure, where we have assumed a diagonal self-

energy for notational simplicity, and we solve the impurity model within the iterated perturbation theory.

1. Guess $\Sigma(i\omega_n)$ (73)

2. solve $\left[H_{LDA}+\sum_{\alpha,\beta,R}\left|d_{\alpha,R}\right\rangle\left(\Sigma_{\alpha,\beta}(i\omega)-\Sigma_{dc}\right)\left\langle d_{\beta,R}\right|\right]\psi_{k,\omega}=\varepsilon_{k,\omega}\psi_{k,\omega}$ (74)

3. $G_\alpha(i\omega_n)=\sum_k \frac{\psi^L_{k\alpha\omega}\psi^R_{k\alpha\omega}}{i\omega_n-\varepsilon_{k\omega}}$ (75)

4. $G^{-1}_{o,\alpha}(i\omega_n)=G^{-1}_{\alpha}(i\omega_n)+\Sigma_\alpha(i\omega_n)$ (76)

5. $n_\alpha=T\sum_n G_\alpha(i\omega_n)$ (77)

6. $\Sigma^{HF}_\alpha=U\sum_{\beta\neq\alpha} n_\beta$ (78)

7. $\tilde{G}_{o,\alpha}\left(i\omega_n\right)=\left(G^{-1}_{o,\alpha}\left(i\omega_n\right)-\Sigma^{HF}_\alpha\left(i\omega_n\right)\right)^{-1}$ (79)

8. $\Sigma^{IPT}_\alpha(i\omega_n)=\Sigma^{HF}_\alpha+U^2\int_0^\beta\left(e^{i\omega_n\tau}\tilde{G}_{o,\alpha}\left(\tau\right)\sum_{\beta\neq\alpha}\tilde{G}_{o,\beta}\left(\tau\right)\tilde{G}_{o,\beta}\left(\beta-\tau\right)\right)d\tau$ (80)

9. Iterate

This procedure is very similar to the previous algorithm given for the Hubbard model, the only major difference being that iterated perturbation theory is used to solve the impurity model instead of QMC. Only the major differences shall be outlined. The third step corresponds to the construction of the local Greens function for the Hubbard model, where $\psi^L_{k\alpha\omega},\psi^R_{k\alpha\omega}$ are the projections of the "left" and "right" eigenvectors of the Dysons equation onto the localized orbital α. It should be noted that the self-energy is not Hermitian and therefore $\psi^L_{k\alpha\omega},\psi^R_{k\alpha\omega}$ are not simply complex conjugates. In the fifth step the elements of the density matrix are constructed from the local Greens function, and T is the temperature. In the sixth and seventh step, the Hartree-Fock self-energy and Greens function are constructed. In the final step the self-energy is constructed within the IPT. This procedure is then iterated to self-consistency.

Chapter 4

Introduction to Metal-Insulator Transitions

4.1 Introduction

A portion of this thesis is concerned with a metal-insulator transition in Li_xCoO_2. In order to fully appreciate this, the different types of metal-insulator transitions shall be discussed and summarized. We begin by discussing the definition of a metal and an insulator for our purposes (ie. excluding superconductivity). A metal is a system in which the lowest energy electronic excitation is gapless, while an insulator is a system in which some finite energy must be supplied to excite an electron. Rigorously, the gap is defined as the difference of the first eigenvalue of the N+1 particle system and the first eigenvalue of the N-1 particle system. The main goal of this discussion is to understand what is causing the gap in the insulating state, and what parameters may be varied in order to induce a transition to a metallic state where the gap is zero[20, 25].

4.2 Types of Insulators

4.2.1 Band Insulator

The first and perhaps the simplest sort of insulator is the Bloch-Wilson or band insulator. This is an insulator in which the crystal potential causes the bands to split, inducing a gap. If the material has an even number of electrons which fill the bands up to the gap, the system will be a band insulator. There are many examples of this sort of insulator in nature, such as Si and pure $LiCoO_2$. A metallic state may be induced by doping the material with an element having a different valence which will induce holes into the valence band or electrons into the conduction band. Additionally, mechanical stress may sometimes by used to vary the crystal potential such that the gap closes.

4.2.2 Mott Insulator

The second sort of insulator is the Mott insulator, which results when the electron-electron interactions overwhelm the kinetic energy which would have been gained from delocalizing. This transition can be most simply understood in terms of the single band, half-filled Hubbard model. The Hubbard model contains two ingredients: the hopping parameter t which reflects the kinetic energy and the potential due to some external field, and the on-site coulomb repulsion U which is felt whenever a site is doubly occupied. When $U = 0$, one is simply left with a half-filled band which is metallic and the electron is delocalized. When the electron is delocalized, there is a relatively high probability that a site will be found to be doubly occupied. As U is increased, the system will begin to pay an increasingly larger penalty whenever a site is doubly occupied. Once $U>>t$, the electrons will localize with one per site in order to prevent double occupancy, which is the Mott insulating state. In this case, the bands will now be split with a gap of roughly U. In order to clearly illustrate this, the Hubbard model can be solved within DMFT for a series of U/t and the resulting spectral density is shown in Figure 3.

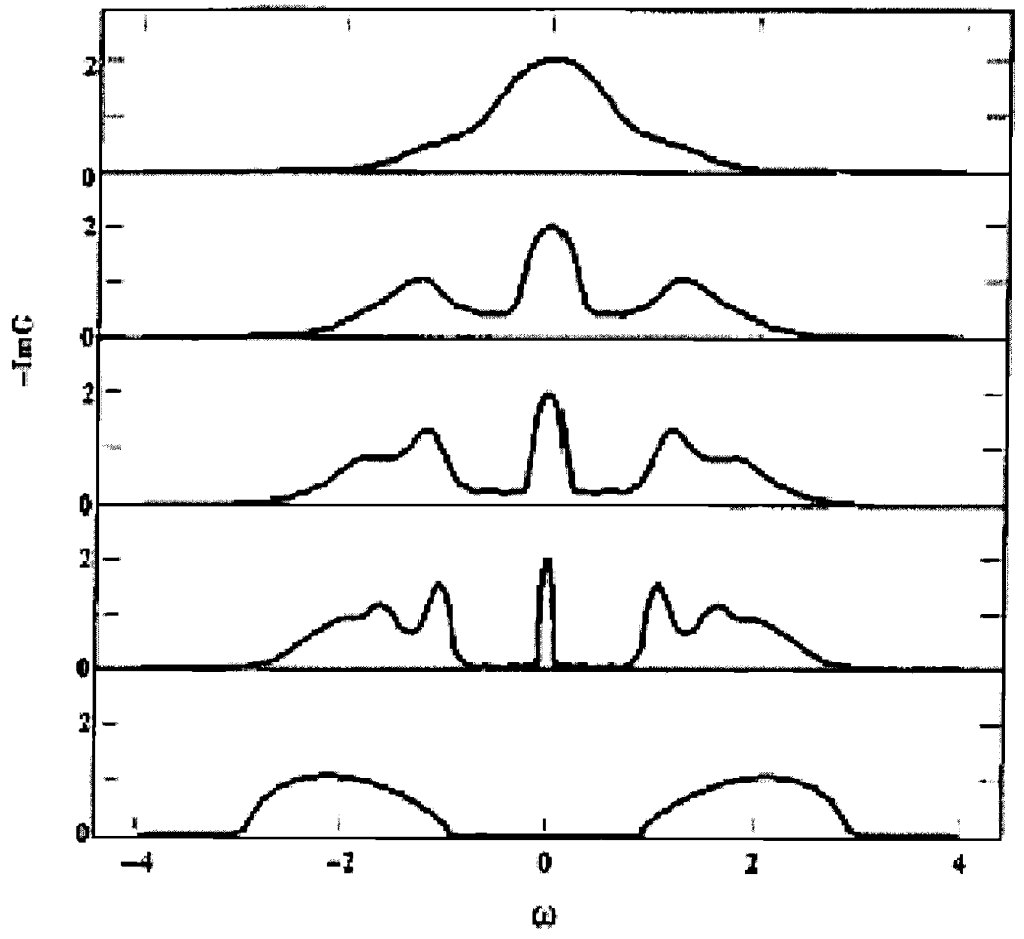

Figure 3 The spectral function for the one band Hubbard model[18]. U/t is increasing from top to bottom.

As *U/t* is increased, one can see the upper and lower Hubbard bands forming from spectral weight which has been shifted away from the region near Fermi energy. Near the transition on the metallic side, the Hubbard bands are well developed yet the system is still metallic. This reflects the dual character of the electron in this region of parameter space, displaying characteristics of both localized and delocalized states. DMFT is perhaps the only practically manageable theory which can accurately describe the insulating state, the metallic state, and the crossover between them. It should be noted that the Mott insulating state can only occur for an integer number of electrons per site. If this were not the case, the electron could always hop through the lattice while still

avoiding double occupancy. There are essentially two ways to destroy a Mott insulating state[20]. The first is referred to as a bandwidth controlled (BC) metal insulator transition, while the second is a filling controlled metal insulator transition (FC). These respectively correspond to decreasing the ratio of *U/t,* and doping the system away from integer filling. V_2O_3 exhibits a BC MIT which is induced via pressure[20]. $Ca_{1-x}Sr_xVO_3$ is not a Mott insulator for any x, but it is in the strongly correlated regime[20]. In this material, both Ca and Sr have the same valence but different sizes which distort the structure causing a variation in the strength of the hopping parameters. $La_xSr_{1-x}TiO_3$ is a Mott insulator for $x = 1$ and it displays a FC MIT as the composition is varied[20]. This also can be illustrated by solving the Hubbard model within DMFT for different dopings (see Figure 4). The correlations can be seen to increase as the system tends towards half filling, evidenced by the formation of the Hubbard gap.

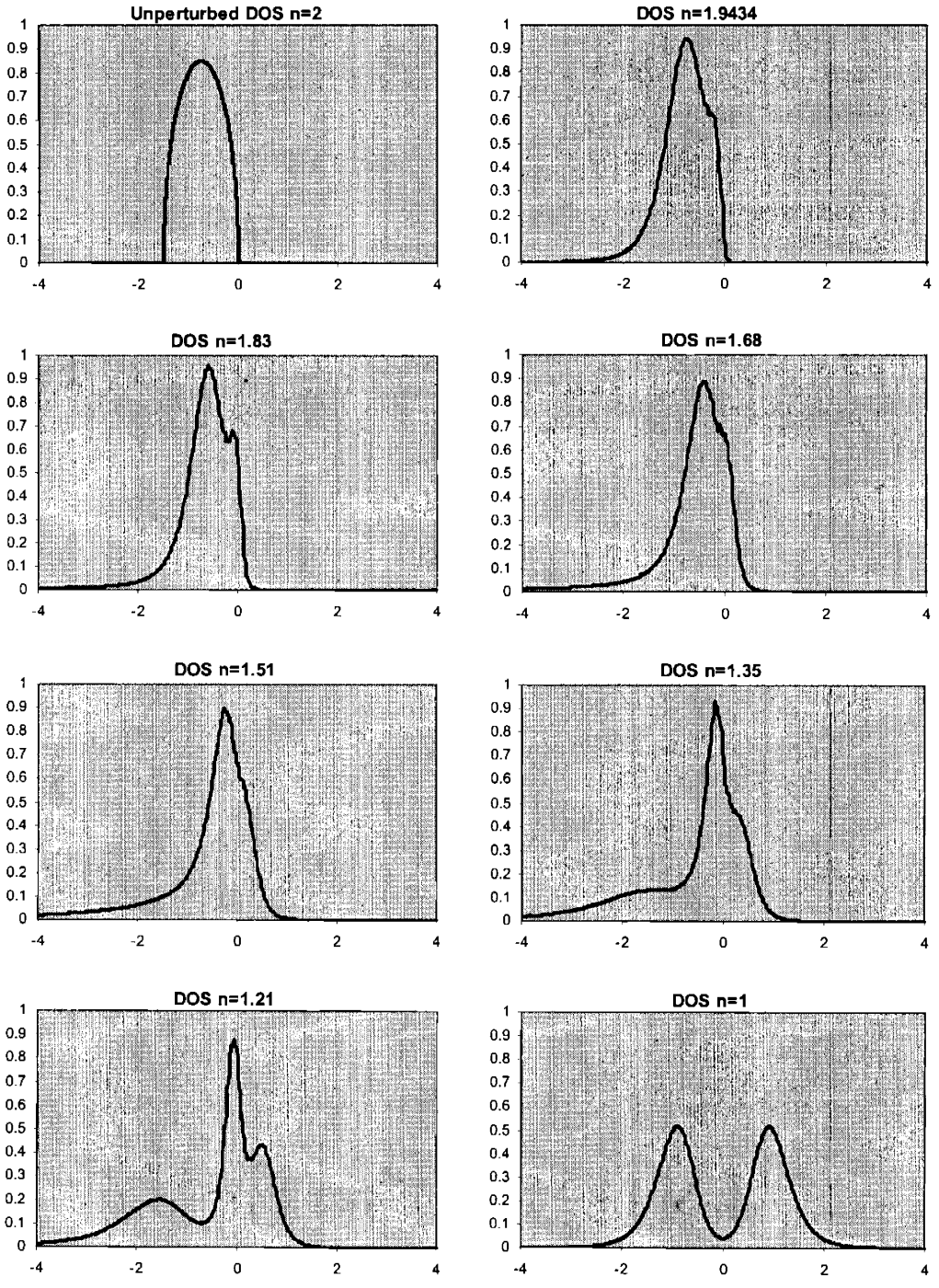

Figure 4 DMFT calculation for single band model as a function of doping for a temperature of 0.1 eV. The upper left hand panel shows the U = 0 calculation. The subsequent plots are computed using U = 3 for various total densities *n*.

4.2.3 Slater Insulator

A third sort of insulator can be created via magnetic ordering. Slater pointed out that if one is dealing with a half-filled band and antiferromagnetic spin ordering is imposed, the unit cell will be doubled which will split the bands leaving a filled band and empty band. This is known as a Slater insulator, and created an ambiguity with the Mott insulator during the early days of strongly correlated electrons. The Mott insulator may occur independently of the any magnetic ordering, but at a low enough temperature the electron spins will order in the Mott insulating state. Therefore, many of the known examples of Mott insulators are antiferromagnetic and it is not totally straightforward to differentiate the two in experiment. However, the Mott insulator may be definitively identified by heating above the Néel temperature or measuring the manner in which the specific heat diverges at the doping induced MIT. Historically, Slater's theory had the advantage of simplicity in that a single-particle theory may be used to induce the Slater insulator, while a many-body theory is required to produce the Mott insulator. The Slater insulator may be destroyed by doping away from half filling or heating above the Néel temperature.

4.2.4 Anderson Insulator

A fourth type of insulator is the Anderson insulator. Anderson demonstrated that a random potential within an electronic system, such as impurities within a metal, may cause localization and hence an insulating state[14, 25]. Qualitatively, this transition can be seen as a competition between the kinetic energy which prefers to delocalize the electron, and the potential of the random impurities which prefer to localize the electron. Anderson localization is fairly unique in that it is a *one-electron* phenomena. The impurity potential prefers to bind the electron, but the fact that localization can be achieved relies on the fact that the impurities are randomly place or have a random potential strength. Interestingly, the Anderson insulator actually has a nonzero DOS at the Fermi level despite the fact that the particles are localized. The DOS does not distinguish between states which are

spatially localized or delocalized, and the two-particle Greens function is needed to demonstrate the conductivity is zero.

4.2.5 Polarons

While on the topic of metal-insulator transitions, some attention should be given to polarons. A polarons is an electron which has been dressed by phonons. Small polaron theory can be used to show that the bandwidth will be narrowed exponentially by the electron-phonon coupling[2]. If the electron phonon coupling is large, the bandwidth can become small enough such that activated hopping will be the dominant transport mode. Thus one expects band-like behavior at zero temperature for small polarons, and possibly activated behavior at higher temperatures. It should be emphasized that the polaron itself cannot actually localize an electron, as the polaron can still tunnel through the lattice via the exponentially narrowed bands. However, polarons can greatly increase the effective mass of an electron and make it far more susceptible to an impurity potential.

4.3 Metal-Insulator Transition Near a Band Insulator

In this thesis, we are specifically concerned with a metal-insulator transition near a band insulator, and therefore it is useful to put the general discussion of MIT's from above within this context. Specifically, we shall address the role of the on-site coulomb interaction, the vacancy potential, and polarons.

4.3.1 Impact of On-site *d* Interactions

We shall begin by considering the on-site coulomb interactions of the Co *d* states and their effect as a function of doping. Given that the t_{2g} states in $LiCoO_2$ are split and a nearly isolated band exists near the Fermi energy, we study the energy as a function of doping for the one band Hubbard model. Since the Hubbard model constitutes a many-body problem, we shall need to employ an approximation. We use the Gutzwiller approximation[26] as it is not computationally demanding, yet it does an adequate job describing strongly correlated metals.

We begin by defining the single band Hubbard model:

$$H = \sum_{ij\sigma} t_{ij} C_{i\sigma}^{\dagger} C_{j\sigma} + \sum_{i} U C_{i\downarrow}^{\dagger} C_{i\downarrow} C_{i\uparrow}^{\dagger} C_{i\uparrow} \tag{81}$$

where the operator c creates an electron in some localized orbital. We assume that the unperturbed (i.e. U = 0) DOS has a Guassian form for simplicity.

$$\rho(\varepsilon) = \frac{1}{t\sqrt{2\pi}} e^{\frac{-\varepsilon^2}{2t^2}} \tag{82}$$

The number of particles and energy for the unperturbed case is defined as the usual integral over the DOS.

$$n = \int_{-\infty}^{\varepsilon_f} \rho(\varepsilon) d\varepsilon = \frac{1}{2}\left(1 + erf\left(\frac{\varepsilon_f}{\sqrt{2}}\right)\right) \tag{83}$$

$$\varepsilon_o = \int_{-\infty}^{\varepsilon_f} \varepsilon\rho(\varepsilon) d\varepsilon = \frac{t}{\sqrt{2\pi}} e^{\frac{-\varepsilon_f^2}{2t^2}} \tag{84}$$

Gutzwiller's approximation involves postulating a variational wavefunction, which is defined as follows.

$$|\psi_{GWF}\rangle = G|\psi_o\rangle = \prod_i \left(1 - (1-g) C_{i\downarrow}^{\dagger} C_{i\downarrow} C_{i\uparrow}^{\dagger} C_{i\uparrow}\right)|\psi_o\rangle \tag{85}$$

where g is a variational parameter that varies between 0 and 1, and $|\psi_o\rangle$ is the unperturbed wavefunction. The Gutzwiller operator, G, is a projection operator which projects out double occupancy. Therefore, for $g = 0$ we are left with no double occupancies, and for g = 1 we are left with the unperturbed wavefunction $|\psi_o\rangle$. Now we give the paramagnetic ground state energy as a function of the variational parameter.

$$E = \frac{\langle\psi|H|\psi\rangle}{\langle\psi|\psi\rangle} = 2q\varepsilon_o + Ud \tag{86}$$

$$q = 1 - \frac{S}{(1+g)^2}\left(1 - \frac{g^2}{1-S}\right) \tag{87}$$

$$S = \frac{1}{2\left(1-\frac{n}{2}\right)}\left(1 - \sqrt{1 - 4(1-g^2)\left(1-\frac{n}{2}\right)\frac{n}{2}}\right) \tag{88}$$

$$d = \frac{g^2}{1-g^2}\frac{nS}{2(1-S)} \tag{89}$$

where n is the number of particles. In order to derive these relations some additional approximations had to be made. Now we have an expression for the total energy as a function of the variational parameter g and the number of particles. This expression can be minimized using standard numerical techniques in order to get the energy as a function of doping and U (see Figure 5). As shown, U substantially increases the energy near half-filling. However, it is also clear that U has no appreciable effect at band fillings below roughly 0.1. Therefore, we conclude that the on-site interactions are not *directly* relevant in the dilute limit.

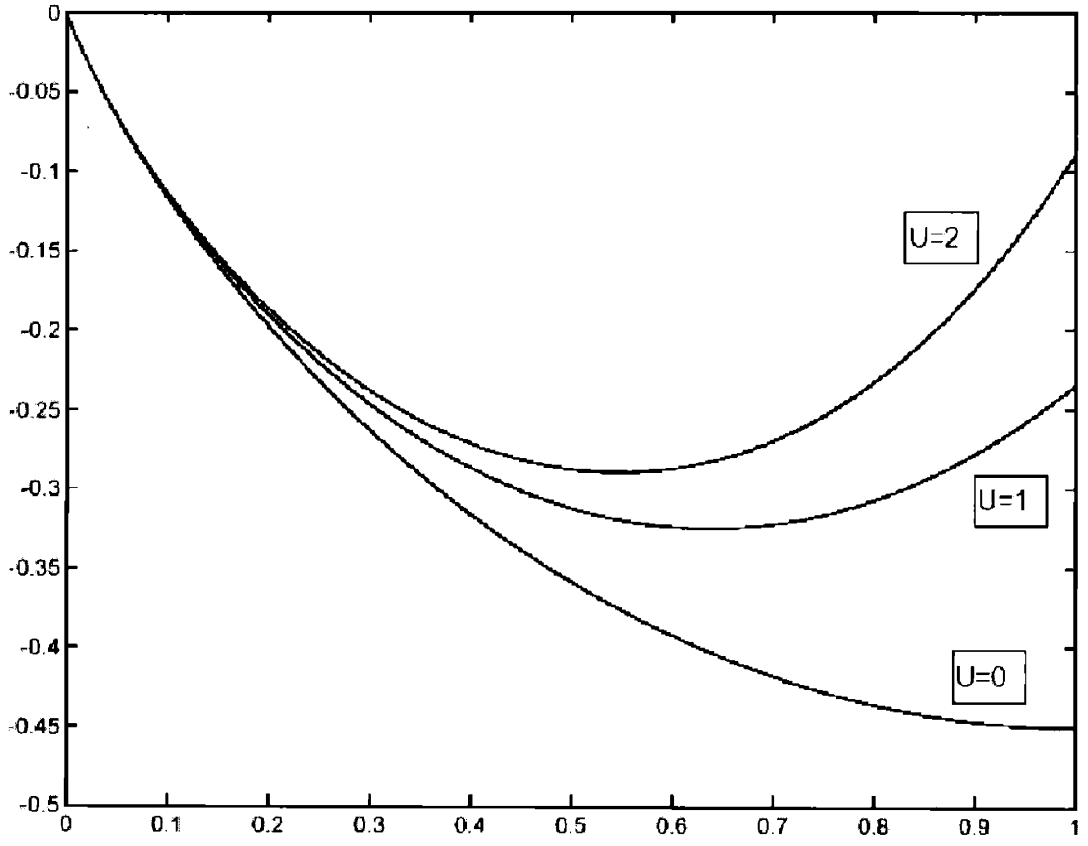

Figure 5 Energy vs. particle number for given a hopping paramter $t = 1$.

Another interesting question which can easily be addressed is the effect of a doping dependent hopping parameter. LDA calculations show that the width of the a_{1g} band in Li_xCoO_2 increases by a factor of two when all the Li is removed (see chapter 5). Additionally, the a_{1g} band begins to overlap substantially with the other bands. In order to

show the potential effect of a doping dependent hopping parameter, a calculation was performed with U = 0 and with a hopping parameter that varies linearly from 1 to 4 as x increases from 0 to 1 (see Figure 6). As shown, this in itself can cause a non-convexity and hence phase separation. It must be remembered that the hopping parameter was varied linearly in this example, and nonlinear behavior could make this effect more dramatic.

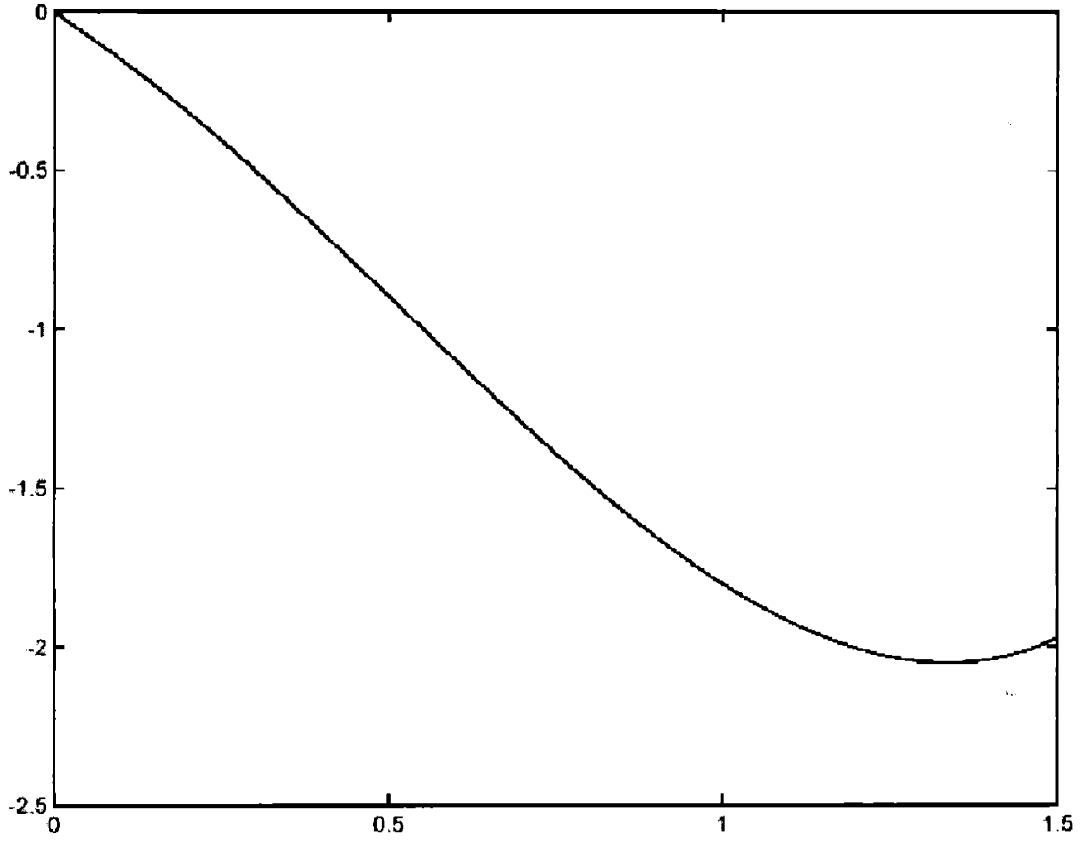

Figure 6 Energy vs. particle number for a doping dependent hopping parameter. t = 1 at x = 0 and t = 4 at x = 1. U = 0.

It is interesting to calculate the kinetic energy for the A_{1g} band in $LiCoO_2$. In order to do this, the DOS corresponding to the flat band is simply used to calculate the kinetic energy gain due to band formation (see Figure 7). It is seen that the kinetic energy per carrier is roughly 100 meV in the dilute limit, and therefore it is not difficult to understand why the holes become localized. This is also consistent with the fact that the binding energy is found to be roughly 150-300 meV in experiment.

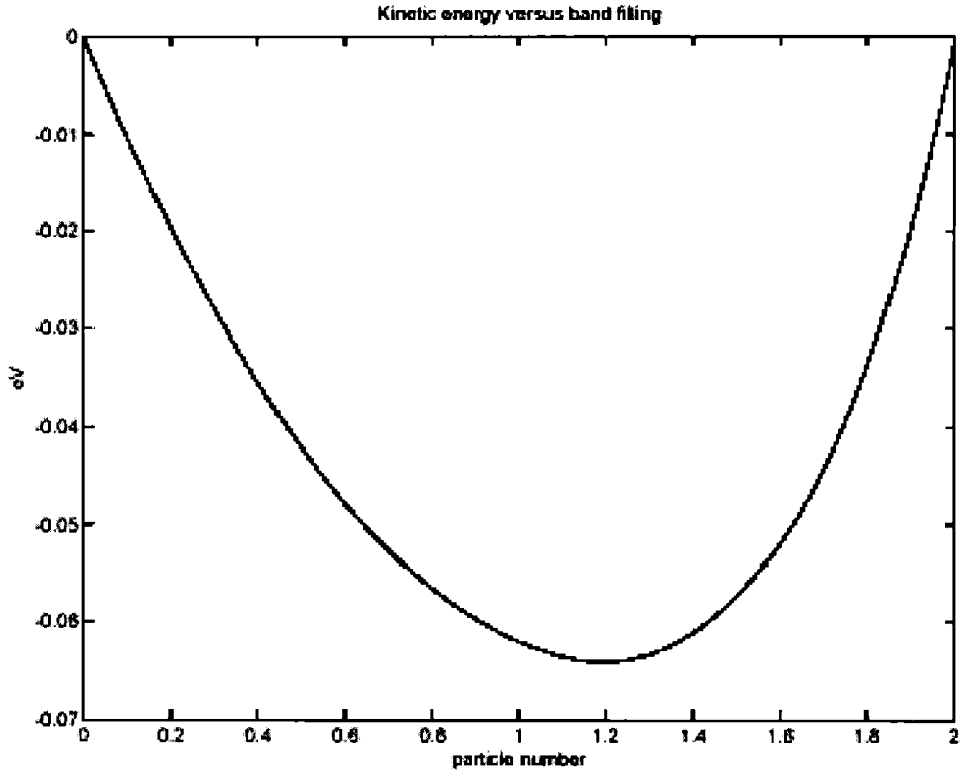

Figure 7 Kinetic energy versus filling for the LDA a_{1g} band in $LiCoO_2$. This is calculated under the assumption that the band is rigid, which is only valid for small doping.

4.3.2 The Impurity Potential

Having shown that the on-site coulomb interactions are not relevant in the dilute limit, we now turn to the impurity potential. In order to get some simple ideas of the effect of the vacancy potential, some simple arguments of Mott's shall be employed. First, we shall apply Mott's criterion for a metal-insulator transition[27].

$$n^{\frac{1}{3}}a = 0.25 \tag{90}$$

where n is the density of carriers and a is the radius of the impurity orbital. This equation was originally obtained by determining what density destroys bound states of the Yukawa potential. The constant 0.25 has been found empirically to apply well over a broad range of materials[28]. Plotting this equation for Li_xCoO_2 demonstrates that a transition at 5%

holes corresponds roughly to an impurity radius of 2 Å (see Figure 8). Given that the radius from the vacancy to the neighboring oxygen atoms is 2 A and to the nearest Co is 2.7 A, this estimate seems reasonable.

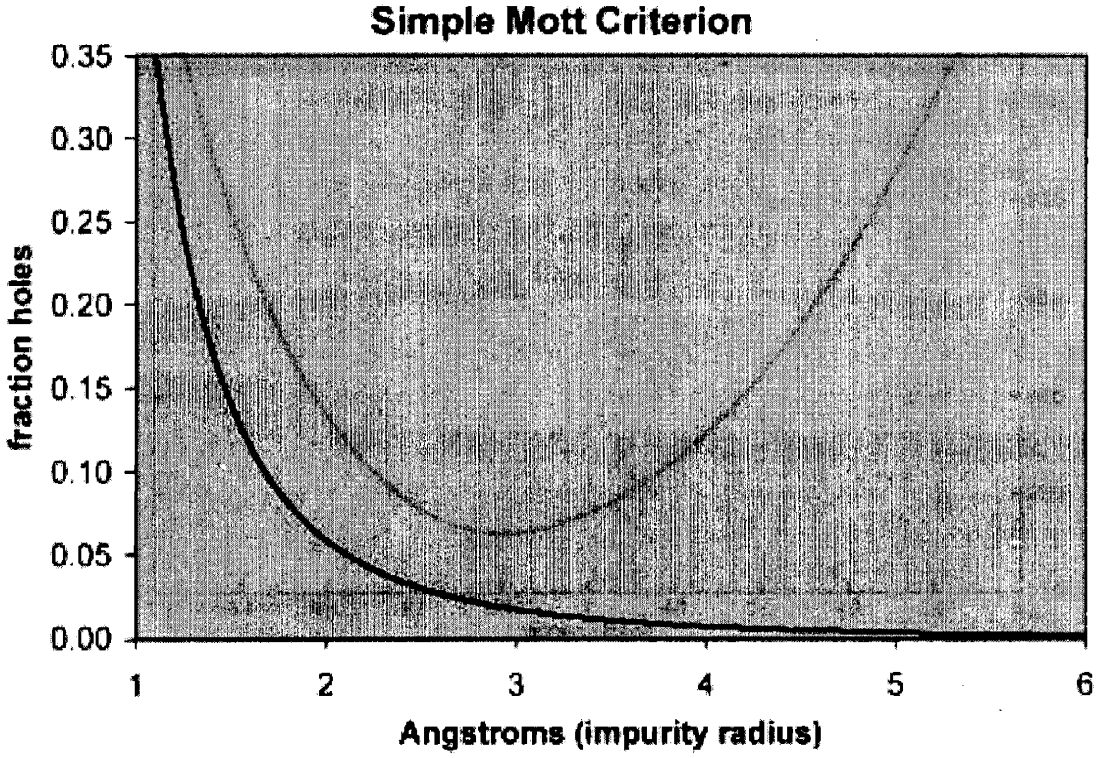

Figure 8 A plot of the simple Mott criterion for $LiCoO_2$.

Another interesting estimate is the binding energy of the hole to the vacancy. In materials with narrow bands, Mott recommended to calculate the binding energy of the polaron to the donor simply as $\frac{e^2}{\kappa d}$ where κ is the dielectric constant and d is the distance from the polaron center to the impurity site[29]. The dielectric tensor has been calculated using empirical potentials[30] and if we average the different components we get roughly 15. If we assume that the polaron sits on the Co site, this gives a binding energy of 300 meV, which is also quite reasonable.

4.3.3 Polarons

The other mechanism which can help localize the hole in the dilute limit is the polaron. In $LiCoO_2$, the symmetry is already broken, so one would not expect a Jahn-Teller effect. Therefore, the most obvious local distortion would be the simple A_{1g} mode (ie. the breathing mode). The relevant Hamiltonian for this situation is the Hubbard-Holstein model.

$$H = \sum_{ij\sigma} t_{ij} C_{i\sigma}^{\dagger} C_{j\sigma} + \sum_{i} U C_{i\downarrow}^{\dagger} C_{i\downarrow} C_{i\uparrow}^{\dagger} C_{i\uparrow} + \sum_{i\sigma} g\hat{X}_i \left(C_{i\sigma}^{\dagger} C_{j\sigma} - \left\langle C_{i\sigma}^{\dagger} C_{j\sigma} \right\rangle \right) + \sum_{i} \frac{1}{2} k\hat{X}_i^2 + \sum_{i} \frac{1}{2m} \hat{P}_i^2 \qquad (91)$$

where g is the linear electron-phonon coupling, X is the operator for the amplitude of the local A_{1g} mode, P is the momentum operator of the A_{1g} mode, k is the elastic constant, and m is the mass of the A_{1g} mode. The electron phonon coupling is a linear coupling to the density on the site minus the average density per site for the system, which will drive the electron to localize.

Instead of solving this model, some simple estimates will be considered. We know that in the dilute limit U does not have a large effect. Therefore, the kinetic energy and the polaron will be competing with each other. We know from experiment that the holes are in fact localized with a binding energy of roughly 150-300 meV per carrier. If we considered the extreme strong coupling limit (i.e. no kinetic energy), and if we assume that all the binding energy arises from the polaron, we can calculate the size of the distortion if we knew the elastic constant. We can estimate this using DFT by calculating an elastic constant for the cooperative A_{1g} mode, and this was found to be 2.4 eV/ $Å^2$. If we conservatively assume the binding energy to be -100 meV, we get an electron phonon coupling of -0.69 eV/Å. This yields a distortion which changes the bond lengths from 1.89 to 1.80 Å. Given that these were all very conservative estimates, this is a large distortion considering that the bond lengths in CoO_2 are calculated to be 1.84 Å. This simple estimate does not lend much support to the possibility of polarons, but it is a rather crude estimate.

4.4 Overview

In this section, the different types of metal-insulator transitions are presented. These different mechanisms are then discussed in the context of the metal-insulator

transition in Li_xCoO_2, which resides near a band insulator. Using Gutzwiller calculations, it is demonstrated the on-site correlations are not directly relevant in this limit. Simple estimates are used to gauge the potential importance of the impurity potential. Although qualitative, the estimates suggest the impurity potential as a reasonable mechanism of localization. These considerations lead to the calculations in chapter 6, which identify the presence of an impurity band.

Chapter 5

Introduction to Li_xCoO_2

5.1 Relevance of $LiCoO_2$

Li_xCoO_2 is currently the predominant material used as a cathode in rechargeable Li batteries. The utility of Li_xCoO_2 lies in the fact that Li may be reversibly intercalated. Therefore, it is desirable to have a fundamental understanding of all the changes which occur upon delithiation, and this has motivated a significant amount of experimental[31-34] and computational[35-39] work in the past. One of the outstanding mysteries in this material was the anomalous first-order MIT[40], and this problem has been addressed within this thesis. For $x > 0.95$, the system is insulating and for $x < 0.75$ the system is metallic, and the compositions $0.75 < x < 0.95$ consist of a two-phase mixture of the metallic and insulating phases. The fact that Li_xCoO_2 is insulating for $x > 0.95$ has negative implications for battery operations, given that reasonable electronic conductivity is necessary to operate a battery. This problem may be practically resolved by doping with a small amount of impurities to recover the conductivity[33, 41], but a fundamental understanding of the insulating state and the transition has remained a mystery.

Aside from being an important battery material, Li_xCoO_2 has a renewed sense of fundamental importance due to the close relation to Na_xCoO_2. Hydrated Na_xCoO_2 was recently found to be superconducting at very low temperatures, thus creating a strong interest in all electronic aspects of the material[42]. Qualitatively speaking, Na_xCoO_2 and Li_xCoO_2 are extremely similar materials given that Na and Li are both alkali metals, with the only notable difference being that Na^+ is a larger ion than Li^+. Therefore, a detailed understanding of the electronic structure of Li_xCoO_2 will be useful in understanding Na_xCoO_2 and its hydrated counterpart.

5.2 The Layered Structure

The layered structure is an ordered rock salt that can be envisioned as two interpenetrating face centered cubic lattices, with one lattice consisting of oxygen and the other lattice consisting of alternating *(111)* planes of Li and Co (see Figure 9 and Figure 10). In the $R\bar{3}m$ space group the Li and the Co ions remain fixed in the ideal rock salt positions, but the oxygen atoms have a degree of freedom allowing the whole *(111)* oxygen plane to relax in the *<111>* direction (Cubic cell notation). Physically, this relaxation is caused by the broken symmetry induced by the Li-Co ordering. Because the Li-Co ordering breaks the cubic symmetry and causes the oxygen atoms to relax, the point group of the metal site is reduced from O_h to D_{3d} upon ordering the rock salt lattice. Both the Co and the Li sites are coordinated by distorted oxygen octahedron, and the Co-O octahedron share edges.

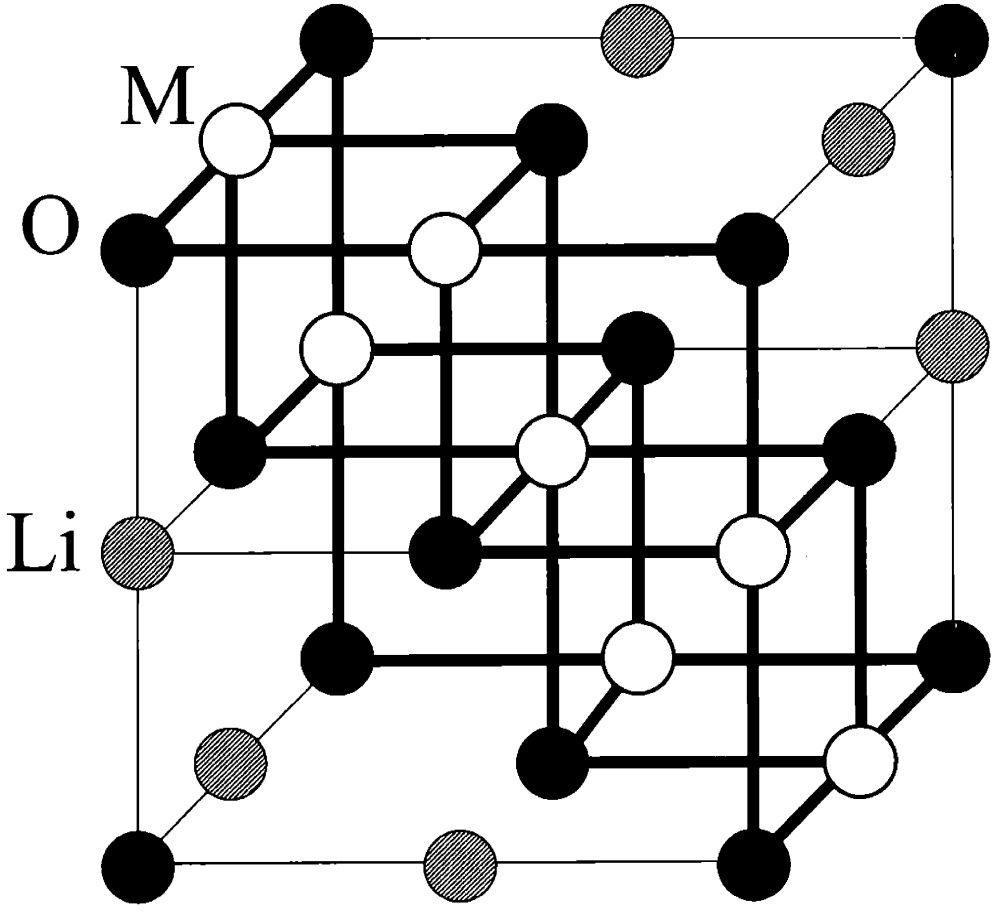

Figure 9 Layered $LiCoO_2$ ($R\bar{3}m$). Co-O bonds are designated with thick lines. In this structure, each *(111)* plane is occupied by a single species. Every other *(111)* plane consists of oxygen, while the planes in between the oxygen planes alternate between metal and Li. The Co-O octahedra share edges half with Li-O octahedra and half with other Co-O octahedra. Corners of the Co-O octahedra are only shared with Li-O octahedra. The entire oxygen plane can relax along the body diagonal. (Note that this is not a unit cell)

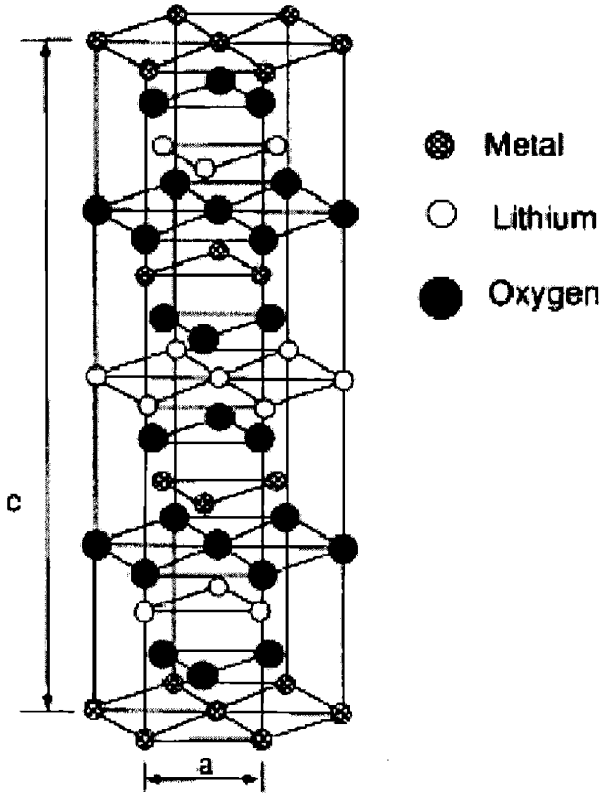

Figure 10 Layered structure in the hexagonal unit cell. The oxygen layers can relax along the *c*-axis.

5.3 Electronic Structure of $LiCoO_2$

From simple chemical considerations, one expects the two oxygen atoms in $LiCoO_2$ will accept two electrons each, the Li will donate one electron, and the Co will

donate three electrons. Therefore we expect Co^{3+}, which has a total of six electrons in the *d* shell. Due to the fact that the Co are coordinated by oxygen, the degeneracy of the five-fold *d* levels will be split by the crystal field. As noted above, the octahedron in this structure are distorted, and therefore the crystal field will have D_{3d} symmetry as opposed to O_h. However, the distortion away from O_h symmetry is relatively small and we shall therefore first consider the effects of the O_h crystal field. An O_h crystal field will split the five-fold degenerate orbitals into a set of three-fold orbitals, t_{2g}, and two-fold orbitals, e_g, with the e_g orbitals being higher in energy[43]. Although not obvious, the crystal field is stronger than the Hunds coupling, and therefore Co^{3+} is low spin with a configuration t_{2g}^6 as opposed to the high spin configuration $t_{2g}^4 e_g^2$. $LiCoO_2$ is therefore a band insulator given that the t_{2g} shell is filled and separated from the e_g states due to the crystal field splitting.

When considering the true D_{3d} crystal field, the formerly three-fold degenerate t_{2g} states of the Co atom will be split into a set of two-fold (E_g symmetry) and one-fold (A_{1g} symmetry) orbitals, while the e_g orbitals remain unchanged. The D_{3d} states which originated from the t_{2g} states will be referred to as e_g' and a_{1g} (the prime is to prevent confusion with the usual e_g states). If one considers a coordinate system aligned along the octahedral axes, the e_g' and the a_{1g} orbitals are defined as follows [44]:

$$|a_{1g}\rangle = \frac{1}{\sqrt{3}}\left(|xy\rangle + |yz\rangle + |zx\rangle\right) \tag{92}$$

$$|e_g'(1)\rangle = \frac{1}{\sqrt{2}}\left(|zx\rangle - |yz\rangle\right) \tag{93}$$

$$|e_g'(2)\rangle = \frac{1}{\sqrt{6}}\left(-2|xy\rangle + |yz\rangle + |zx\rangle\right) \tag{94}$$

The forms of these symmetrized orbitals are found using standard group theoretical techniques[43]. The a_{1g} orbital is often discussed in the literature, so we shall discuss it in a bit more detail. The A_{1g} irreducible representation is the identity representation, and therefore the a_{1g} orbital rotates into itself under all the operations of the D_{3d} point group. It is straightforward to visualize the a_{1g} orbital, as it is simply a d_{z2} orbital with its lobes pointing along the three-fold rotation axis (ie. The *c*-axis in Figure 10). In other words, if instead of choosing a coordinate system along the octahedral axis we chose a coordinate

system as in Figure 10, the a_{1g} orbital is simply d_{z2}. This immediately yields some potential insight into how the a_{1g} electrons may behave. Given that the lobes of the a_{1g} orbitals point in the *z* direction, there will be little overlap with their neighbors. This is suggestive that these orbitals may have weak dispersion. This scenario also occurs in the spinel-like structure LiV_2O_4, in which the V atoms have D_{3d} site symmetry. It has been suggested that localized a_{1g} electrons interacting with e_g' electrons give rise to the unsuspected heavy Fermion behavior in LiV_2O_4[45, 46].

As Li is removed from Li_xCoO_2, holes will be introduced into the t_{2g} states yielding a configuration t_{2g}^{6-x}. The electronic correlations among the t_{2g} states will continue to increase as the number of holes increases. CoO_2 will have one t_{2g} hole per Co, and it will likely be a Mott insulator.

5.4 Experimental Literature Review for Li_xCoO_2

In this section, we shall review the relevant experimental literature on $LiCoO_2$. Specifically, we shall be concerned with the Photoemission data, which is directly calculated using LDA+DMFT in chapter 8. Additionally, the X-ray Absorption data is reviewed given that it has implications for the rehybridization mechanism which is studied in chapter 6. Finally, the X-ray diffraction, nuclear magnetic resonance, and conductivity data pertaining to the metal-insulator transition, studied in chapter 7, is reviewed.

5.4.1 Photoemission Experiments

Van Elp et al measured the XPS valence band spectra of $LiCoO_2$[47] (see Figure 11). The data consists of a narrow main line, a broad feature from -2 to -8 eV arising from the oxygen states, a satellite from -9 to -14 eV, and the oxygen *s* states at -21 eV. The main question is what states compose the main line and the satellite. One frequently confronts this question when attempting to understand the spectrum of transition metal oxides. In order to answer this question, van Elp et al performed cluster calculations[47], and Czyzyk et al performed DFT calculations[48]. The cluster calculation involves writing

down a many body Hamiltonian for a Co ion in an oxygen octahedron. This requires the knowledge of the Racah parameters, charge transfer energy, crystal field splitting, and the Co-O hybridizations. The ground state and excited states are then written as a sum of a few Slater determinants, and the Hamiltonian is diagonalized for the N, N+1, and N-1 particle system. This yields the excitation spectra for N-1 and N+1 particle system. The predicted spectra is shown to be in reasonable agreement with experiment (see Figure 12).The occupation numbers for the ground state, the first removal, and first addition states are found to be roughly $0.47\left|d^6\right\rangle+0.44\left|d^7L^1\right\rangle+0.09\left|d^8L^2\right\rangle$, $0.17\left|d^5\right\rangle+0.5\left|d^6L^1\right\rangle+0.3\left|d^7L^2\right\rangle$, and $0.77\left|d^7\right\rangle+0.22\left|d^8L\right\rangle$, where L designates a hole in the oxygen states. The ground state is shown to be strongly mixed between d^6 and d^7L^1. The d^7L^1 state arises due to the strong hybridization between the Co e_g orbital and the oxygen p orbitals. This is complementary to what our DFT calculations have predicted for the ground state, showing 1.28 electrons in the e_g orbitals due to hybridization with the oxygen (discussed below). The cluster calculations show the first addition state to be mainly d^7 in nature.

Now the composition of the main line versus the satellite shall be reviewed. The cluster calculations show that the first electron removal state (ie. the main line) is composed mostly of d^6L^1 followed by d^7L^2. More specifically, the state d^6L^1 is predominantly $t_{2g}^5e_g^1L^1$ and the state d^7L^2 is predominantly $t_{2g}^5e_g^2L^2$ (ref [49]). Thus we see that the cluster calculation predicts that the main line arises from removing and electron from the t_{2g} states, followed by a backflow of electrons from the ligand to the e_g orbital. Roughly half of an electron is transferred from the e_g to the oxygen. The authors claim that the satellite is composed mainly of t_{2g}^5, and that its formation is largely due to the splitting of the t_{2g}^5 state and $t_{2g}^5e_g^1L^{-1}$ as a result of the large hybridization.

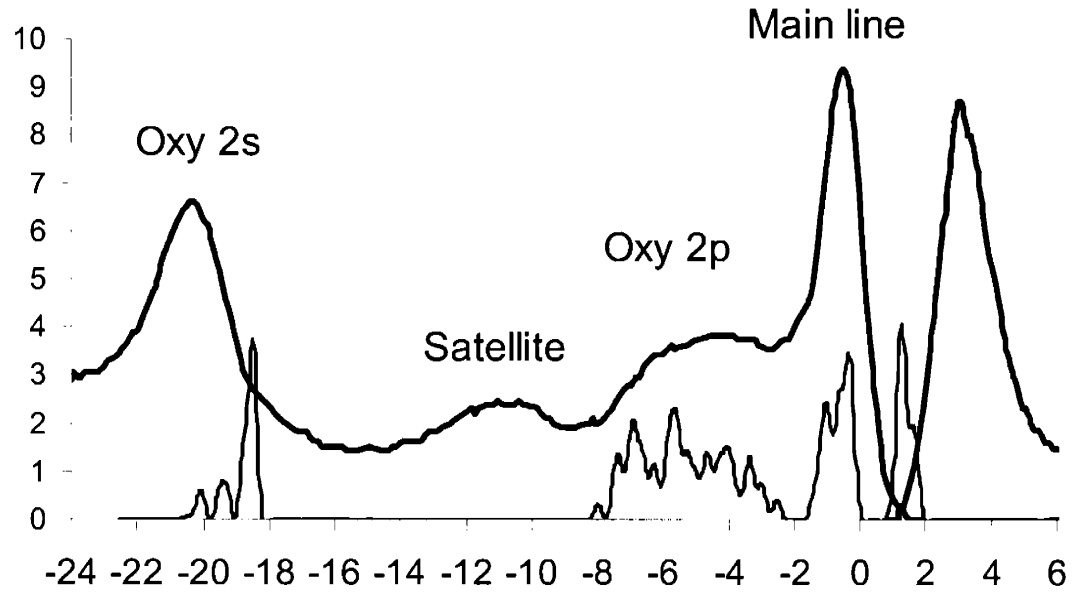

Figure 11 XPS spectrum of $LiCoO_2$ taken from van Elp[47] is given by the blue curve. LDA calculations are given by the red curve.

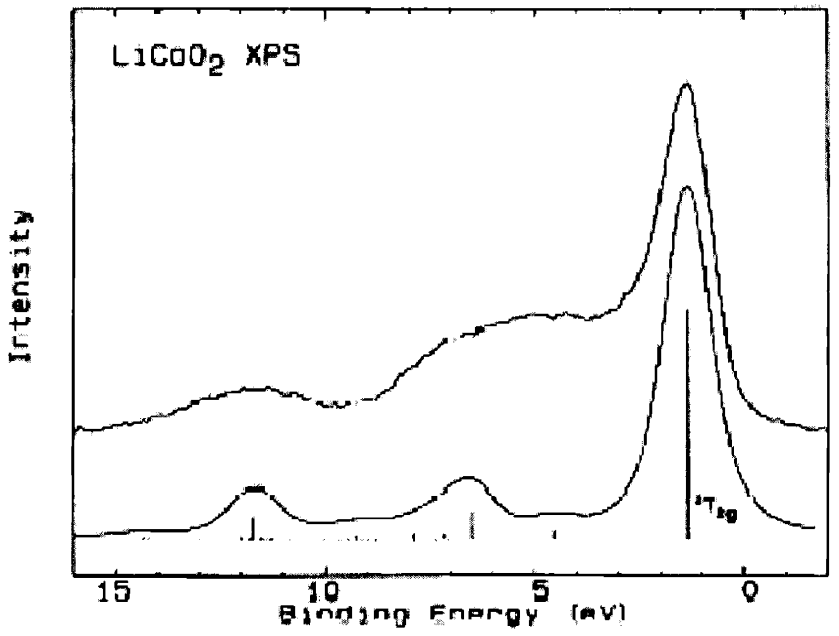

Figure 12 XPS spectrum predicted by the cluster calculations (lower curve) and the experimental result (upper curve) [47].

Czyzyk et al compared the DOS from LDA calculations to the measured XPS spectrum of $LiCoO_2$[48]. We use our LDA calculations for comparison as they are more accurate and there are no qualitative differences (see Figure 11). Before considering this data we should recall that the DOS predicted by DFT have no formal association to the removal or addition spectra[50]. However, experience has shown that this often yield reasonable results and consistent errors. The LDA spectrum successfully reproduces the main line and the oxygen *2s* states, but the oxygen *2s* states and the band gap are under predicted. Under predicting the band gap is a usual LDA error and is anticipated. However, the satellite is totally absent, suggesting that perhaps correlations are important. The satellite is predicted using LDA+DMFT in chapter 8.

5.4.2 XAS Experiments

Although the XAS spectrum is not directly predicted in this thesis, we believe that the rehybridization mechanism may be responsible for some of the interesting behavior seen experimentally, and therefore a review of the data is included. It should be emphasized that this technique has an inherently coarse energy resolution, and interpreting the data is often subtle. Two different types of XAS spectra are considered. The first is the Co 2*p* spectra, which arises from exciting an electron from the Co 2*p* levels to the unoccupied Co *d* states. There will be two main absorption peaks due to the fact that the *p* orbitals are split via spin-orbit coupling. The second type of spectra is the oxygen 1*s* spectra, which arises from exciting an electron from the oxygen 1*s* state to the unoccupied oxygen states.

A number of studies present Co 2p XAS in order to determine if Co^{4+} is formed during deintercalation or if Co^{3+} remains. Changes in the spectra as a function of lithium are extremely subtle, and opposite conclusions are sometimes reached. Dupin et al conclude that their data indicates that Co^{4+} is formed during deintercalation [51] (see Figure 13). They state that the formation of the shoulder on the high energy side of the Co $2p_{1/2}$ peak is the signature of the presence of Co^{4+}. Montoro et al have presented similar data for a range of Li compositions[52] (see Figure 14). All the curves are similar, but there are small peak shifts and possibly the formation of subtle shoulders. However, Montoro et al claim that all these curves are essentially identical and that this is evidence that Co

remains Co^{3+} through the entire deintercalation process. They suggest that the holes are totally accommodated by the Oxygen. The experiments by Yoon et al show more noticeable effects[53] (see Figure 15). It should be noted that in this study a $LiCoO_2$ thin film was used, as opposed to the previous two studies which used bulk material. These authors suggest both the Co and the oxygen may be involved in charge compensation. Galakhov et al present data on a variety of materials [54]. The most relevant comparison is between that of $LiCoO_2$ and $Na_{0.7}CoO_2$, which should be similar to the Li case. As shown, the curves are rather similar. These authors conclude that the holes in Na_xCoO_2 must be on the oxygen orbitals and Co remains Co^{3+}.

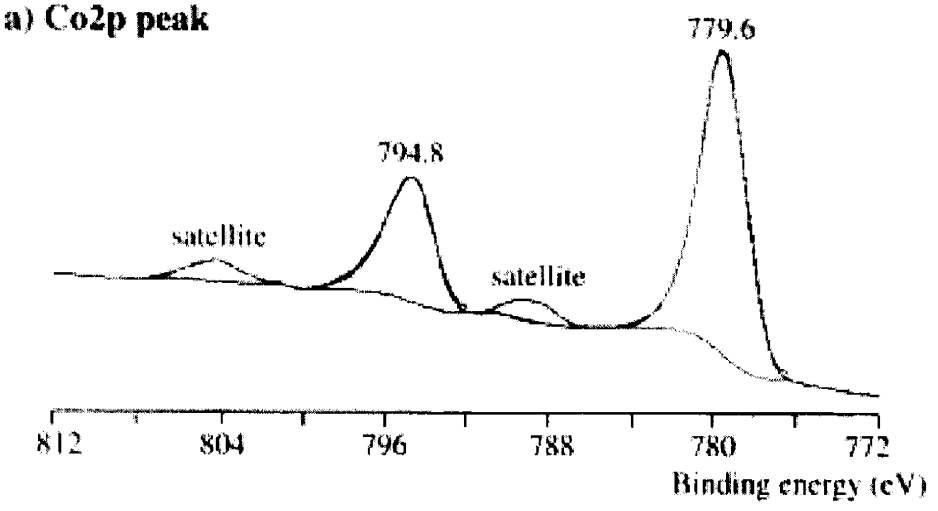

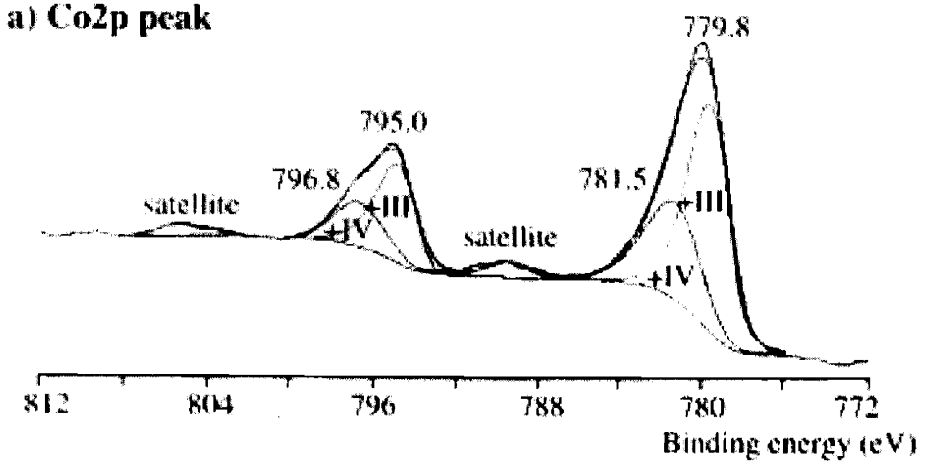

Figure 13 Co 2p XAS spectrum of $LiCoO_2$ (top) and $Li_{0.6}CoO_2$ (bottom)[51].

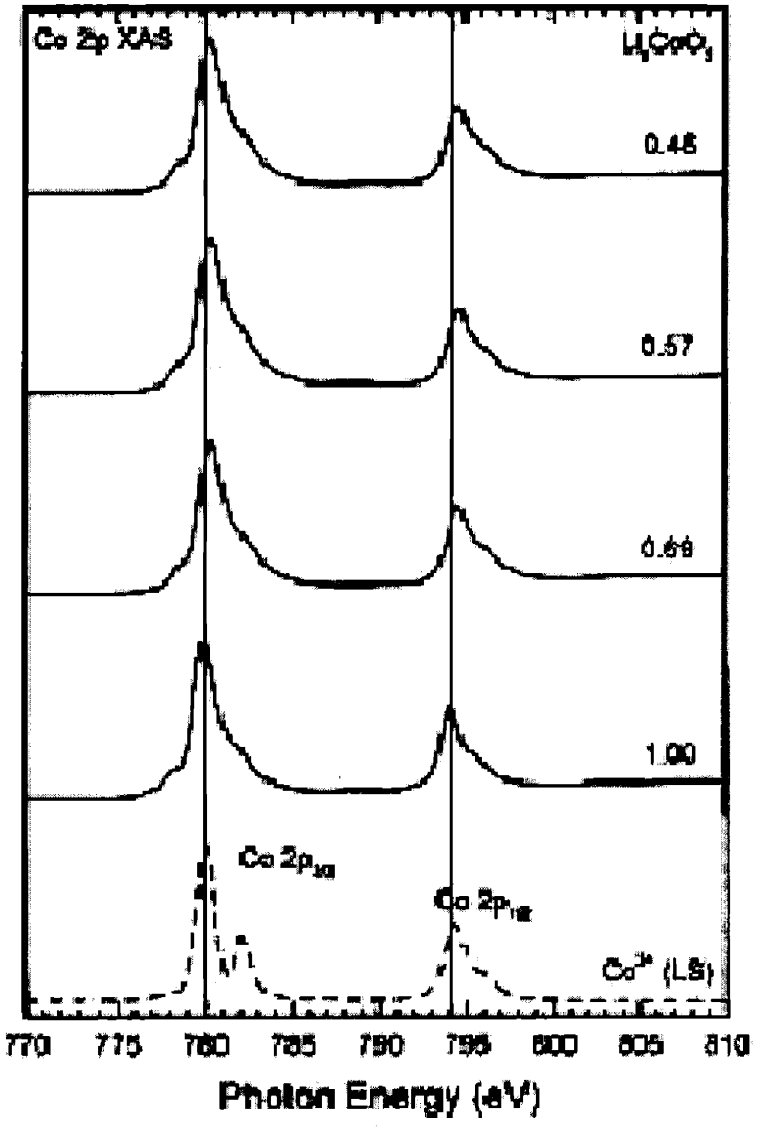

Figure 14 Co 2p XAS spectrum of Li_xCoO_2 [52]. I have added vertical lines as references to help detect changes in the peaks.

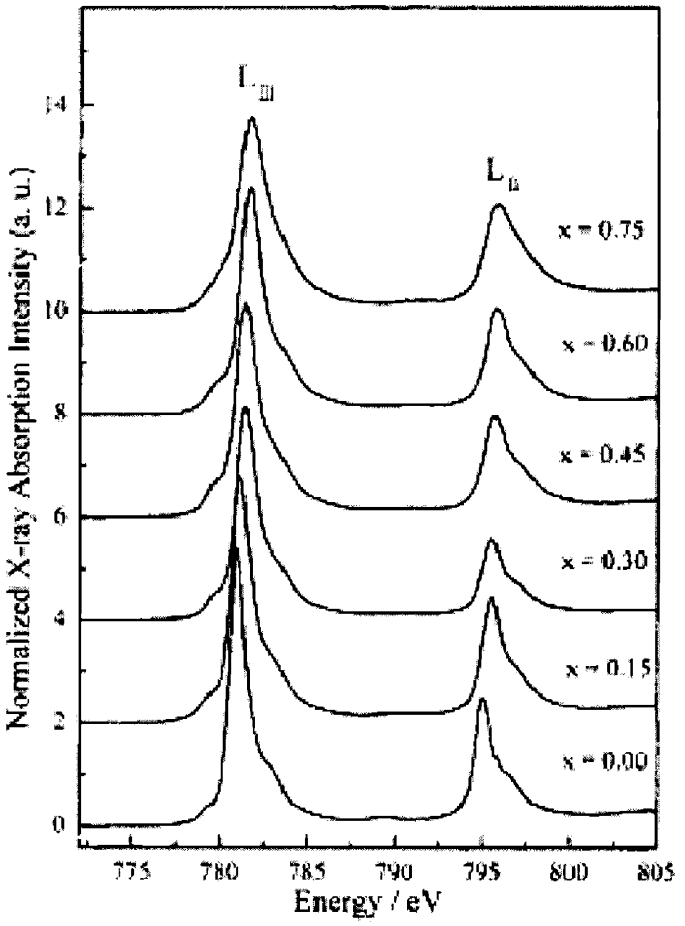

Figure 15 Co 2p XAS spectrum of $Li_{1-x}CoO_2$ [53].

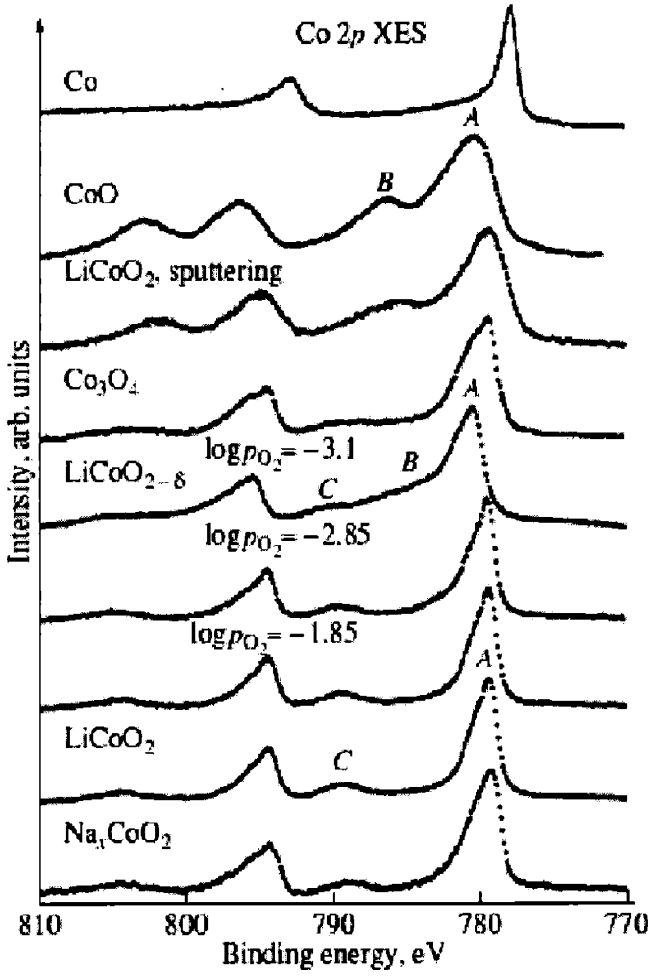

Figure 16 Co 2p XAS peak for various materials[55].

The three preceding set of authors also present O *1s* XAS spectra for same cases. Most of the data is similar, and therefore we only show the data of Montoro et al [52] (see Figure 17). The data clearly shows the growth of a shoulder on the low energy side of the first peak, suggesting that hole density is being increased on the oxygen. The predicted O *1s* XAS spectra from LDA is shown in the bottom panel, and it is in reasonable agreement with experiment. One would expect band theory to predict a similar trend as of function of delithiation given that we see the oxygen partial DOS above the Fermi level increase in CoO_2 as compared to $LiCoO_2$ (see Figure 27 and Figure 23). This is largely due to the increased mixing of the oxygen and e_g orbitals as the holes are doped into the system.

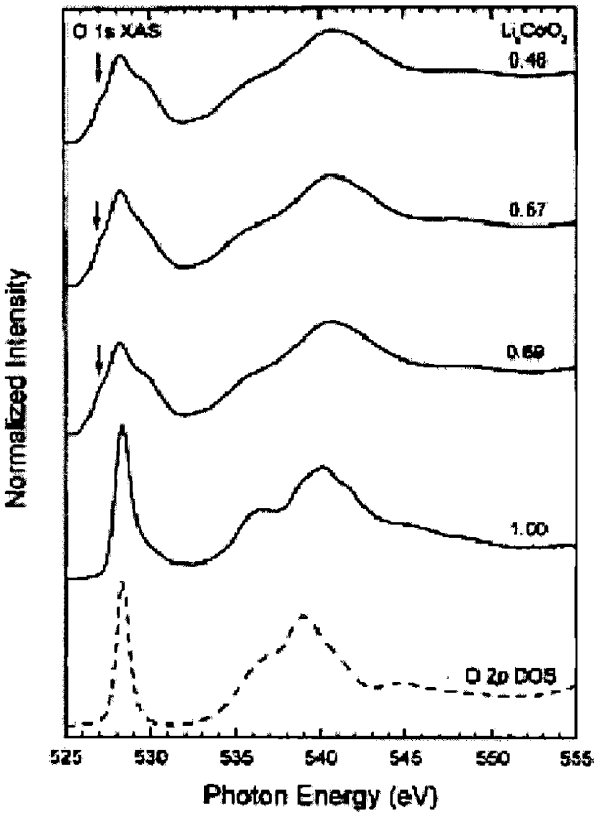

Figure 17 O 1s XAS peak for Li_xCoO_2 [52].

To summarize, XAS has shown that there is a notable change in the O *1s* data and more subtle changes in the Co *2p* data. It seems reasonable that these experiments are consistent with the results of our DFT calculations. If hole formation in the t_{2g} states is accompanied by electron addition to the e_g state, then the average change in valence is indeed smaller than going from 3+ to 4+. Additionally, our calculations support the formation of a hole on oxygen.

5.4.3 Metal-Insulator Transition

The metal-insulator phase transition in Li_xCoO_2 occurs over the two phase region for $0.75 < x < 0.95$, and this is evidenced in the voltage profile, the x-ray diffraction (XRD) data, the conductivity data, and the nuclear magnetic resonance (NMR) data[40]. The voltage profile displays a plateau, denoting a composition range of constant chemical

potential and therefore a two phase region. The XRD data indicates that the two phases have the same symmetry and the structural parameters are very similar. In the hexagonal setting, the *a* lattice parameter differ by a negligible amount while the *c* lattice parameters differ by roughly 0.7% (see Figure 18).

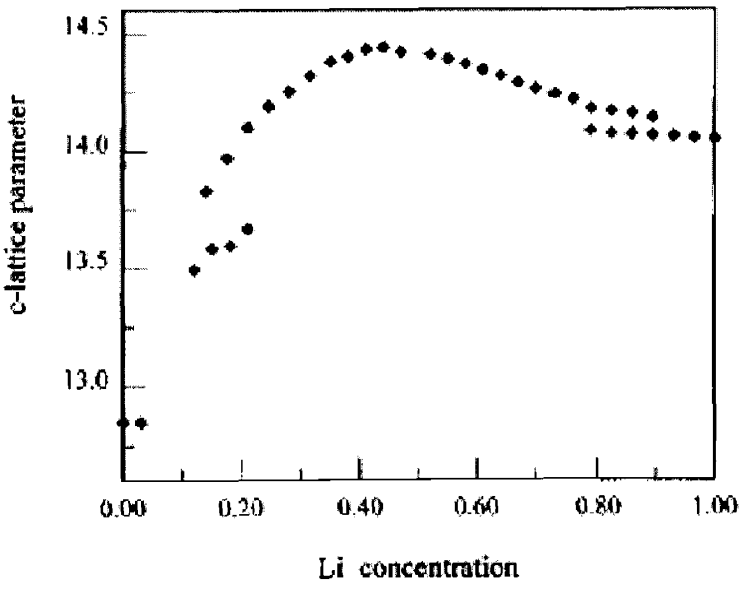

Figure 18 C parameter (hexagonal unit cell) vs *x* in Li_xCoO_2 (ref [56]). The two phase region is clearly seen in the region $0.75 > x > 0.95$.

Conductivity measurements indicate that there is a composition-dependent activation barrier for $x > 0.95$ which increases as *x* approaches one, ranging from a minimum of less than 10 meV and a maximum of 100-300 meV[40, 57] (see Figure 19). Therefore the holes are weakly bound in the insulating state. Given that pure $LiCoO_2$ is a band insulator with a gap of roughly 2.7 eV, one can infer that the samples in this study contain dilute concentrations of vacancies. For $x < 0.75$, no appreciable activation is present and the conductivity is essentially metallic.

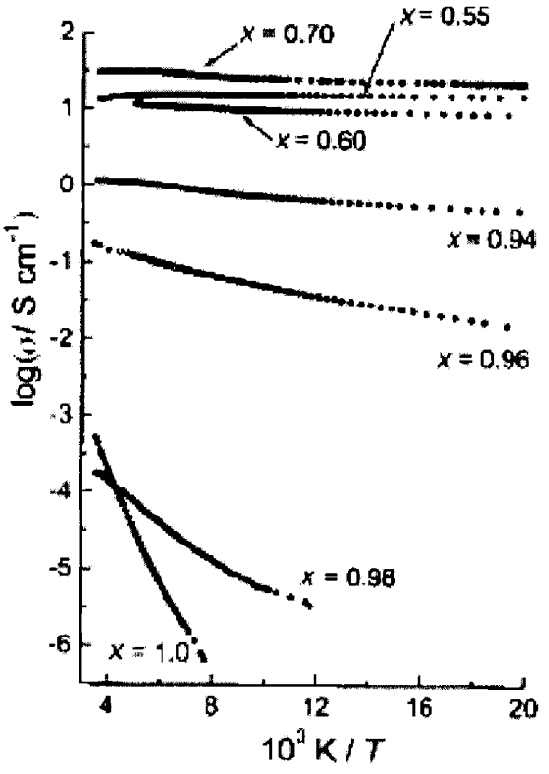

Figure 19 Conductivity data for Li_xCoO_2.

^{7}Li NMR measurements were performed over a range of compositions. The nuclear spin on the Li is extremely sensitive to the local electronic spin density, and therefore NMR is an excellent local probe of the electronic structure. Given that $LiCoO_2$ is diamagnetic, one would expect a single peak centered about $\delta = 0$ since there is no electronic spin density to interact with the nuclear spin, and this is indeed observed (see Figure 20). As holes are doped into the system within the insulating phase, the intensity of the peak decreases while no shifting of the peak occurs. Although this behavior is not totally transparent, there are several plausible reasons as to why it may occur[58]. As Li is removed from the sample, one would expect some decrease of intensity of the peak at $\delta = 0$ simply because there are fewer Li present. However, one would also expect to see some shift of the signal due to the presence of the hole density which is created as Li is removed, and this is not observed. One possible explanation is that the Fermi contact shift and/or the dipolar interaction due to the hole density is so strong that a portion of the

signal is shifted to a completely different frequency range which is not being considered in the experiment. Given that we know from experiment that the holes are bound, it may be reasonable to expect a strong interaction. The figure indicates that the original peak has shrunk to 25% of its original value at the onset of the transition.

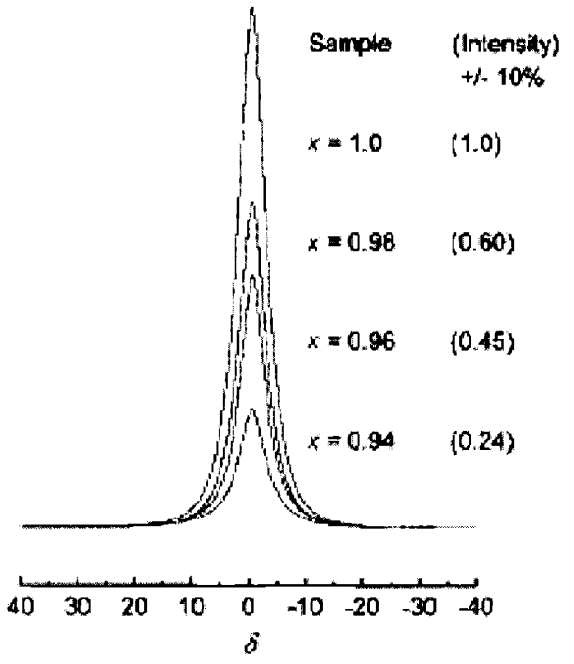

Figure 20 ^{7}Li NMR spectra for Li_xCoO_2 for $x > 0.94$.

Once $x < 0.95$, and additional Knight-shifted NMR peak corresponding to the $x = 0.75$ phase appears and grows at the expense of the $x = 0.95$ peak (see Figure 21). The Knight-shifted peak of the $x = 0.75$ phase is indicative of metallic electrons. Therefore the NMR data clearly supports the notion of a metal-insulator transition. A similar study was performed by Imanishi et al which yielded comparable results[59].

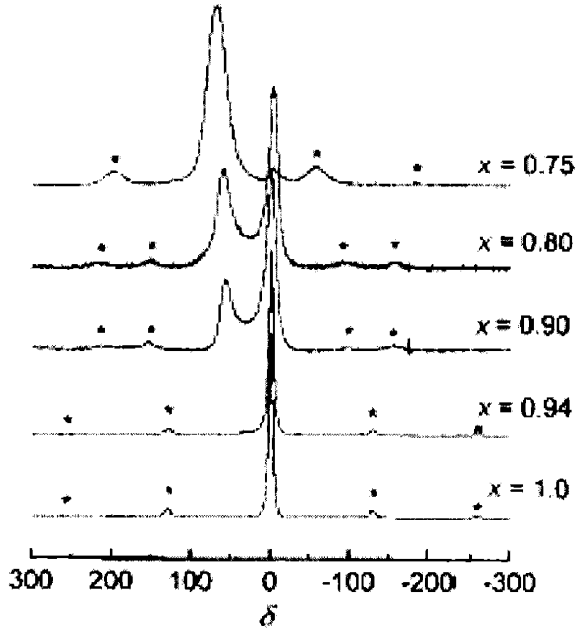

Figure 21 ^{7}Li NMR spectra for Li_xCoO_2. The change from a paramagnetic contact shift to a night shift is clearly observed.

5.5 LDA Calculations of the electronic structure of $LiCoO_2$ and CoO_2

In this section, we present various LDA band structures and DOS calculations. Many of these results have been published in some form, but there are a number of interesting details which have not been yet received attention in the literature, such as the relatively flat band near the Fermi surface in $LiCoO_2$. The band structure and DOS for $LiCoO_2$ are shown in Figure 22 and Figure 23, respectively. The two bands above the Fermi level are the e_g states, which are clearly separated from the fully occupied t_{2g} states below the Fermi level. At the gamma point, one can clearly see that the t_{2g} bands have been significantly split by roughly 1.5 eV, with the a_{1g} band above the e_g' bands. The a_{1g} band is quite flat, with a total width of roughly 0.35 eV, while the e_g' bands show a larger width of 0.9 eV. The oxygen bands are clearly separated from the t_{2g} bands. The decomposed DOS in Figure 23 illustrate that there is mixing between the oxygen *p* states and the Co *d* states. The oxygen states are mixed more heavily with the e_g states than the t_{2g} states, as one would expect considering the overlap. Also, this is evidenced by the e_g

peak in the oxygen states and the oxygen peak in the e_g states. The bandstructure calculations thus suggest that the ground state of this material contains filled t_{2g} states with hybridization induced filling of the e_g states and hole formation in the oxygen states, in qualitative agreement with the cluster calculations. This statement can be made more quantitative by calculating the orbital occupation numbers (see Table 1). The oxygen hole has been defined as the integral of the oxygen partial DOS within the e_g peak, which is essentially the unoccupied portion of the oxygen states due to hybridization with the e_g states. The e_g states have 1.28 electrons, while each oxygen atom has 0.52 holes (2 per cell).

	O	t_{2g}	e_g	O hole
CoO_2	6.46	4.50	1.63	0.72
$LiCoO_2$	6.71	4.90	1.28	0.52
CoO_2+1	6.72	4.92	1.38	0.60

Table 1 Orbital occupation numbers. The oxygen hole is the integral of the oxygen partial DOS within the e_g peak (ie. above the Fermi level).

Although it is clear that there is a significant splitting of the t_{2g} states, it is clear that the a_{1g} band and e_g' band do cross in the *X* direction in *k*-space. This raises the question of how often crossing occurs. In order to get a feel for this, it is instructive to inspect the total DOS. The t_{2g} DOS form a three peaked structure, and the top peak correspond to the a_{1g} band. It is fairly clear that the DOS is nearly zero between the top peak and the middle peak, and this is very suggestive that crossing is a rare event. It is also interesting how the e_g' bands form a two peak structure. This appears to occur because one of the bands disperses more before leveling off. The three peak structure of the DOS does appear to be a fairly generic quality in that it can also be seen in $LiNiO_2$. However, this structure is destroyed once this system is sufficiently doped, as we shall see in CoO_2.

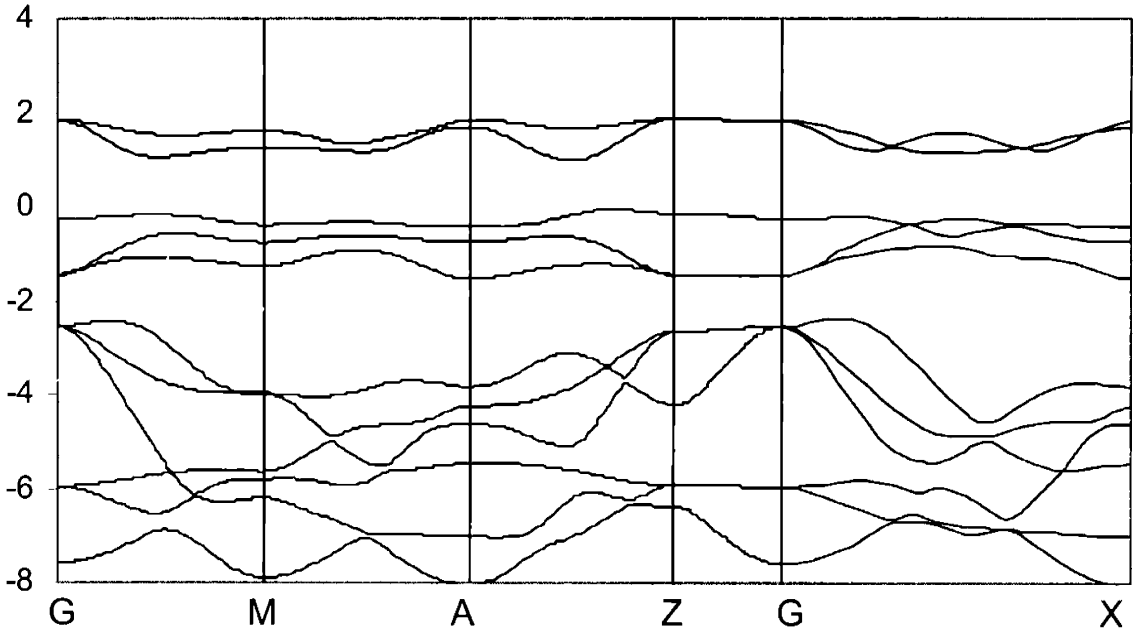

Figure 22 Non spin polarized band structure for $LiCoO_2$ calculated within LDA. The Fermi energy is zeroed. The e_g bands are in blue, t_{2g} in red, and oxygen in green.

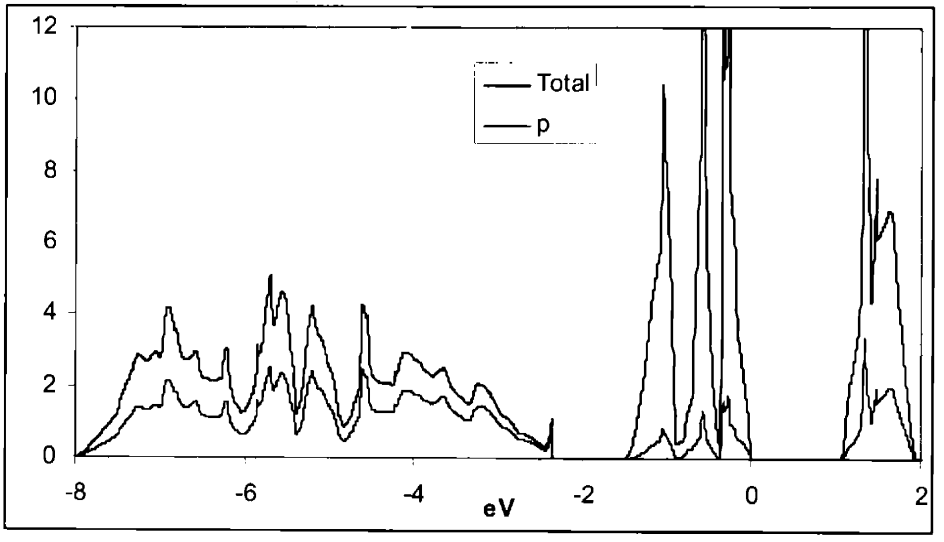

Figure 23 DOS for $LiCoO_2$ calculated with LDA. The decomposition into oxygen *p* states is also shown. The Fermi level is zeroed. All atomic sphere radii used in the DOS projection are 1 Å.

Thus far we have been labeling each band by its symmetry at the gamma point, but it is useful to project the DOS onto the symmetrized orbitals to see the composition of each band (see Figure 24). It should be noted that the difference between the a_{1g} projection and the e_g' projection is an indication of how broken the symmetry is (ie. they would be identical if the t_{2g} symmetry was not broken), and therefore the symmetry is clearly broken. At the same time, it should also be noted that the flat band clearly has a mixed character between A_{1g} and e_g'. Therefore we should not lose sight of the fact that the "a_{1g} band" is clearly of mixed character. However, the a_{1g} state is clearly dominant at the Fermi level, which is what is pertinent for small doping. Additionally, there is still a strong presence of the a_{1g} character at the bottom of the t_{2g} DOS.

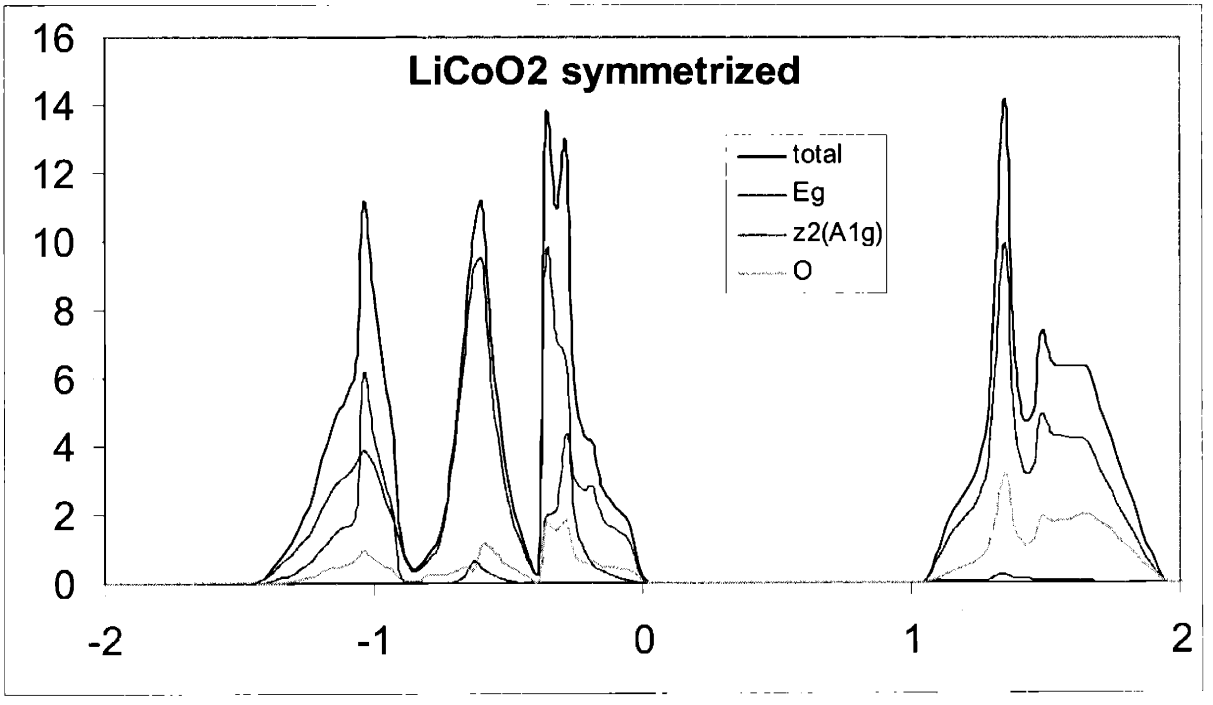

Figure 24 DOS for $LiCoO_2$ calculated with LDA. The decomposition into a_{1g} and e_g' states is also shown. The Fermi level is zeroed. All atomic sphere radii used in the DOS projection are 1 Å.

The total DOS for $Li_{0.5}CoO_2$ is shown in Figure 25. It is clear that the a_{1g} band and the e_g' bands begin to overlap more once the system is doped with 50% holes, given that the two peaks nearest the Fermi energy are significantly overlapping.

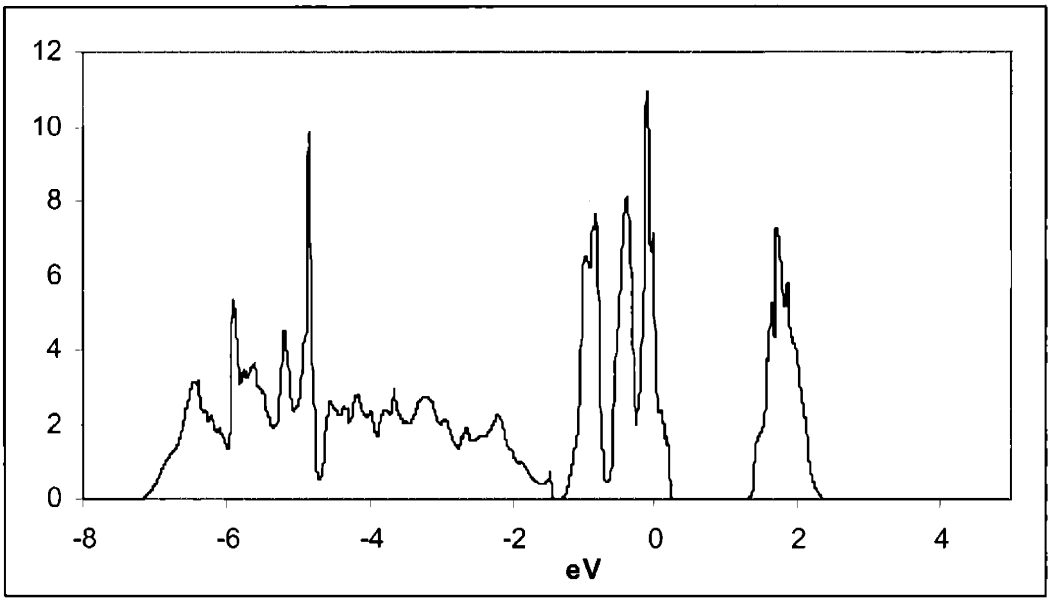

Figure 25 DOS for $Li_{0.5}CoO_2$ calculated with LDA.

The band structure and DOS of CoO_2 show some noteworthy differences (see Figure 26 and Figure 27). Several of the oxygen bands have crossed into the t_{2g} bands, demonstrating that the bands are behaving in a non-rigid fashion. The formerly flat band near the Fermi surface has become much wider, with a width of about 1 eV. The Fermi level now cuts through this band, indicating the formation of holes in this band. The decomposed DOS clearly illustrate that the mixing between the oxygen *p* states and the Co *d* states has increased. Projections onto the a_{1g} orbital still shows a presence at the Fermi level, although the mixing has increased and there is substantial band crossing among the a_{1g} band and the e_g' band (see Figure 28). These calculations predict that the ground state will have a hole in the t_{2g} states, and increased hybridization has caused a higher population of the e_g states and a larger hole in the oxygen states (see Table 1).

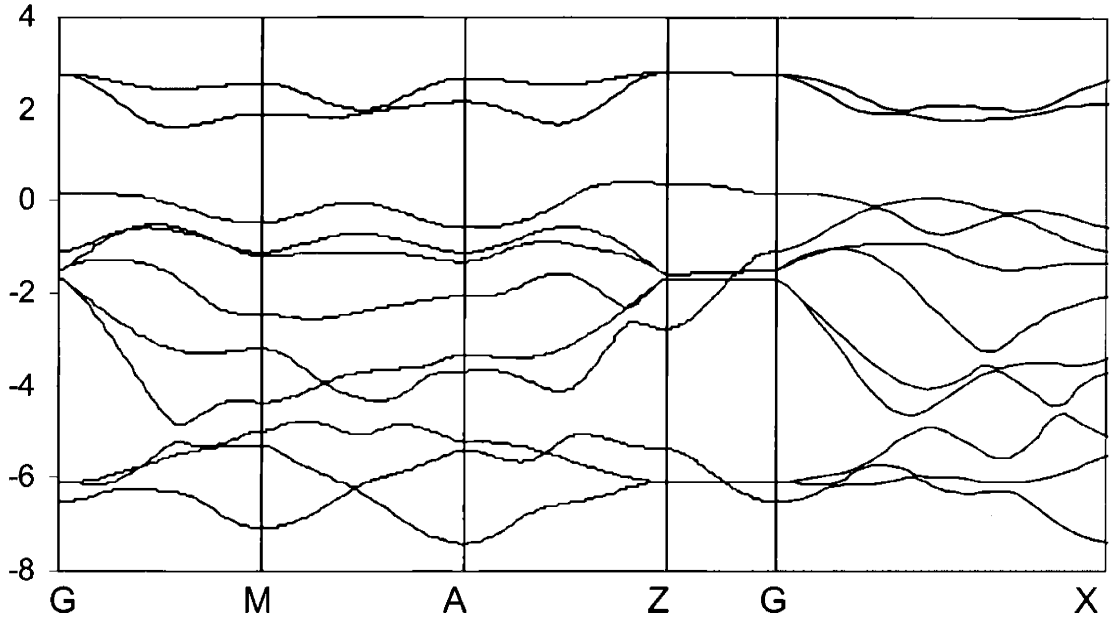

Figure 26 Non spin polarized band structure for CoO_2 calculated within LDA. The Fermi energy is zeroed. The e_g bands are in blue, t_{2g} in red, and oxygen in green.

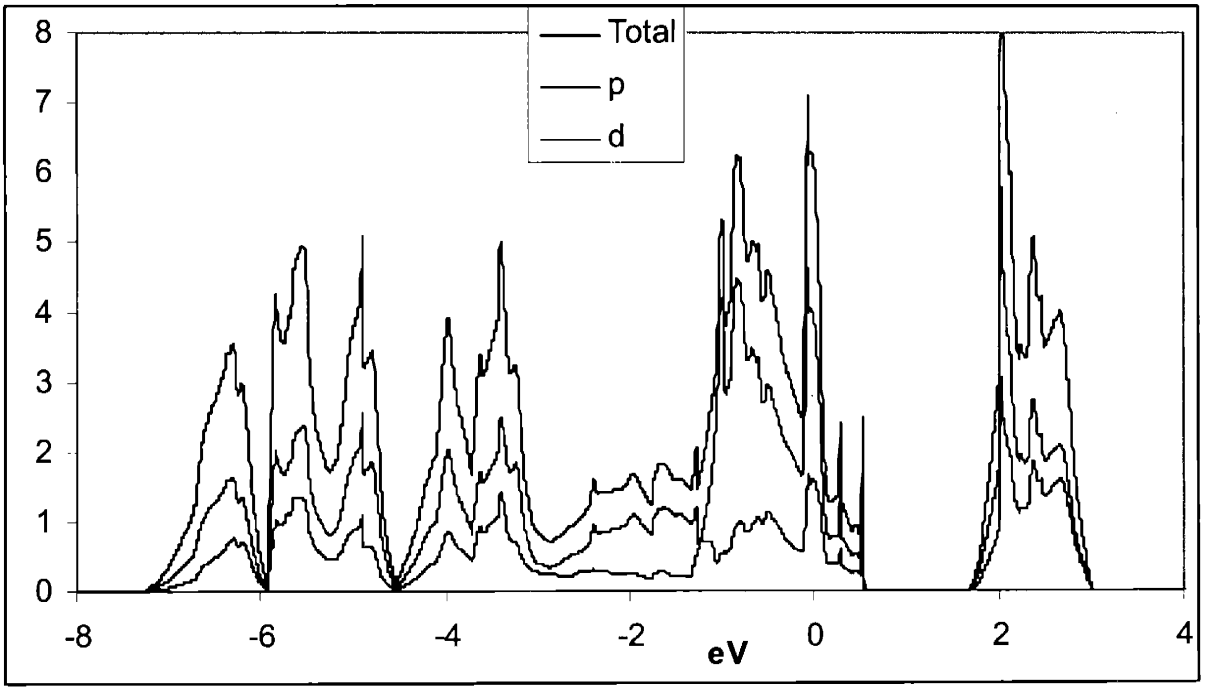

Figure 27 DOS for CoO_2 calculated with LDA. The decomposition into oxygen *p* states and Co *d* states is also shown. The Fermi level is zeroed. All atomic sphere radii used in the DOS projection are 1 Å.

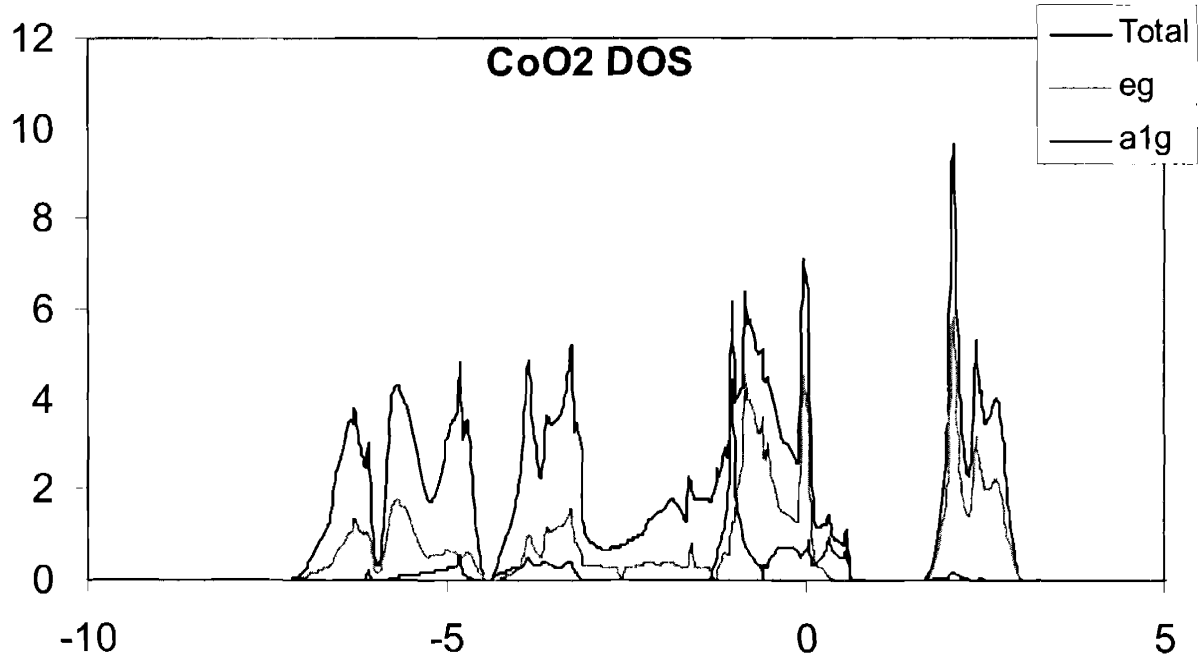

Figure 28 DOS for CoO_2 calculated with LDA. The decomposition into a_{1g} and e_g' states is also shown. The Fermi level is zeroed. All atomic sphere radii used in the DOS projection are 1 Å.

Rehybridization Mechanism

The rehybridization mechanism in Na_xCoO_2 is the subject of chapter 6. In this section, we provide the same charge density difference plots for Li_xCoO_2 in addition to a plot of the total charge within spheres centered on the atoms versus sphere radius (Figure 29, Figure 30, and Figure 31). These figures clearly illustrate that the same type of rehybridization occurs in $LiCoO_2$ (see chapter 6 for details).

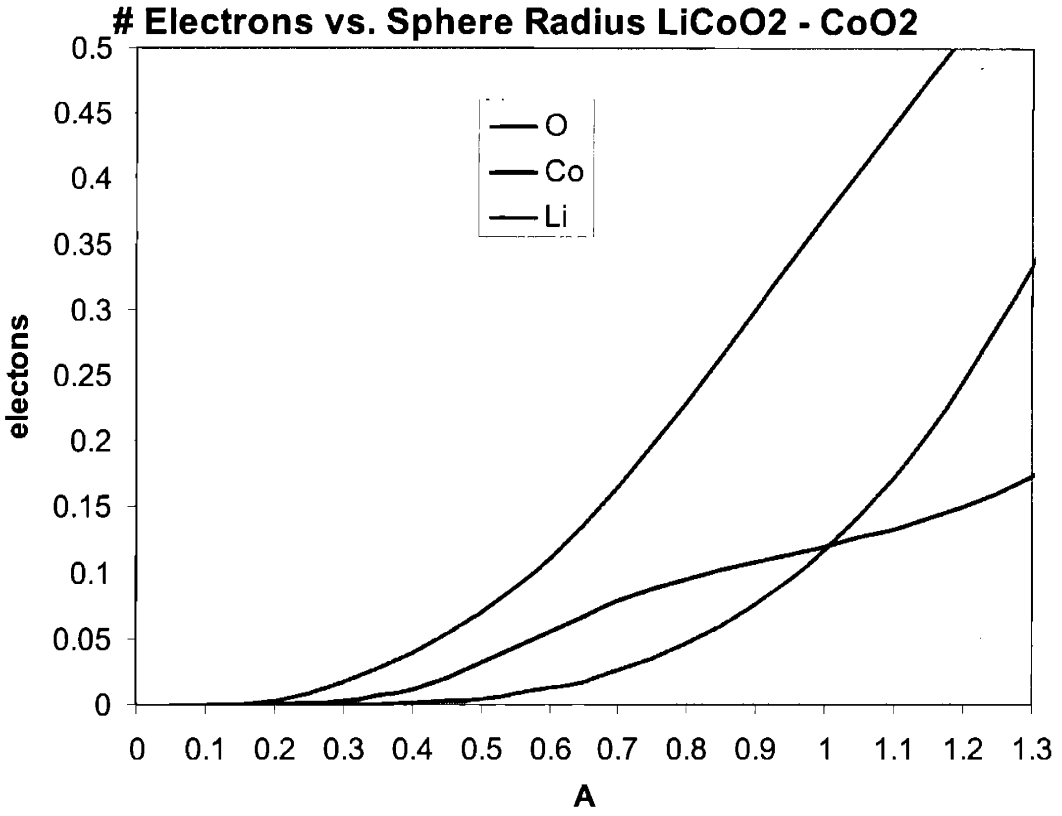

Figure 29 A plot of the change of the number of electrons within a sphere versus the radius of the sphere (ie. adding Li to CoO_2) . The oxygen curve represents both oxygen sites within the unit cell. Clearly, the oxygen accepts a majority of the charge.

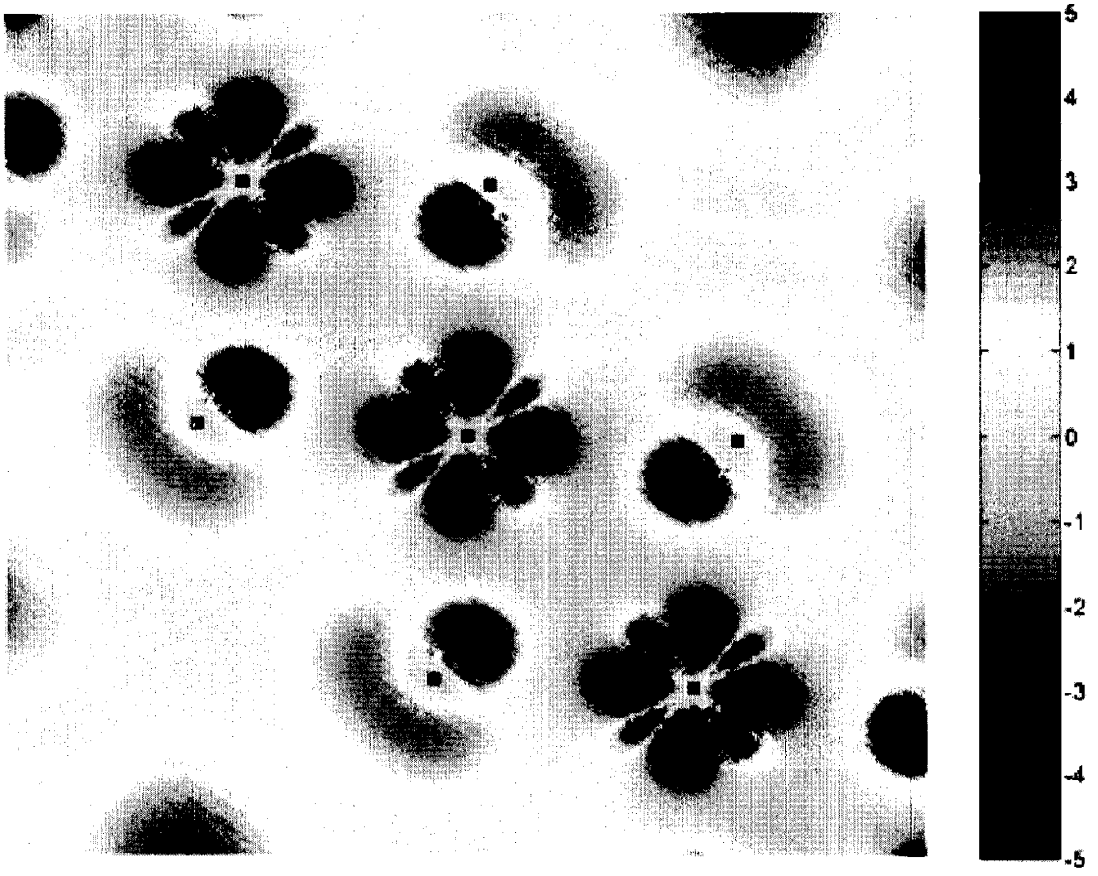

Figure 30 Total charge density difference of CoO_2 minus $LiCoO_2$. The approximate location of Li, Co, and O are denoted by white, black, and blue dots, respectively. The dark colors (ie. blue, purple) denote electron removal while light colors (ie. green, yellow, red) denote electron addition. Essentially, charge is removed from the t_{2g} orbital and the oxygen, and charge is added to the e_g orbital.

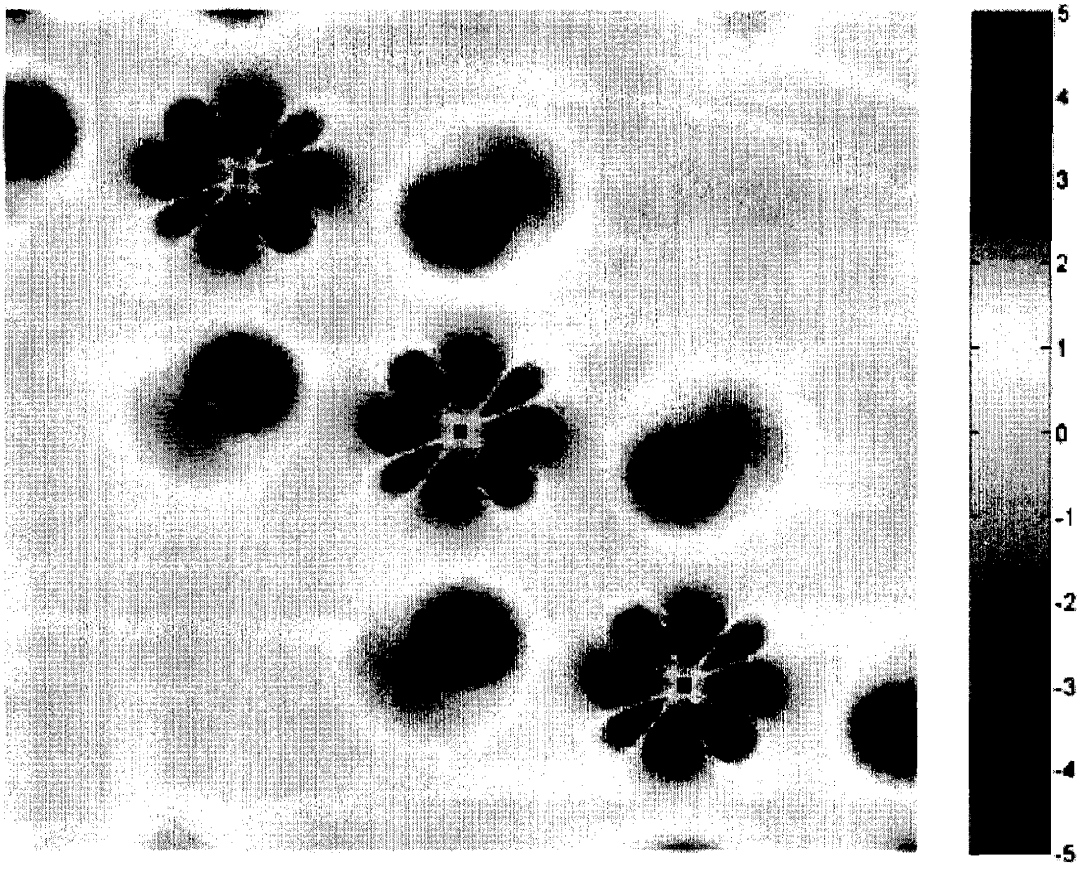

Figure 31 Total charge density difference of CoO_2 minus CoO_2+1e. Same conventions as previous figure.

5.6 Cluster Calculations

In this section, we reproduce the published configuration interaction cluster calculations[47,60] in greater detail. These calculations are used to predict the high energy satellite which is alternatively calculated using LDA+DMFT in Chapter 6. First we begin by defining the many-body Hamiltonian for the cluster.

$$\hat{H} = \frac{1}{2}\sum_{ijkl}\langle ij|V|kl\rangle d_i^+ d_j^+ d_l d_k + \sum_i \varepsilon_d d_i^+ d_i + \sum_i \varepsilon_p p_i^+ p_i + \sum_i t_i\left(p_i^+ d_i + d_i^+ p_i\right) - \sum_i^{t2g} 4Dq \cdot d_i^+ d_i + \sum_i^{eg} 6Dq \cdot d_i^+ d_i$$

where p_i and d_i are the destruction operators for the symmetrized oxygen p and Co d states, t_i is the hopping matrix element between Co and Oxygen, 10Dq is the crystal field splitting, and ε_p and ε_d are the bare energies for the oxygen *p* and Co *d* states. The only symmetrized *p* states used in this model are those with e_g and t_{2g} symmetry.

In order to solve this Hamiltonian, we shall choose a suitable many-body basis set in which the Hamiltonian will be diagonalized. For lucidity, we will begin by setting up the problem in the absence of multiplets (ie. no exchange) and crystal field splitting, and under the assumption that the different oxygen symmetries are equivalent. In this case, the ground state wave function of the N, N-1, N+1 particle systems can be expanded as follows:

$$|N\rangle = a_n \left|d^n\right\rangle + b_n \left|d^{n+1}\underline{L}\right\rangle + c_n \left|d^{n+2}\underline{L}^2\right\rangle$$

$$|N-1\rangle = a_{n-1} \left|d^{n-1}\right\rangle + b_{n-1} \left|d^{n}\underline{L}\right\rangle + c_{n-1} \left|d^{n+1}\underline{L}^2\right\rangle$$

$$|N+1\rangle = a_{n-1} \left|d^{n+1}\right\rangle + b_{n-1} \left|d^{n+2}\underline{L}\right\rangle + c_{n-1} \left|d^{n+3}\underline{L}^2\right\rangle$$

where a, b, and c are variational coefficients. This basis is by no means complete, but higher order configurations will be high in energy and will not have a significant effect on the spectrum. Given the above assumptions, we can now write a simple formula for the energy of a given configuration.

$$E\left(d^n L^m\right) = n\varepsilon_d + \frac{1}{2}\cdot U \cdot n(n-1) + m\varepsilon_p$$

Using this simple formula, we can find the relative energies of the different basis configurations for the respective systems.

$$E\left(d^{n+1}L^{m-1}\right) - E\left(d^n L^m\right) = \varepsilon_d - \varepsilon_p + Un \equiv \Delta$$

$$E\left(d^{n+2}L^{m-2}\right) - E\left(d^n L^m\right) = 2\varepsilon_d - 2\varepsilon_p + 2Un + U = 2\Delta + U$$

$$E\left(d^{n}L^{m-1}\right) - E\left(d^{n-1} L^m\right) = \varepsilon_d - \varepsilon_p + Un - U = \Delta - U$$

$$E\left(d^{n+1}L^{m-2}\right) - E\left(d^{n-1} L^m\right) = 2\varepsilon_d - 2\varepsilon_p + 2Un - U = 2\Delta - U$$

The Hamiltonian matrix can now be constructed for the N and N-1 particle system.

$$H(N)=\begin{bmatrix} E(d^n) & t & 0 \\ t & E(d^n)+\Delta & t \\ 0 & t & E(d^n)+2\Delta+U \end{bmatrix}$$

$$H(N-1)=\begin{bmatrix} E(d^{n-1}) & t & 0 \\ t & E(d^{n-1})+\Delta-U & t \\ 0 & t & E(d^{n-1})+2\Delta-U \end{bmatrix}$$

We see that up to a constant, the diagonal elements of the Hamiltonians are defined by Δ and U, and therefore the absolute values of ε_p and ε_d are not necessary. Only Δ is given in reference [47], and therefore the spectrum can only be determined to within a constant. The Hamiltonians can now be diagonalized to give the eigenvalues of the respective systems. In order to get the photoemission spectra, one needs to construct the imaginary part of the greens function, also known as the spectral function.

$$\rho(\omega)=\sum_i \langle N-1,i|d|N\rangle \delta(\omega-E_{gs}+E_i)+\sum_i \langle N+1,i|d^+|N\rangle \delta(\omega+E_{gs}-E_i)$$

In order to address this problem in a more realistic fashion, we will not introduce the above simplifications. Therefore, one needs to construct all the relevant symmetrized wavefunctions in order to create a realistic basis. This task is accomplished by following the rules of group theory[61]. The basis functions for the N-1 particle system are shown in Figure 32, and for the N particle system in Figure 33. For the N-1 particle system, only basis functions for the $^2T_{2g}\zeta$ irreducible representation are considered because all 5 other irreducible representations will be degenerate. Now the Hamiltonian matrix can be constructed. As shown above, the average energies of the multiplets are defined in terms of the charge transfer energy and *U*. A representative submatrix for the N and N-1 particle Hamiltonians using the generic basis from above is shown.

$$H(N)=\begin{bmatrix} \langle 1|H'|1\rangle & k_i t & 0 \\ k_i t & \langle 2|H'|2\rangle+\Delta & k_j t \\ 0 & k_j t & \langle 3|H'|3\rangle+2\Delta+U \end{bmatrix}$$

$$H(N-1)=\begin{bmatrix} \langle 1|H'|1\rangle & k_i t & 0 \\ k_i t & \langle 2|H'|2\rangle+\Delta-U & k_j t \\ 0 & k_j t & \langle 3|H'|3\rangle+2\Delta-U \end{bmatrix}$$

where

$$H' = \frac{1}{2}\sum_{ijkl}\langle ij|V|kl\rangle d_i^+ d_j^+ d_l d_k + \sum_i T_i\left(p_i^+ d_i + d_i^+ p_i\right) - \sum_i^{t2g} 4Dq \cdot d_i^+ d_i$$

$$+\sum_i^{eg} 6Dq \cdot d_i^+ d_i - \frac{1}{2}UN_d\left(N_d - 1\right)$$

k is some constant which depends on the particular basis states used in the matrix element, and N_d is the number operator for the *d* electrons. H' does not contain ε_p or ε_d as these are contained within Δ. Additionally, the last term in H' removes the average electron interaction, because this is already accounted for with Δ and U.

The resulting photoemission spectra for the N-1 particle system is shown in Figure 34. The occupancies are shown in N-1 and N particle systems are shown in Figure 35 and Figure 36, respectively. The main line of the N-1 particle system is composed of 0.22 d^5, 0.56 $d^6\underline{L}$, and 0.22 $d^7\underline{L}^2$. One of the reasons we repeated these calculations was to determine the specific nature of the $d^6\underline{L}$ state in the main line, which is not given in ref[47]. This configuration is overwhelmingly composed of the four different states $\left|t_{2g}^5 e_g^1 \underline{e_g}\right\rangle$, as indicated in Figure 35. Additionally, we find that the satellite is roughly 0.5 d^5 and 0.4 $d^7\underline{L}^2$

$$1.\left|t_{2g}^5\left({}^2T_{2g}\zeta\right)\right\rangle=\left|\zeta\eta\bar{\eta}\xi\bar{\xi}\right\rangle$$

$$2.\left|t_{2g}^6\underline{t}\left({}^2T_{1g}\zeta\right)\right\rangle=\left|\bar{\phi}_\zeta\zeta\eta\bar{\eta}\xi\bar{\xi}\right\rangle$$

$$3.\left|t_{2g}^5e_g\left({}^3T_{1g}\right)\underline{e_g}\left({}^2T_{2g}\zeta\right)\right\rangle=\frac{1}{\sqrt{6}}\left[\left|v\bar{\phi}_v\zeta\eta\bar{\eta}\xi\bar{\xi}\right\rangle+\left|\bar{v}\bar{\phi}_v\zeta\eta\bar{\eta}\xi\bar{\xi}\right\rangle-2\left|v\phi_v\zeta\eta\bar{\eta}\xi\bar{\xi}\right\rangle\right]$$

$$4.\left|t_{2g}^5e_g\left({}^3T_{2g}\right)\underline{e_g}\left({}^2T_{2g}\zeta\right)\right\rangle=\frac{1}{\sqrt{6}}\left[\left|u\bar{\phi}_u\zeta\eta\bar{\eta}\xi\bar{\xi}\right\rangle+\left|\bar{u}\bar{\phi}_u\zeta\eta\bar{\eta}\xi\bar{\xi}\right\rangle-2\left|u\phi_u\zeta\eta\bar{\eta}\xi\bar{\xi}\right\rangle\right]$$

$$5.\left|t_{2g}^5e_g\left({}^1T_{1g}\right)\underline{e_g}\left({}^2T_{2g}\zeta\right)\right\rangle=\frac{1}{\sqrt{2}}\left[\left|v\bar{\phi}_v\zeta\eta\bar{\eta}\xi\bar{\xi}\right\rangle-\left|\bar{v}\bar{\phi}_v\zeta\eta\bar{\eta}\xi\bar{\xi}\right\rangle\right]$$

$$6.\left|t_{2g}^5e_g\left({}^1T_{2g}\right)\underline{e_g}\left({}^2T_{2g}\zeta\right)\right\rangle=\frac{1}{\sqrt{2}}\left[\left|u\bar{\phi}_u\zeta\eta\bar{\eta}\xi\bar{\xi}\right\rangle-\left|\bar{u}\bar{\phi}_u\zeta\eta\bar{\eta}\xi\bar{\xi}\right\rangle\right]$$

$$7.\left|t_{2g}^6e_g\underline{e_gt_{2g}}\left({}^1T_{1g}\right)\left({}^2T_{2g}\zeta\right)\right\rangle=\frac{1}{\sqrt{2}}\left[\left|v\bar{\phi}_\zeta\phi_v\zeta\bar{\zeta}\eta\bar{\eta}\xi\bar{\xi}\right\rangle-\left|v\phi_\zeta\bar{\phi}_v\zeta\bar{\zeta}\eta\bar{\eta}\xi\bar{\xi}\right\rangle\right]$$

$$8.\left|t_{2g}^6e_g\underline{e_gt_{2g}}\left({}^1T_{2g}\right)\left({}^2T_{2g}\zeta\right)\right\rangle=\frac{1}{\sqrt{2}}\left[\left|u\bar{\phi}_\zeta\phi_u\zeta\bar{\zeta}\eta\bar{\eta}\xi\bar{\xi}\right\rangle-\left|u\phi_\zeta\bar{\phi}_u\zeta\bar{\zeta}\eta\bar{\eta}\xi\bar{\xi}\right\rangle\right]$$

$$9.\left|t_{2g}^6e_g\underline{e_gt_{2g}}\left({}^3T_{1g}\right)\left({}^2T_{2g}\zeta\right)\right\rangle=\frac{1}{\sqrt{6}}\left[\left|v\bar{\phi}_\zeta\phi_v\zeta\bar{\zeta}\eta\bar{\eta}\xi\bar{\xi}\right\rangle+\left|v\phi_\zeta\bar{\phi}_v\zeta\bar{\zeta}\eta\bar{\eta}\xi\bar{\xi}\right\rangle-2\left|v\bar{\phi}_\zeta\bar{\phi}_v\zeta\bar{\zeta}\eta\bar{\eta}\xi\bar{\xi}\right\rangle\right]$$

$$10.\left|t_{2g}^6e_g\underline{e_gt_{2g}}\left({}^3T_{2g}\right)\left({}^2T_{2g}\zeta\right)\right\rangle=\frac{1}{\sqrt{6}}\left[\left|u\bar{\phi}_\zeta\phi_u\zeta\bar{\zeta}\eta\bar{\eta}\xi\bar{\xi}\right\rangle+\left|u\phi_\zeta\bar{\phi}_u\zeta\bar{\zeta}\eta\bar{\eta}\xi\bar{\xi}\right\rangle-2\left|u\bar{\phi}_\zeta\bar{\phi}_u\zeta\bar{\zeta}\eta\bar{\eta}\xi\bar{\xi}\right\rangle\right]$$

$$11.\left|t_{2g}^5e_g^2\left({}^4T_{1g}\right)\underline{e_g^2}\left({}^2T_{2g}\zeta\right)\right\rangle=\frac{1}{3\sqrt{2}}\begin{bmatrix}\left|\bar{u}v\bar{O}_uO_v\zeta\eta\bar{\eta}\xi\bar{\xi}\right\rangle+\left|u\bar{v}\bar{O}_uO_v\zeta\eta\bar{\eta}\xi\bar{\xi}\right\rangle+\left|\bar{u}v\bar{O}_uO_v\zeta\eta\bar{\eta}\xi\bar{\xi}\right\rangle-\left|\bar{u}v\bar{O}_u\bar{O}_v\zeta\eta\bar{\eta}\xi\bar{\xi}\right\rangle\\-\left|u\bar{v}\bar{O}_uO_v\zeta\eta\bar{\eta}\xi\bar{\xi}\right\rangle-\left|uv\bar{O}_u\bar{O}_v\zeta\eta\bar{\eta}\xi\bar{\xi}\right\rangle-\left|\bar{u}v\bar{O}_u\bar{O}_v\zeta\eta\bar{\eta}\xi\bar{\xi}\right\rangle-\left|u\bar{v}\bar{O}_u\bar{O}_v\zeta\eta\bar{\eta}\xi\bar{\xi}\right\rangle\\-\left|uvO_u\bar{O}_v\zeta\eta\bar{\eta}\xi\bar{\xi}\right\rangle+3\left|uv\bar{O}_u\bar{O}_v\zeta\eta\bar{\eta}\xi\bar{\xi}\right\rangle\end{bmatrix}$$

$$12.\left|t_{2g}^5e_g^2\left({}^3A_{2g}\right)\left({}^2T_{1g}\right)\underline{e_g^2}\left({}^3A_{2g}\right)\left({}^2T_{2g}\zeta\right)\right\rangle=\frac{1}{6}\begin{bmatrix}4\left|\bar{u}\bar{v}O_uO_v\zeta\eta\bar{\eta}\xi\bar{\xi}\right\rangle-2\left|\bar{u}vO_uO_v\zeta\eta\bar{\eta}\xi\bar{\xi}\right\rangle-2\left|u\bar{v}O_uO_v\zeta\eta\bar{\eta}\xi\bar{\xi}\right\rangle\\+2\left|uvO_u\bar{O}_v\zeta\eta\bar{\eta}\xi\bar{\xi}\right\rangle-\left|\bar{u}v\bar{O}_uO_v\zeta\eta\bar{\eta}\xi\bar{\xi}\right\rangle-\left|u\bar{v}\bar{O}_uO_v\zeta\eta\bar{\eta}\xi\bar{\xi}\right\rangle\\+2\left|uvO_u\bar{O}_v\zeta\eta\bar{\eta}\xi\bar{\xi}\right\rangle-\left|\bar{u}vO_u\bar{O}_v\zeta\eta\bar{\eta}\xi\bar{\xi}\right\rangle-\left|u\bar{v}O_u\bar{O}_v\zeta\eta\bar{\eta}\xi\bar{\xi}\right\rangle\end{bmatrix}$$

$$13.\left|t_{2g}^5e_g^2\left({}^1E_g\right)\left({}^2T_{1g}\right)\underline{e_g^2}\left({}^1E_g\right)\left({}^2T_{2g}\zeta\right)\right\rangle=\frac{1}{2}\left[\left|u\bar{v}O_u\bar{O}_v\zeta\eta\bar{\eta}\xi\bar{\xi}\right\rangle-\left|\bar{u}vO_u\bar{O}_v\zeta\eta\bar{\eta}\xi\bar{\xi}\right\rangle-\left|u\bar{v}\bar{O}_uO_v\zeta\eta\bar{\eta}\xi\bar{\xi}\right\rangle+\left|\bar{u}v\bar{O}_uO_v\zeta\eta\bar{\eta}\xi\bar{\xi}\right\rangle\right]$$

$$14.\left|t_{2g}^5e_g^2\left({}^1A_{1g}\right)\left({}^2T_{2g}\right)\underline{e_g^2}\left({}^1A_{1g}\right)\left({}^2T_{2g}\zeta\right)\right\rangle=\frac{1}{2}\left[\left|u\bar{u}O_u\bar{O}_v\zeta\eta\bar{\eta}\xi\bar{\xi}\right\rangle+\left|u\bar{u}O_v\bar{O}_v\zeta\eta\bar{\eta}\xi\bar{\xi}\right\rangle+\left|v\bar{v}O_u\bar{O}_u\zeta\eta\bar{\eta}\xi\bar{\xi}\right\rangle+\left|v\bar{v}O_v\bar{O}_v\zeta\eta\bar{\eta}\xi\bar{\xi}\right\rangle\right]$$

$$15.\left|t_{2g}^5e_g^2\left({}^1E_g\right)\left({}^2T_{2g}\right)\underline{e_g^2}\left({}^1A_{1g}\right)\left({}^2T_{2g}\zeta\right)\right\rangle=\frac{1}{2}\left[\left|u\bar{u}O_u\bar{O}_u\zeta\eta\bar{\eta}\xi\bar{\xi}\right\rangle+\left|u\bar{u}O_v\bar{O}_v\zeta\eta\bar{\eta}\xi\bar{\xi}\right\rangle+\left|v\bar{v}O_u\bar{O}_u\zeta\eta\bar{\eta}\xi\bar{\xi}\right\rangle+\left|v\bar{v}O_v\bar{O}_v\zeta\eta\bar{\eta}\xi\bar{\xi}\right\rangle\right]$$

$$16.\left|t_{2g}^5e_g^2\left({}^1A_{1g}\right)\left({}^2T_{2g}\right)\underline{e_g^2}\left({}^1E_g\right)\left({}^2T_{2g}\zeta\right)\right\rangle=\frac{1}{2}\left[\left|u\bar{u}O_u\bar{O}_u\zeta\eta\bar{\eta}\xi\bar{\xi}\right\rangle+\left|u\bar{u}O_v\bar{O}_v\zeta\eta\bar{\eta}\xi\bar{\xi}\right\rangle+\left|v\bar{v}O_u\bar{O}_u\zeta\eta\bar{\eta}\xi\bar{\xi}\right\rangle+\left|v\bar{v}O_v\bar{O}_v\zeta\eta\bar{\eta}\xi\bar{\xi}\right\rangle\right]$$

$$17.\left|t_{2g}^5e_g^2\left({}^1E_g\right)\left({}^2T_{2g}\right)\underline{e_g^2}\left({}^1E_g\right)\left({}^2T_{2g}\zeta\right)\right\rangle=\frac{1}{2}\left[\left|u\bar{u}O_u\bar{O}_u\zeta\eta\bar{\eta}\xi\bar{\xi}\right\rangle+\left|u\bar{u}O_v\bar{O}_v\zeta\eta\bar{\eta}\xi\bar{\xi}\right\rangle+\left|v\bar{v}O_u\bar{O}_u\zeta\eta\bar{\eta}\xi\bar{\xi}\right\rangle+\left|v\bar{v}O_v\bar{O}_v\zeta\eta\bar{\eta}\xi\bar{\xi}\right\rangle\right]$$

$$18.\left|t_{2g}^5e_g^2\left({}^3A_{2g}\right)\left({}^2T_{1g}\right)\underline{e_g^2}\left({}^1E_g\right)\left({}^2T_{2g}\zeta\right)\right\rangle=\frac{1}{2\sqrt{3}}\begin{bmatrix}-2\left|uvO_u\bar{O}_v\zeta\eta\bar{\eta}\xi\bar{\xi}\right\rangle+\left|\bar{u}vO_u\bar{O}_v\zeta\eta\bar{\eta}\xi\bar{\xi}\right\rangle+\left|u\bar{v}O_u\bar{O}_v\zeta\eta\bar{\eta}\xi\bar{\xi}\right\rangle\\+2\left|uv\bar{O}_uO_v\zeta\eta\bar{\eta}\xi\bar{\xi}\right\rangle-\left|\bar{u}v\bar{O}_uO_v\zeta\eta\bar{\eta}\xi\bar{\xi}\right\rangle-\left|u\bar{v}\bar{O}_uO_v\zeta\eta\bar{\eta}\xi\bar{\xi}\right\rangle\end{bmatrix}$$

$$19.\left|t_{2g}^5e_g^2\left({}^1E_g\right)\left({}^2T_{1g}\right)\underline{e_g^2}\left({}^3A_{2g}\right)\left({}^2T_{2g}\zeta\right)\right\rangle=\frac{1}{2\sqrt{3}}\begin{bmatrix}2\left|u\bar{v}O_u\bar{O}_v\zeta\eta\bar{\eta}\xi\bar{\xi}\right\rangle-2\left|\bar{u}vO_u\bar{O}_v\zeta\eta\bar{\eta}\xi\bar{\xi}\right\rangle-\left|u\bar{v}\bar{O}_uO_v\zeta\eta\bar{\eta}\xi\bar{\xi}\right\rangle\\+\left|\bar{u}v\bar{O}_uO_v\zeta\eta\bar{\eta}\xi\bar{\xi}\right\rangle-\left|u\bar{v}O_u\bar{O}_v\zeta\eta\bar{\eta}\xi\bar{\xi}\right\rangle-\left|\bar{u}vO_u\bar{O}_v\zeta\eta\bar{\eta}\xi\bar{\xi}\right\rangle\end{bmatrix}$$

Figure 32 Symmetrized wave functions for the N-1 particle system in the cluster calculation for $LiCOO_2$. The Co *d* states are all in the electron representation, while the oxygen *p* states are in either the electron or hole representation. *O* represents an *p* electron, while ϕ represents a *p* hole. ζ=xy, η=xz, ξ=yz, u=z^2, and v=x^2-y^2. The presence of a bar indicates low spin.

$$1.\left|t_{2g}^{6}\left({}^{1}A_{1g}\right)\right\rangle=\left|\zeta\bar{\zeta}\eta\bar{\eta}\xi\bar{\xi}\right\rangle$$

$$2.\left|t_{2g}^{6}e_g\underline{e_g}\left({}^{1}A_{1g}\right)\right\rangle=\frac{1}{2}\left[\left|u\phi_u\zeta\bar{\zeta}\eta\bar{\eta}\xi\bar{\xi}\right\rangle-\left|\bar{u}\bar{\phi}_u\zeta\bar{\zeta}\eta\bar{\eta}\xi\bar{\xi}\right\rangle+\left|v\phi_v\zeta\bar{\zeta}\eta\bar{\eta}\xi\bar{\xi}\right\rangle-\left|v\phi_v\zeta\bar{\zeta}\eta\bar{\eta}\xi\bar{\xi}\right\rangle\right]$$

$$3.\left|t_{2g}^{6}e_g^{2}\left({}^{3}A_{2g}\right)\underline{e_g^{2}}\left({}^{1}A_{1g}\right)\right\rangle=\frac{1}{2\sqrt{3}}\begin{bmatrix}-2\left|uv\overline{O_u}\,\overline{O_v}\zeta\bar{\zeta}\eta\bar{\eta}\xi\bar{\xi}\right\rangle-2\left|\bar{u}\bar{v}O_uO_v\zeta\bar{\zeta}\eta\bar{\eta}\xi\bar{\xi}\right\rangle+\left|u\bar{v}\overline{O_u}O_v\zeta\bar{\zeta}\eta\bar{\eta}\xi\bar{\xi}\right\rangle\\+\left|u\bar{v}\overline{O_u}O_v\zeta\bar{\zeta}\eta\bar{\eta}\xi\bar{\xi}\right\rangle+\left|\bar{u}vO_u\overline{O_v}\zeta\bar{\zeta}\eta\bar{\eta}\xi\bar{\xi}\right\rangle+\left|\bar{u}v\overline{O_u}O_v\zeta\bar{\zeta}\eta\bar{\eta}\xi\bar{\xi}\right\rangle\end{bmatrix}$$

$$4.\left|t_{2g}^{6}e_g^{2}\left({}^{1}A_{1g}\right)\underline{e_g^{2}}\left({}^{1}A_{1g}\right)\right\rangle=\frac{1}{2}\left[\left|u\bar{u}O_u\overline{O_u}\zeta\bar{\zeta}\eta\bar{\eta}\xi\bar{\xi}\right\rangle+\left|u\bar{u}O_v\overline{O_v}\zeta\bar{\zeta}\eta\bar{\eta}\xi\bar{\xi}\right\rangle+\left|v\bar{v}O_u\overline{O_u}\zeta\bar{\zeta}\eta\bar{\eta}\xi\bar{\xi}\right\rangle+\left|v\bar{v}O_v\overline{O_v}\zeta\bar{\zeta}\eta\bar{\eta}\xi\bar{\xi}\right\rangle\right]$$

$$5.\left|t_{2g}^{6}e_g^{2}\left({}^{1}E_g\right)\underline{e_g^{2}}\left({}^{1}A_{1g}\right)\right\rangle=\frac{1}{2\sqrt{2}}\begin{bmatrix}\left|u\bar{u}O_u\overline{O_u}\zeta\bar{\zeta}\eta\bar{\eta}\xi\bar{\xi}\right\rangle-\left|u\bar{u}O_v\overline{O_v}\zeta\bar{\zeta}\eta\bar{\eta}\xi\bar{\xi}\right\rangle-\left|v\bar{v}O_u\overline{O_u}\zeta\bar{\zeta}\eta\bar{\eta}\xi\bar{\xi}\right\rangle+\left|v\bar{v}O_v\overline{O_v}\zeta\bar{\zeta}\eta\bar{\eta}\xi\bar{\xi}\right\rangle\\+\left|u\bar{v}O_u\overline{O_v}\zeta\bar{\zeta}\eta\bar{\eta}\xi\bar{\xi}\right\rangle-\left|u\bar{v}\overline{O_u}O_v\zeta\bar{\zeta}\eta\bar{\eta}\xi\bar{\xi}\right\rangle-\left|\bar{u}vO_u\overline{O_v}\zeta\bar{\zeta}\eta\bar{\eta}\xi\bar{\xi}\right\rangle+\left|\bar{u}v\overline{O_u}O_v\zeta\bar{\zeta}\eta\bar{\eta}\xi\bar{\xi}\right\rangle\end{bmatrix}$$

Figure 33 Symmetrized wave functions for the N particle system in the cluster calculation for $LiCOO_2$. Same conventions as previous figure.

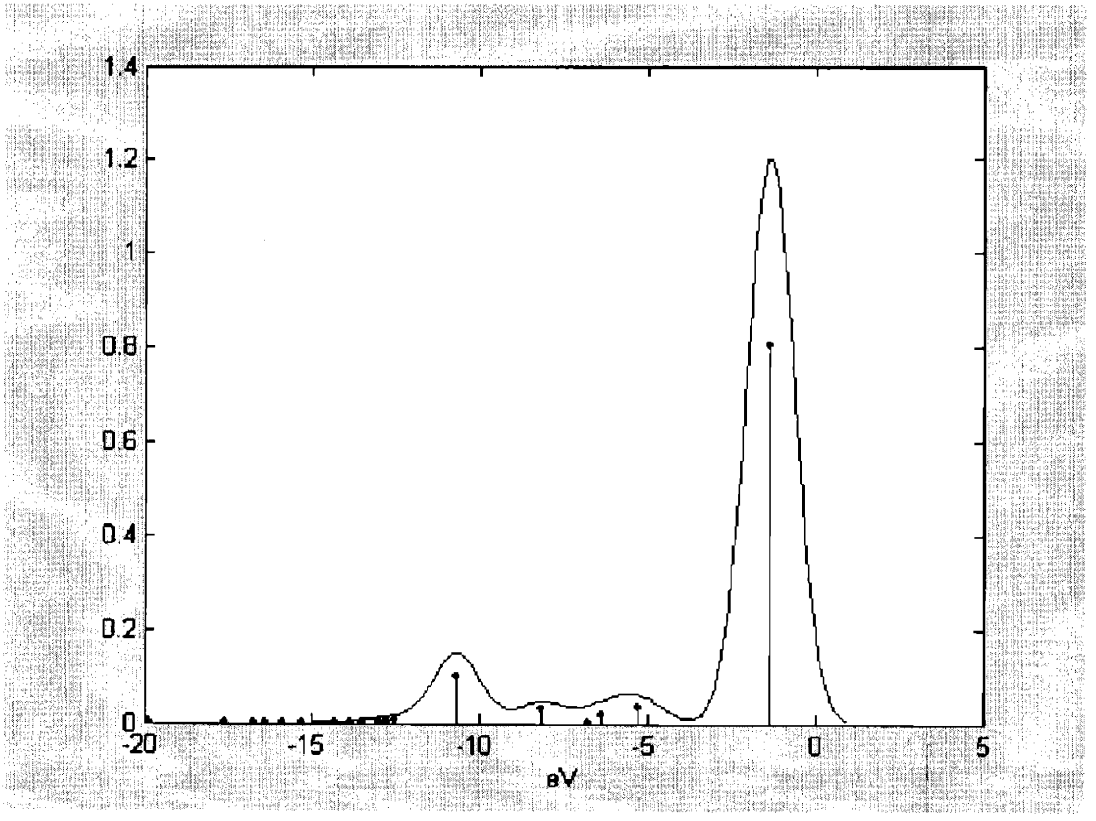

Figure 34 Calculated removal spectrum for $LiCOO_2$.

	E1	E2	E3	E4	E5	E6	E7	E8	E9	E10	E11	E12	E13	E14	E15	E16	E17	E18	E19
state1	0.22	0.00	0.01	0.00	0.02	0.49	0.06	0.00	0.00	0.03	0.00	0.02	0.00	0.01	0.01	0.00	0.00	0.02	0.12
state2	0.05	0.59	0.01	0.00	0.00	0.00	0.00	0.00	0.00	0.00	0.00	0.00	0.00	0.01	0.05	0.04	0.20	0.04	0.02
state3	0.25	0.05	0.25	0.11	0.01	0.00	0.01	0.00	0.00	0.00	0.00	0.00	0.02	0.12	0.01	0.00	0.01	0.08	0.08
state4	0.18	0.01	0.06	0.40	0.01	0.00	0.01	0.00	0.00	0.01	0.00	0.04	0.03	0.01	0.01	0.06	0.02	0.02	0.15
state5	0.06	0.00	0.37	0.20	0.04	0.01	0.00	0.00	0.00	0.00	0.00	0.01	0.00	0.13	0.08	0.02	0.00	0.05	0.04
state6	0.03	0.00	0.01	0.00	0.54	0.03	0.00	0.00	0.00	0.00	0.01	0.00	0.01	0.02	0.00	0.16	0.06	0.02	0.11
state7	0.01	0.03	0.04	0.00	0.00	0.00	0.19	0.51	0.05	0.04	0.00	0.00	0.01	0.03	0.03	0.01	0.04	0.01	0.00
state8	0.01	0.04	0.00	0.02	0.02	0.00	0.19	0.36	0.15	0.05	0.02	0.03	0.01	0.00	0.01	0.00	0.09	0.00	0.01
state9	0.01	0.11	0.00	0.02	0.01	0.01	0.18	0.00	0.12	0.22	0.01	0.04	0.02	0.03	0.01	0.02	0.13	0.05	0.01
state10	0.01	0.12	0.00	0.00	0.02	0.03	0.00	0.01	0.49	0.02	0.01	0.00	0.01	0.02	0.05	0.06	0.11	0.01	0.02
state11	0.09	0.04	0.04	0.06	0.04	0.31	0.13	0.00	0.00	0.06	0.00	0.06	0.00	0.10	0.01	0.02	0.00	0.00	0.05
state12	0.02	0.00	0.09	0.04	0.07	0.11	0.01	0.00	0.05	0.06	0.00	0.01	0.00	0.28	0.05	0.07	0.07	0.01	0.07
state13	0.03	0.01	0.00	0.00	0.00	0.01	0.07	0.00	0.01	0.12	0.22	0.08	0.30	0.05	0.03	0.00	0.01	0.01	0.06
state14	0.02	0.00	0.00	0.00	0.00	0.00	0.01	0.01	0.01	0.00	0.03	0.09	0.16	0.01	0.25	0.19	0.07	0.00	0.15
state15	0.00	0.00	0.01	0.09	0.03	0.00	0.00	0.02	0.04	0.07	0.07	0.09	0.21	0.03	0.20	0.03	0.00	0.09	0.01
state16	0.00	0.00	0.01	0.05	0.02	0.00	0.01	0.01	0.00	0.02	0.08	0.04	0.03	0.00	0.03	0.02	0.09	0.57	0.02
state17	0.03	0.01	0.00	0.00	0.00	0.01	0.12	0.01	0.01	0.22	0.28	0.00	0.09	0.02	0.10	0.00	0.01	0.03	0.08
state18	0.00	0.00	0.06	0.00	0.09	0.00	0.01	0.06	0.06	0.03	0.13	0.25	0.03	0.09	0.04	0.12	0.04	0.00	0.00
state19	0.00	0.00	0.06	0.00	0.07	0.00	0.00	0.01	0.00	0.05	0.14	0.24	0.07	0.04	0.05	0.20	0.06	0.00	0.00

Figure 35 Occupancies for the N-1 system. The first column corresponds to the main line, while the sixth column corresponds to the satellite.

	E1	E2	E3	E4	E5
state1	0.491	0.469	0.006	0.006	0.027
state2	0.435	0.268	0.025	0.036	0.235
state3	0.043	0.176	0.565	0.075	0.141
state4	0.009	0.021	0.021	0.56	0.389
state5	0.022	0.065	0.383	0.323	0.207

Figure 36 Occupancies for the N particle system.

5.7 Overview

In this chapter we presented background material on Li_xCoO_2. Photoemission data displays a satellite which is not captured within LDA, but is predicted by empirical cluster calculations which are repeated in detail within this chapter. Predicting this satellite using LDA+DMFT, a nearly first-principles technique, is the focus of chapter 8. XAS data indicates notable changes in the oxygen 2*s* absorption spectra while subtler changes in the Co 2*p* absorption spectra as a function of Li removal. This appears to be consistent with the rehybridization mechanism, in which hole density doped into the t_{2g} states is compensated by electron density in the e_g states and hole density on the oxygen states. The band structure and density of states are presented for $LiCoO_2$ and CoO_2.

Perhaps the most interesting feature is the flat a_{1g} band in $LiCoO_2$, which will greatly enhance the localizability of a hole.

The experimental observation of the metal-insulator transition for $0.75 < x < 0.95$ is discussed in terms of the XRD, conductivity, and NMR data. Two distinct phases are observed with the same symmetry and similar structural parameters. The $x = 0.75$ phase displays a Knight-shifted NMR signal with essentially no activation in the conductivity, while the $x = 0.95$ phase displays a non-shifted NMR peak and an activated conductivity. This evidences a first order metal-insulator transition, although the mechanism of insulating state and the transition has not yet been explained. This question is addressed in chapter 7.

Chapter 6

The Role of Hybridization in Na_xCoO_2 and the Effect of Hydration

Abstract

Density functional theory (DFT) within the local density approximation (LDA) is used to understand the electronic properties of $Na_{1/3}CoO_2$ and $Na_{1/3}CoO_2(H_2O)_{4/3}$, which was recently found to be superconducting[42]. Comparing the LDA charge density of CoO_2 and the Na doped phases indicates that doping does not simply add electrons to the t_{2g} states. In fact, the electron added in the t_{2g} state is dressed by hole density in the e_g state and electron density in the oxygen states via rehybridization. In order to fully understand this phenomenon, a simple extension of the Hubbard Hamiltonian is proposed and solved using the dynamical mean-field theory (DMFT). This simple model confirms that the rehybridization is driven by a competition between the on-site coulomb interaction and the hybridization. In addition, we find that the presence of e_g-oxygen hybridization effectively screens the low energy excitations. To address the role that water plays in creating the superconducting state, we compare the LDA band structure of $Na_{1/3}CoO_2$ and its hydrated counterpart. This demonstrates that hydration does cause the electronic structure to become more two-dimensional.

Na_xCoO_2 was originally investigated as a rechargeable battery material[62]. More recently, Na_xCoO_2 and its hydrated counterpart are receiving renewed interest due to the discovery of superconductivity[42], in addition to anomalous thermoelectric properties[63]. Understanding these properties requires a detailed understanding of the low energy Hamiltonian in this material. While there are many interesting parallels between the cuprates and Na_xCoO_2, the details of the electronic structure are quite different. In Na_xCoO_2, the Fermi level lies within the t_{2g} states, with x=1 corresponding to a band insulator with filled t_{2g} states and x=0 corresponding to one t_{2g} hole per cobalt (possibly a Mott insulator). One of the useful steps forward in understanding the cuprates was the work of Zhang and Rice, in which they derived an effective one band model [64]. Initial studies of the low energy physics of Na_xCoO_2 have assumed a one band model[65-67], given that the octahedra in this structure are distorted and the t_{2g} levels are split into a 1-fold a_{1g} level and a 2-fold e_g' level (not to be confused with the usual e_g levels) [44]. However, the potential influence of the e_g orbitals and the oxygen orbitals on the low energy physics has not yet been addressed.

Na_xCoO_2 crystallizes in a layered structure, in which the layers are two-dimensional triangular lattices of a given species. The layers alternate as Na-O-Co-O and this pattern is repeated. Both the Na and the Co reside in sites which are coordinated by distorted oxygen octahedra. Insertion of water causes the oxygen layers to be pried apart, resulting in an even more two-dimensional-like structure [42]. Co exists in the low spin state due to the appreciable crystal field splitting. When x<1 Co is in a mixed valence state, Co^{3+}/Co^{4+}, yielding an average electronic configuration t_{2g}^{6-x}. However, the large overlap of the e_g and the oxygen states creates strong hybridization and therefore an appreciable occupation of the e_g states and hole density on the oxygen states.

Previous density functional theory (DFT) calculations addressing Na_xCoO_2 focused on the magnetic properties, in addition to rationalizing the transport properties in terms of the LDA density-of-states [68, 69]. However, hydration was not explicitly considered. In this letter, we present first-principles calculations of $Na_{1/3}CoO_2$ and $Na_{1/3}CoO_2(H_2O)_{4/3}$. We demonstrate that the naïve picture of adding electrons to the t_{2g} states when doping CoO_2 with Na does not accurately describe the physics of Na_xCoO_2.

DFT calculations within the local density approximation (LDA) predict that Na doping adds electrons to the t_{2g} states, in addition to hole density in the e_g state and electron density in the oxygen states. Additionally, we demonstrate that the presence of the e_g-oxygen hybridization screens the low energy excitations of the system.

All LDA calculations were performed using the *Vienna Ab-initio Simulation Package* (VASP) [70, 71]. VASP solves the Kohn-Sham equations using projector augmented wave pseudopotentials [72, 73] and a plane wave basis set. A cut-off energy of 600 *eV* was chosen and k-point meshes of 6x6x3 were used for all cells. Experimental structural parameters were taken as a starting point for full structural relaxations[74, 75]. LDA calculations were performed for $Na_{1/3}CoO_2$ and $Na_{1/3}CoO_2(H_2O)_{4/3}$. The ordering of the Na atoms has been determined for both structures, and the ordering of the water molecules has been narrowed to a few possibilities [74, 75]. The Na atoms are four-fold coordinated by the water molecules, with two water molecules above and two below. However, there are six possible sites above and below the Na atom which may accommodate the water molecule. Two possibilities were suggested by Jorgensen et al[75] and we selected the more symmetric of the two configurations in which two opposing sites above the Na and the mirror image of the sites below the Na are occupied. Regardless of whether or not this particular ordering happens to be the ground state, the qualitative effect should be similar.

The LDA bands for $Na_{1/3}CoO_2$ and $Na_{1/3}CoO_2(H_2O)_{4/3}$ are presented in Figure 37. In both cases, a stable moment of 2/3 Bohr magnetons per formula unit is found. The respective bandstructures demonstrate that the t_{2g} bands are similar, illustrating that hydration does not have any dramatic effect on the low energy physics. In both cases the dispersion in the *z* direction is small, which is a result of the two-dimensional nature of both the hydrated and non-hydrated compound. One notable difference is that the bands in the hydrated case display less splitting due to interlayer coupling at any given k-point. Given the supercell that we have chosen, only 9 t_{2g} bands would be distinguishable at a generic k-point if the layers did *not* interact (ie. the unit cell contains 3 Co basis atoms per plane). Interlayer coupling will induce band splitting, and this is more pronounced for $Na_{1/3}CoO_2$ than $Na_{1/3}CoO_2(H_2O)_{4/3}$. This reflects the fact that the layers are more isolated in the hydrated case, and hence more two-dimensional, which is commonly believed to

be an important ingredient of superconductivity in the cuprates[76]. It might be argued that the difference in band the structures are small, but it may still be relevant considering that the superconducting transition temperature is roughly 4 Kelvin.

Upon doping CoO_2 with Na, the Na will largely donate its electron at the Fermi energy. Therefore the changes in the ground state upon doping should qualitatively resemble the nature of the low energy excitations of the system. Given that the LDA DOS for Na_xCoO_2 shows the Fermi energy to lie within the t_{2g} states, which only have a relatively small mixing with oxygen, one might expect that the electron addition state upon doping is some linear combination of t_{2g} orbitals in addition to some small oxygen character. We shall demonstrate that this is not true, indicating that the LDA bands are behaving in an extremely non-rigid fashion. In order to accurately characterize the changes in the ground state upon doping CoO_2, it is useful to plot the charge density which has been added to the system. This can be done by subtracting the charge density of CoO_2 from that of $Na_{1/3}CoO_2$ calculated with the same structural parameters. This approach has been used frequently in studies of Li_xCoO_2 [38].

The difference in charge density between CoO_2 and $Na_{1/3}CoO_2$ is shown in Figure 38, which illustrates that the addition states are not simply t_{2g} orbitals. In fact, electron density is added to the t_{2g} states, hole density is added to the e_g states, and electron density is added to the oxygen states. This can be explained intuitively as a multi-step process, and this hypothesis will be justified below. LDA predicts an appreciable occupation of the e_g orbitals for CoO_2, roughly 1.6 electrons in a 1 Å sphere around Co, due to the large hybridization between the directly overlapping oxygen and e_g states. When charge is added to the system, electron density in the t_{2g} orbitals will increase causing an increase of the Co on–site coulomb repulsion. The on-site coulomb repulsion can be minimized by unmixing the oxygen and e_g orbitals in order to decrease the occupation of the e_g orbitals. Therefore, this rehybridization mechanism is a *competition* between the e_g-oxygen hybridization and the Co on-site coulomb interaction. Clearly, this logic can be inverted to explain the behavior of $Na_{1/3}CoO_2$ when Na is removed and holes are introduced into the system. In this case, holes are introduced into the t_{2g} states, in addition to electrons in the e_g states and holes in the oxygen states. The system increases the hybridization, and therefore the occupation of the e_g orbitals, because there is less t_{2g}

density to interact with e_g density. One can think of the rehybridization as a quasiparticle in which the particle (electron or hole) in the t_{2g} states has been dressed by a rehybridization cloud. A more quantitative analysis of the effect can be given by integrating the change in charge density within a 1 Å spheres centered on each atom. The oxygens gain 0.73 electrons per unit cell, while Co only gains 0.12 electrons per unit cell due to the rehybridization mechanism. It should be noted that the Na potential clearly does have a notable effect on the rehybridization. The oxygen orbitals nearest the Na are preferentially occupied in order to more effectively screen the Na potential.

Hints of this rehybridization effect were first noticed computationally in a study of Li_xTiS_2 over 20 years ago[77]. The authors note that most of the net incoming charge ends up on the Sulfur as Li is added to the material. Studies of Li_xCoO_2 characterized this phenomena much more clearly[38, 78]. Wolverton and Zunger made a key step in understanding this phenomenon by suggesting that it is driven by a need to minimize the potential effect of the strong on-site coulomb interactions and that it is similar to what is observed for transition metal impurities in semiconductors[78]. We wish to emphasize that this phenomena is a competition between the on-site coulomb repulsion and the hybridization, and that the degree to which the rehybridization occurs will depend on the relative magnitudes of the parameters of the particular material at hand. This effect is likely to occur in many other transition metal oxides in which electrons or holes are being doped into the t_{2g} states, such as Na_xTiO_2, Li_xVO_2. The results from X-ray Absorption experiments for Li_xCoO_2 and Na_xCoO_2 are consistent with the rehybridization mechanism[51-54]. The Co *2p* signal shows little variation as a function of doping, while the oxygen *1s* signal shows strong changes. This is in agreement with the observation that the rehybridization mechanism causes the average valence of the transition metal to remain relatively constant, while a net hole is formed on the oxygen.

While LDA gives an indication of the addition state, it cannot even qualitatively characterize the low energy excitations of the system when the electronic correlations are strong. If the rehybridization mechanism is indeed the result of a competition between hybridization and the on-site coulomb interaction, one should be able to capture this effect within a Hubbard-like model. The qualitative effects of the hybridization on the

low energy excitations may then be explored within the modified Hubbard model. Consider the following model Hamiltonian:

$$H = \sum_{i,\sigma}\left[\varepsilon_p p^{\dagger}_{i,\sigma}p_{i,\sigma} + \varepsilon_e e^{\dagger}_{i,\sigma}e_{i,\sigma} + T_{p-e}\left(e^{\dagger}_{i,\sigma}p_{i,\sigma} + p^{\dagger}_{i,\sigma}e_{i,\sigma}\right)\right] + \sum_{i,j,\sigma} w_{i,j}t^{\dagger}_{i,\sigma}t_{j,\sigma}$$
$$+U\sum_{i,\sigma}\left[e^{\dagger}_{i,\sigma}e_{i,\sigma}t^{\dagger}_{i,\sigma}t_{i,\sigma} + t^{\dagger}_{i,\uparrow}t_{i,\uparrow}t^{\dagger}_{i,\downarrow}t_{i,\downarrow} + e^{\dagger}_{i,\uparrow}e_{i,\uparrow}e^{\dagger}_{i,\downarrow}e_{i,\downarrow}\right] - \mu\sum_{i,\sigma}\left[p^{\dagger}_{i,\sigma}p_{i,\sigma} + e^{\dagger}_{i,\sigma}e_{i,\sigma} + t^{\dagger}_{i,\sigma}t_{i,\sigma}\right] \quad (1)$$

This model contains three orbitals (*p, t, e*) which can be analogously thought of as the oxygen *p* orbitals, the transition metal t_{2g} orbitals, and the transition metal e_g orbitals. The respective annihilation operators are denoted as *p, e,* and *t*. We only allow for hybridization between the *p* orbital and the *e* orbital as the oxygen orbitals hybridize much more strongly with the e_g orbitals than the t_{2g} for transition metals in an octahedral site. A coulomb repulsion *U* is included for the *e* and *t* electrons, and for simplicity we only allow the *t* electrons to hop. The hopping parameters for the *t* electrons, w_{ij}, are chosen to yield a semicircular density of states of width 1 eV centered about zero. Additionally, we choose ε_p=-1.5 eV, ε_e=1 eV, $T_{p\text{-}e}$=2 eV, and *U*=3 eV. This model contains all the necessary ingredients to qualitatively demonstrate the rehybridization mechanism. It should be clear that if all the *e* and *p* terms were removed, we would be left with a simple one-band Hubbard model for the *t* electrons.

The above model is not solvable in general, and we shall therefore employ the dynamical mean-field theory [18] (DMFT) as an approximation. Using a path integral representation of the partition function, the effective action for this model can be written in infinite dimensions as follows:

$$S_{eff} = \int_0^{\beta}\int_0^{\beta} d\tau d\tau' t^{\dagger}(\tau)G^o_t(\tau-\tau')t(\tau') + \int_0^{\beta} d\tau e^{\dagger}(\tau)G^o_e(\tau)e(\tau) +$$
$$U\int_0^{\beta} d\tau \sum_{i,\sigma}\left[e^{\dagger}_{i,\sigma}(\tau)e_{i,\sigma}(\tau)t^{\dagger}_{i,\sigma}(\tau)t_{i,\sigma}(\tau) + t^{\dagger}_{i,\uparrow}(\tau)t_{i,\uparrow}(\tau)t^{\dagger}_{i,\downarrow}(\tau)t_{i,\downarrow}(\tau) + e^{\dagger}_{i,\uparrow}(\tau)e_{i,\uparrow}(\tau)e^{\dagger}_{i,\downarrow}(\tau)e_{i,\downarrow}(\tau)\right] \quad (2)$$

where

$$G^o_e(\tau) = \left[\partial_\tau - \varepsilon_e + \mu - \frac{T^2_{p-e}}{\partial_\tau - \varepsilon_p + \mu}\right] \quad (3)$$

and G^o_t is the bath function for the *t* electrons which has to be determined self consistently using equation 4, where *D* is the quarter bandwidth.

$$G_t^o(i\omega_n) = \left[i\omega_n + \mu - D^2 G_t(i\omega_n) \right]^{-1} \quad (4)$$

The Grassman variables for the oxygen states have been integrated out. Due to the fact that we have assumed that the *e* electrons have no intersite hopping, G_e^o will remain unchanged. The above effective action corresponds to a two orbital AIM, and we are still left with a difficult many-body problem. In order to solve this, we follow the usual procedure of decoupling the quartic terms using a discreet Hubbard-Stratonavitch transformation[79], and evaluate the resulting summation using Hirsch-Fye quantum Monte-Carlo[18, 80].

First, we demonstrate how the occupation of the *t* and *e* orbitals change as the total density is varied (see Figure 39). When the *t* orbital is nearly empty, the *e* orbital has an occupation of roughly 0.45 electrons due to the strong hybridization with the oxygen. As the density increases and the *t* orbital is filled, the *e* orbital empties and the *p* orbital is filled. Thus we clearly observe the rehybridization mechanism in this simple model. It does not appear to be as strong as in LDA calculation of Na_xCoO_2, where the gain in density in the t_{2g} orbitals is largely cancelled by the loss in e_g occupation. However, this is not totally surprising given the simple nature of the model we have chosen. Most notably, we only provided one *e* orbital when there are two in the real material. This will decrease the initial occupation of the total e_g density.

In order to explore the effect of the hybridization on the low energy excitations of the system, we have performed calculations at different values of $T_{p\text{-}e}$ while maintaining a half filled *t* band (see Figure 40). The parameters chosen for this model yield a Mott insulator when the *t* orbital is half filled, as seen by the gap in the spectral function. The gap is shown to decrease as $T_{p\text{-}e}$ is increased. This demonstrates that the hybridization among the *e* and *p* orbitals results in an effective screening of the *t* electrons. This can be understood considering that increasing the hybridization will increase the occupation of the *e* orbital, resulting in an increased repulsion with the *t* electron and hence driving it to delocalize.

To conclude, we have shown that the states added to CoO_2 are not simply electrons in the t_{2g} states, but rather an electron in the t_{2g} state dressed by hole density in the e_g state and electron density in the oxygen state. This rehybridization results from a

competition between oxygen-e_g hybridization and the Co on-site coulomb interactions. The LDA result is corroborated with a modified Hubbard model which we proposed and solved using DMFT. Our DMFT calculations indicate that the presence of e_g-oxygen hybridization effectively results in a screening of the low energy t_{2g} excitations. This indicates that the oxygen states and e_g states should be considered when deriving a low energy Hamiltonian for Na_xCoO_2 and its hydrated counterpart. We note that this behavior can be seen in several other similar materials, and that this is a rather general phenomenon. Comparing the LDA bands for $Na_{1/3}CoO_2$ and $Na_{1/3}CoO_2(H_2O)_{4/3}$ shows a reduction in the band splitting due to a decrease of the interlayer coupling. This indicates that hydration does result in a more two-dimensional electronic structure, and this fact may be related to why hydration is required to create the superconducting state.

This research was supported with funding from The Department of Energy, Basic Energy Science under contract DE-F602-96ER45571 and the National Partnership for Advanced Computing (NPACI).

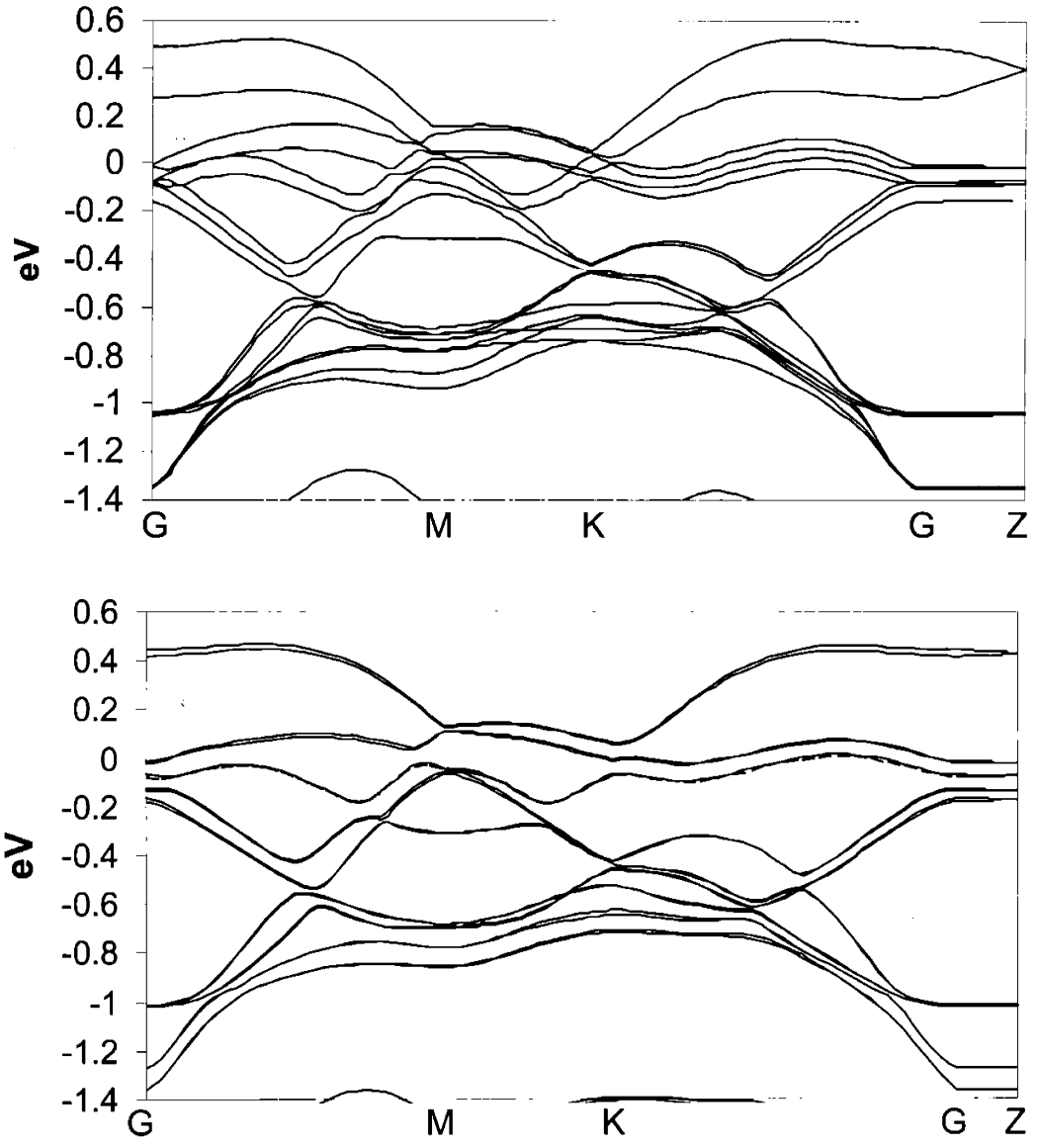

Figure 37 LDA majority t_{2g} bands for $Na_{1/3}CoO_2$ (top panel) and $Na_{1/3}CoO_2(H_2O)_{4/3}$ (bottom panel). The Fermi energy is at zero. G=(0,0,0), M=(1/2,0,0), K=(2/3,1/3,0), and Z=(0,0,1/2).

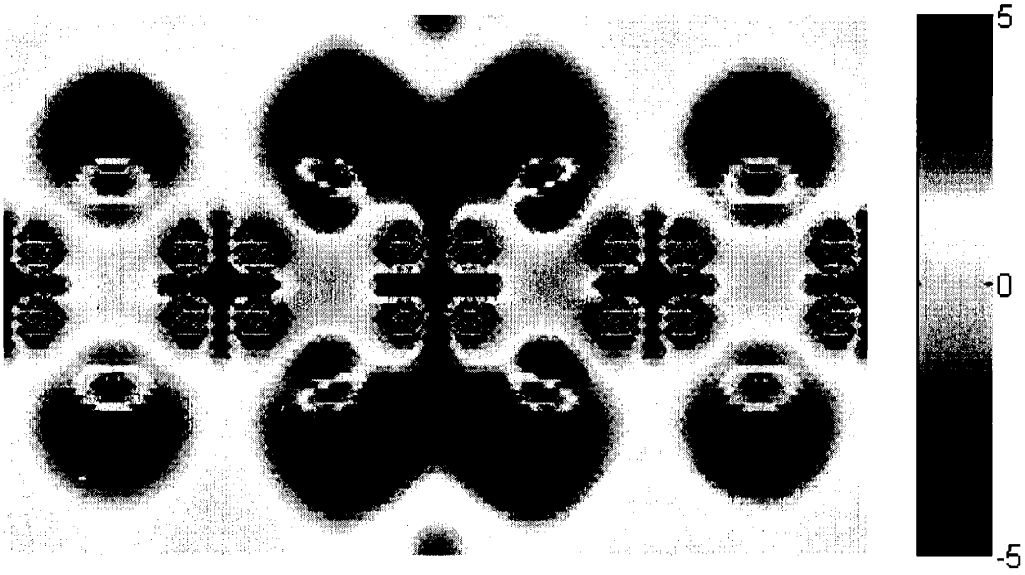

Figure 38 The total charge density difference of $Na_{1/3}CoO_2 - CoO_2$. A plane which cuts through the Co-Oxygen octahedral plane was chosen. The horizontal rows of Na/vacancies, oxygen, and Co are clearly depicted (bottom and top edge of figure bisect Na/vacancy layer). Units are electrons/$Å^3$.

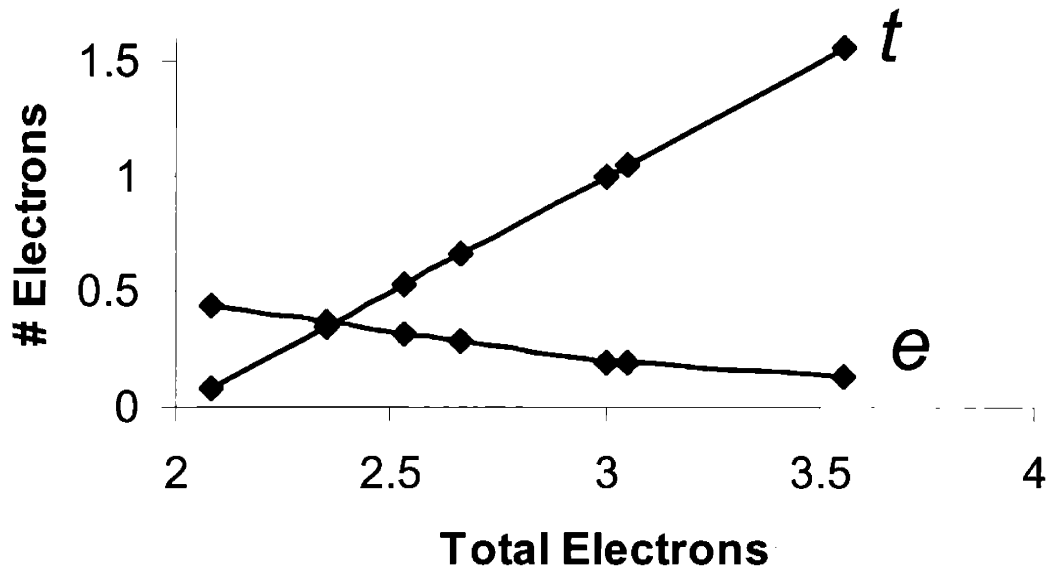

Figure 39 Total occupation of the *e* and *t* orbitals as a function of the total density.

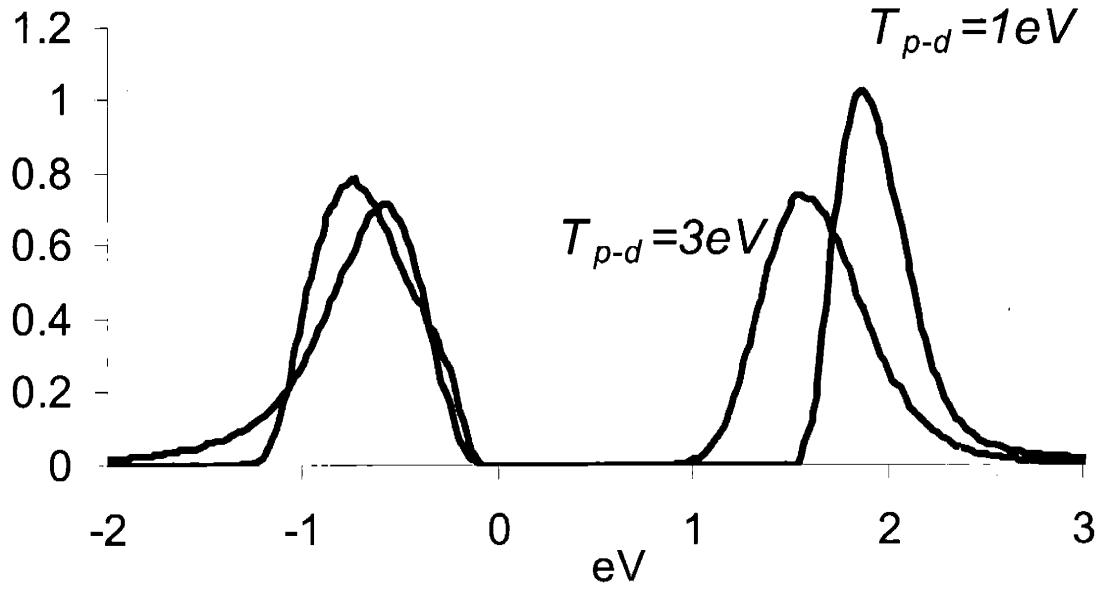

Figure 40 Spectral density for the *t* electrons $\left[\frac{-1}{\pi}\mathrm{Im}G_t(\omega)\right]$

Chapter 7

A First-Order Mott Transition in Li_xCoO_2

Abstract

Despite many years of experimental searches for a first-order Mott transition in crystalline doped semi-conductors, none have been found[81-83]. Extensive experimental work has characterized a first-order metal-insulator transition in Li_xCoO_2, the classic material for rechargeable Li batteries, with a metallic state for $x < 0.75$ and insulating for $x > 0.95$[40, 59]. Despite the fact that this transition has been well characterized experimentally, the mechanism of the transition remains unidentified. Using large-scale density functional theory (DFT) calculations, we identify this hereto anomalous metal-insulator transition as a Mott transition of impurities. DFT demonstrates that for dilute Li vacancy concentrations the vacancy binds a hole and forms impurity states yielding a Mott insulator. The details of the transition are analyzed in terms a one-band Hubbard model. We conclude that this transition is perhaps the first clear case of a first-order Mott transition in a crystalline doped semi-conductor.

Alkali doped CoO_2 is continuing to prove itself as a material rich in both fundamental physics and technological application. Na_xCoO_2 and its hydrated counterpart are receiving renewed interest due to the discovery of superconductivity[42], in addition to anomalous thermoelectric properties[63]. Li_xCoO_2 is the primary cathode material in rechargeable Li batteries, sustaining a multibillion dollar market. As a result, it has been the subject of intense experimental and theoretical study, including the prediction[35, 38, 39] and experimental verification[84, 85] of unusually complex phase behavior. In this paper we use large-scale density functional theory (DFT) calculations to demonstrate that this technologically important material also exhibits the first clear example of a first-order Mott transition in a doped semi-conductor.

Li_xCoO_2 crystallizes in a layered structure, which can be thought of as an interpenetrating face-centered-cubic lattice with one sublattice containing oxygen and the other containing alternating (111) planes of Li and Co. When Li_xCoO_2 is fully lithiated, x = 1, Co is formally in the 3+ valence state. Due to the appreciable crystal field, the Co-3d states are split into a lower manifold containing three levels (t_{2g} states) and a higher manifold containing two states (e_g levels). Having six *d* electrons, Co exists in the low spin $t_{2g}^6 e_g^0$ configuration and $LiCoO_2$ is a band insulator. Because of the high mobility of Li in this material, it is possible to remove Li either by chemical[86] or electrochemical means[87]. This ability to exchange Li gives Li_xCoO_2 its excellent properties as a Li storage material in rechargeable Li batteries[87, 88]. Li removal creates a variety of phase transitions in the material including order/disorder transitions[38, 87], oxygen sliding[89], and alkali staging[38, 84]. Our focus in this paper is on the phase transition in the early stage of delithiation, which is believed to be a metal-insulator transition[40]. Using DFT calculations we provide evidence that this transition is a Mott transition of impurity states. Although Mott predicted such transitions to be first-order, all known examples in doped semi-conductors are continunous due to the random placement of the impurities.

The electronic changes that occur in LixCoO2 as Li is removed are related to its structural changes. Electronically, Li removal leads to the creation of holes in the valence band of Li_xCoO_2 which is of t_{2g} character. Conductivity measurements indicate that there is a composition-dependent activation barrier for $x > 0.95$ which increases as x approaches one, ranging from a minimum of less than 10 meV to a maximum of 100-300

meV[40, 57] X-ray diffraction studies of Li_xCoO_2 indicate that Li removal does not occur continuously, but through two-phase coexistence for $0.75 < x < 0.95$[40]. The two coexisting phases are very similar, with the same symmetry but a 0.7 % difference in the *c* lattice parameter, and no appreciable difference in the *a* lattice parameter (hexagonal setting)[59]. Li-NMR indicates there is a unique NMR signal for each phase, indicating an electronically different Li environment in both phases[40]. The signal for the phase with low Li composition ($x = 0.75$) is Knight-shifted indicating metallic behavior, while Li has no NMR shift in the phase with high Li content, indicating localized carriers. Based on these experiments it has been concluded[40] that for $x > 0.95$ the system contains weakly bound carriers and for $x < 0.75$ the system is metallic and that the two-phase coexistence of phases with the same symmetry for $0.95 < x < 0.75$ is likely the result of a first-order metal insulator transition. In this paper, we show that the mechanism of this transition is a classical Mott transition, with an insulating impurity band at high lithium composition decomposing into the valence band as the concentration of lithium vacancies increases.

The first step in understanding the transition is identifying what specific mechanism is inducing the insulating state for high Li concentrations. $LiCoO_2$ is band insulator with the Fermi level between the filled t_{2g} states and the unfilled e_g states and one could naively expect a metallic state for $x < 1$. Given that the insulating state only has a dilute concentration of holes (< 5%) the on-site Co t_{2g} interactions are not directly relevant as the double occupation of holes on the same site is unlikely. The possible physical phenomena which may be responsible for the localization of the hole are polarons and the electrostatic potential of the Li vacancy. As will be shown below, density-functional theory (DFT) calculations indicate that the vacancy potential is a dominant factor in localizing the holes.

All DFT calculations were performed using the *Vienna Ab-initio Simulation Package* (VASP)[70, 71] within the local-density approximation (LDA). VASP solves the Kohn-Sham equations using projector augmented wave pseudopotentials[72, 73] and a plane wave basis set with a cut-off energy of 400 *eV*. In the present calculations, we are investigating the nature of the insulating phase, $x > 0.95$, and therefore large supercells are required to attain dilute concentration of vacancies. Large-scale parallel computation was performed on the Blue Horizon supercomputer to reach a minimum concentration of

0.78% vacancies, corresponding to a cell with 512 atoms. The effect of the impurity potential can be seen by inspecting the top edge of the valence density-of-states (DOS). If the vacancy potential is strong enough, it will bind the hole resulting in an impurity band which breaks away from the top of the valence band. This is analogous to what occurs in the classic doped semiconductors, such as Si:P[90], and Figure 41 schematically illustrates possible scenarios for this impurity band. For $LiCoO_2$, the valence band is full (Figure 41A). When the system is lightly doped, an impurity band may form resulting in a small peak separated from the top of the valence band, and this peak would be half-filled given that there is one hole associated with each vacancy (Figure 41B). If an impurity band forms, it is possible that the on-site correlations within the impurity band will be strong enough to split the impurity band and form a Mott insulator (see Figure 41C and Figure 41D). Some of the previously described behavior is observed in the LDA calculations. Inspecting the top edge of the LDA non-spin-polarized valence DOS, the formation of a peak can clearly be observed as Li is removed (see Figure 42). The peak grows more distinct as the vacancy concentration is decreased, culminating in an impurity band for 0.78% vacancies which is barely split off from the valence DOS. Therefore, LDA calculations indicate the formation of an impurity band, similar to what is pictured in Figure 41B. The non-spin-polarized LDA calculations will always give a metallic impurity band, Figure 41B, as opposed to a Mott insulating impurity band, Figure 41C or Figure 41D, given that LDA does not properly treat the electronic correlations. However, allowing for spin polarization (LSDA) in the 1.4% vacancy calculation demonstrates that the ferromagnetic interactions split the impurity band and produce a ferromagnetic insulator (similar to Figure 41D), which is as close as LDA can come to the true insulating state. The key result is that the LDA produces an impurity band. This band would likely be split in the dilute limit considering that the impurity bandwidth at 0.78% is roughly 20 meV, while the experimental conductivity demonstrates that the binding energy of the hole is an order of magnitude larger.

In order to better characterize the nature of the impurity state, we can plot the hole density which has been added to the system as Li is removed. This can be done by subtracting the charge density of the structure with Li vacancies from that of stoichiometric $LiCoO_2$, while holding all structural parameters constant. Figure 43 shows

the result for $Li_{0.969}CoO_2$ (3.1% vacancies). The impurity state which is formed by the vacancy potential can be seen as hole density which congregates around the vacancy, and it displays a rather complex structure. The most notable feature is the dominant hole character on the oxygen *p* orbitals which surround the vacancy. Additionally, electron density can be identified within the e_g orbitals and hole density within the t_{2g} orbitals on all the Co atoms which surround the Li vacancy. Given that the projection of the DOS indicates a predominant Co character within the impurity band (see Figure 42A green curve), it is not immediately obvious why such a strong oxygen character is observed in the charge density difference plot. This phenomenon has been previously observed in $LiCoO_2$[38, 78, 91] and studied in greater detail in Na_xCoO_2 [92]. It is referred to as a rehybridization mechanism, and it results from a competition between the e_g-oxygen hybridization and the on-site Co Coulomb interaction.

The above LDA calculations indicate that the *insulating* state is a Mott insulator of impurity states, and therefore it is useful to represent the low energy physics of the insulating phase as an effective half-filled Hubbard model of impurity states. As the vacancy concentration within the insulating phase is varied, the effective Hubbard model remains half-filled but two distinct effects will modify the electronic structure. First, the center of gravity of the impurity band will move towards the t_{2g} bands as the vacancy concentration increases. This is due to the fact that the larger hole density will more effectively screen the vacancy potential. Secondly, the hopping parameters among the vacancy sites (ie. the impurity bandwidth) will increase as the increasing vacancy concentration decreases the average inter-vacancy distance. This will reduce the splitting between the upper and lower Hubbard impurity band. Both effects can independently cause a transition to the metallic state though in a qualitatively different manner. In the first case, the screening of the vacancy potential causes the impurity band to decompose and its states to merge with the t_{2g} bands once a sufficient hole density is achieved. We refer to this as a classic Mott transition. In the second case, the intra-impurity band hopping parameters will increase as a function of doping and will eventually overcome the impurity on-site coulomb interaction, giving a metallic impurity band as in Figure 41A. Given that this is a metal-insulator transition within an always half-filled band we refer to it as a Mott-Hubbard transition. Clearly, a necessary requirement for the Mott-

Hubbard transition is that the impurity band persists and is not first destroyed by the classic Mott mechanism. The composition dependence of the activation energy in the conductivity of Li_xCoO_2 can be qualitatively understood in terms of the above mechanisms. The excitation gap for carriers will either be between the upper and lower Hubbard impurity band, or between the lower Hubbard band and the t_{2g} states if the upper Hubbard band lies within the t_{2g} states (see Figure 41 C and D). In the first scenario the increase in the intra-impurity hopping parameters will decrease the gap, while in the second case both the increase in the intra-impurity hopping and the screening of the impurity potential will reduce the gap.

Having established the nature of the insulating state and the different mechanisms by which it may be destabilized, we now address the first-order transition to the metallic state. If the metal-insulator transition in Li_xCoO_2 is a Mott-Hubbard transition, it could be modeled with a one-band Hubbard model. The one-band Hubbard model has been extensively studied within the dynamical mean-field theory (DMFT), and a first-order Mott transition is indeed observed as the relative magnitude of the hopping and the on-site interaction is varied[18]. However, this one-band assumption does not appear to be valid in this material. The two-phase region spans 5-25% vacancies, and therefore once more than 5% vacancies are present, a new metallic phase with 25% vacancies will nucleate and grow at the expense of the insulating phase as the vacancy content is further increased. It is therefore unlikely that the impurity band exists in the metallic phase given that the metallic phase forms at 25% vacancies, and this is supported by our calculations. Alternatively, the metallic phase can be well described with t_{2g} states at the Fermi level, in which the impurity band has decomposed and the role of the vacancy has been reduced due to screening. Therefore, the transition in Li_xCoO_2 appears to be best characterized as a classic Mott transition, in the sense that the transition is associated with a decomposition of the impurity band due to screening of the vacancy potential by the long range coulomb interaction of the hole density. Now that the qualitative nature of this transition is understood, we investigate whether or not LDA shows any sign of predicting a first-order transition by looking for a non-convexity in the energy as a function of vacancy content. The LDA should do reasonably well in describing the energetics of metallic phase, while it likely does not properly describe energetics of the Mott insulating

state. We plot the formation energy for the cases of 3.1% and 5.6% vacancies along with the previously published formation energies (see Figure 45). As shown, the formation energy is nearly linear in the dilute limit and there is no sign of a non-convexity. Therefore, although LDA produces an insulating state for low vacancy concentrations, it fails in capturing the first-order nature of the MIT. Most likely this failure occurs because LDA does not correctly describe the energetics of the Mott insulating phase correctly. In terms of the effective Hubbard model of the impurity band, one might suggest that LDA is similar to a Hartree-Fock solution of this Hubbard model whereas the true solution would give a correlation induced splitting which would be lower in energy. Therefore the LDA energies should be pulled down for $x > 0.95$ and this could create the non-convexity and hence the two phase region. Another possible source of error in the insulating phase is the possibility that the LDA does not properly describe the formation of the impurity band due to the well known fact that LDA does not properly localize charge. Additionally, a polaron would assist in forming the impurity band by enhancing the effective mass of the holes. Although, there is no a-priori reason to expect the electron-phonon coupling to be large in this situation, given that the symmetry of the t_{2g} states is already broken. All of the above factors will help stabilize the insulating phase and therefore help create the non-convexity.

Now that the qualitative nature of this transition is understood and it is clear that LDA fails, it is evident that capturing this transition within a first-principles approach will be challenging. This is due to the fact that the low energy electronic degrees of freedom exist on a different length scale for the metal and the insulator. The insulating state is characterized in terms of coarse impurity states which span many oxygen and Co ions, while the metallic phase is characterized in terms of finer Co t_{2g} states. In order to capture the transition, it would be necessary to write the Hamiltonian on the smaller length scale (ie. in terms of the Co t_{2g} states). Clearly, one would need to include the impurity potential, perhaps in some average manner, in addition to the on-site and long range coulomb interaction. Additionally, it is possible that the oxygen states may need to be treated explicitly considering that the rehybridization mechanism plays a clear role in forming the impurity state, as demonstrated above. Quantitatively describing this

transition will serve as a great challenge to new theoretical techniques, such as cluster DMFT[93, 94], GW+DMFT[95, 96], and typical-medium theory[97].

One of Mott's early suggestions was to search for the Mott transition in the classic doped semiconductors[98]. Despite the extensive amount of experiments which have been performed on crystalline doped semiconductors, all of the observed metal-insulator transitions are continuous transitions as opposed to first order[81, 82]. This is typically attributed to the random distribution of the impurity states, which creates Anderson localization and destroys the first-order nature of the transition[81]. Perhaps the only exceptions occur in solutions such as Na-NH_3 where there are experimentally observed first-order transitions which are believed to be associated with a Mott transition[83]. Mott suggested that the high mobility in these solutions may allow the impurities to form a higher degree of order relative to the low mobility crsytalline materials such as Si:P, and perhaps this suppresses the Anderson transition and gives a first-order Mott transition[83]. Therefore, the high mobility of the Li-vacancy may be a key difference relative to Si:P which allows the transition to be first-order. Thus it appears that a very commonly used material such as Li_xCoO_2 may be the long awaited example of a first order Mott transition in a crystalline doped semi-conductor.

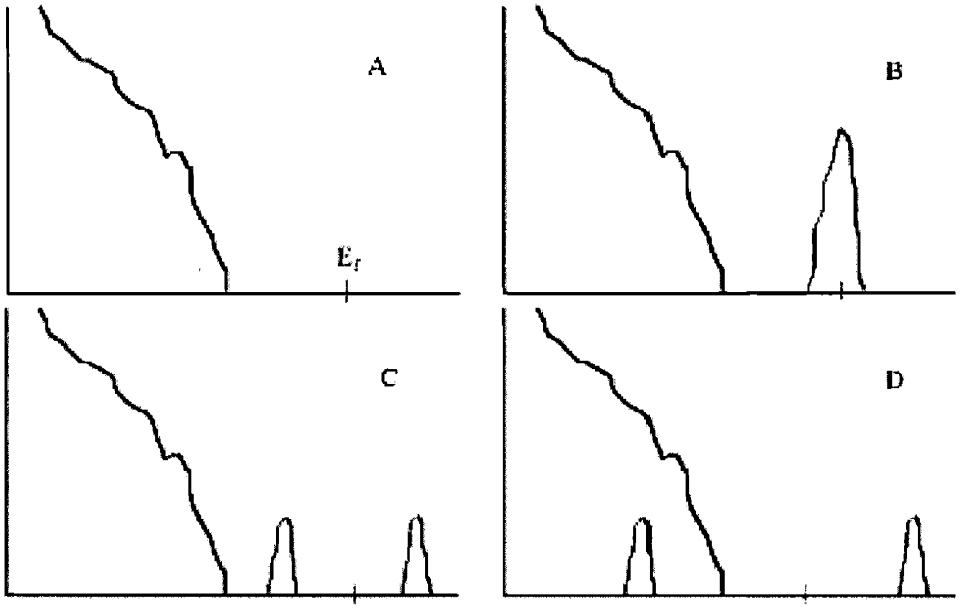

Figure 41 A schematic of the density-of-states for various realizations of the impurity band. The blue curve is the valence band and the red curve is the impurity band. A.) Pure band insulator. B.) Lightly doped band insulator with a metallic impurity band. C.) Lightly doped band insulator with a Mott insulating impurity band in which the gap is between the Lower and upper Hubbard impurity band. D.) Same as C except one of the Hubbard bands has split into the valence band.

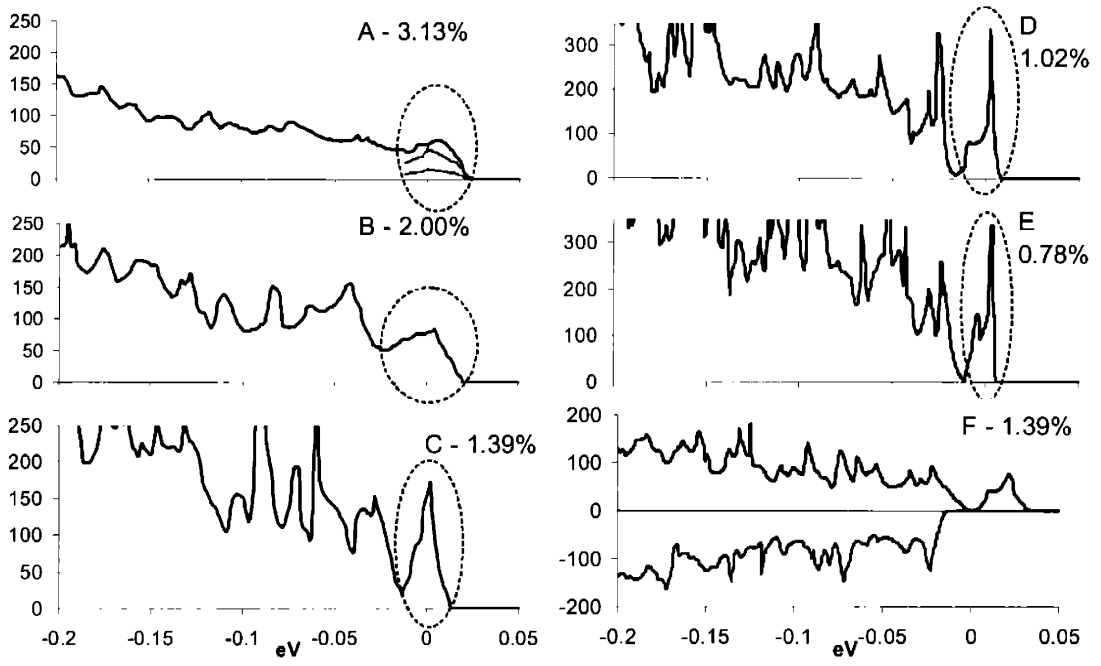

Figure 42 LDA DOS for various supercells. The impurity band is circled for clarity. All plots are non-spin-polarized with the exception of panel F. A.) 4x4x2 unit cell, 3.13% vacancies. Oxygen and Co partial DOS for the impurity band is shown in red and green, respectively. B.) 5x5x2 unit cell, 2.00% vacancies. C.) 6x6x2 unit cell, 1.39% vacancies. D.) 7x7x2 unit cell, 1.02% vacancies. E.) 8x8x2 unit cell, 0.78% vacancies. F.) 6x6x2 unit cell, 1.4% vacancies.

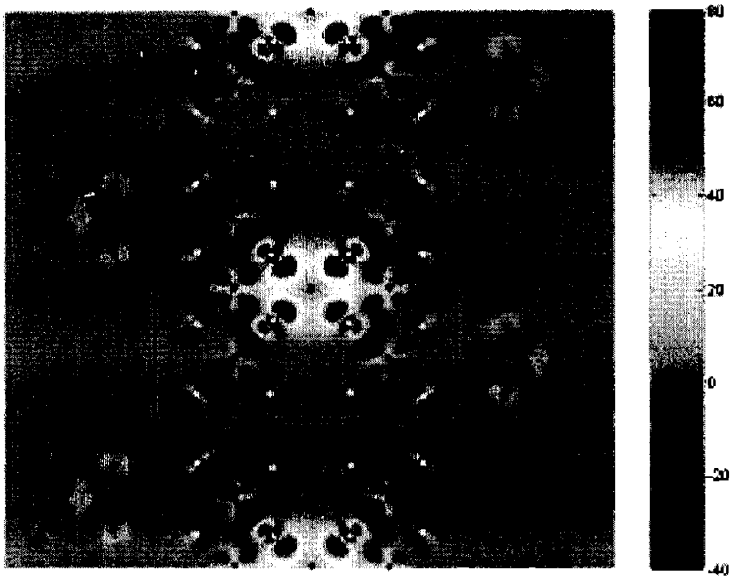

Figure 43 The total charge density difference of $Li_{0.969}CoO_2 - CoO_2$. A plane which cuts through the Co-Oxygen octahedral plane was chosen. The vacancy is depicted by a black dot, while selected Co and oxygen atoms are designated by red and white dots, respectively. The vertical rows of Li/vacancies, oxygen, and Co can be seen. Units are electrons/$Å^3$.

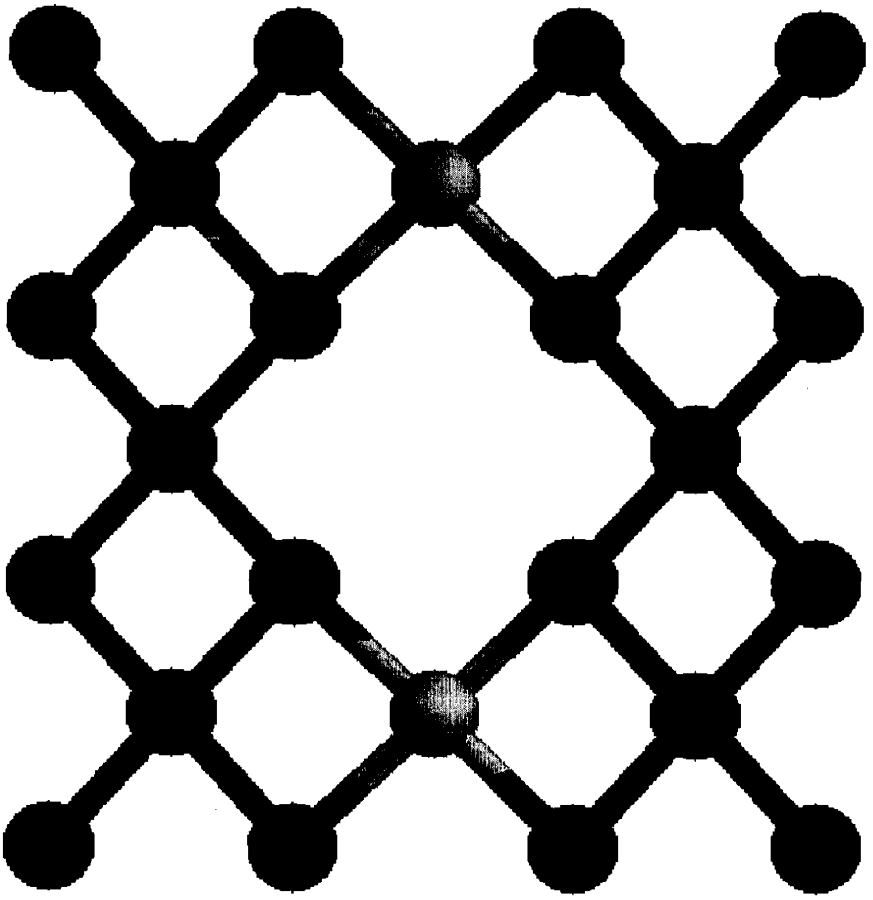

Figure 44 A schematic of the Li (yellow), Co (blue), and oxygen (red) atoms which lie within the black rectangle in the plane pictured in Figure 43. The Li vacancy is located in the center.

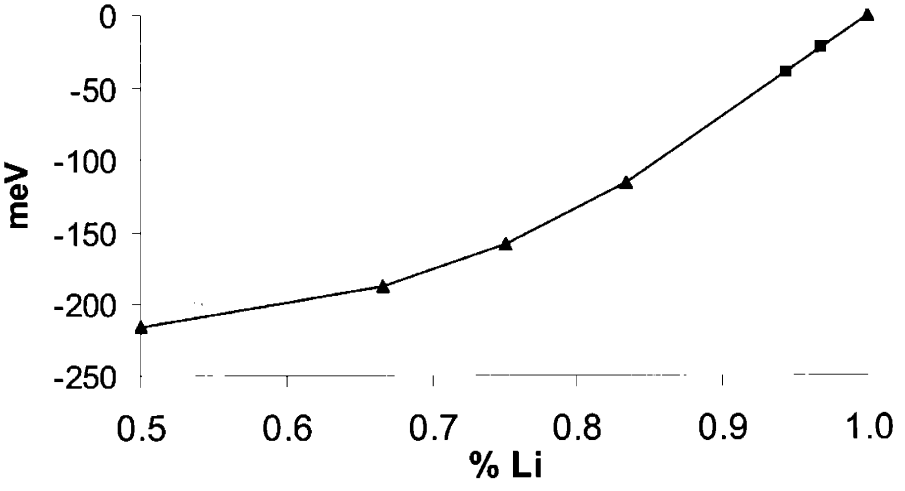

Figure 45 Total energy of Li_xCoO_2. Previously published calculations by Van der Ven et al[38] are given by blue triangles, while our calculations are given by red squares.

Chapter 8

Predicting High Energy Photoemission Satellites Using LDA+DMFT

Abstract

$LiCoO_2$ is known to display a high energy photoemission satellite which is not captured within the LDA. We show that LDA+U also fails to predict the satellite, while LDA+DMFT solved within multi-band iterated perturbation theory (IPT) successfully recovers the satellite. The satellite is shown to be of t_{2g} character, and results from a combination of on-site Co coulomb repulsion and hybridization among the oxygen and *d* states.

Understanding the photoemission spectra of transition-metal oxides has been an active area of research over the past 40 years and continues to this day. Typically, experimental measurements are compared to density functional theory (DFT) calculations and empirical configuration interaction cluster calculations (CICC)[99]. Both techniques have there advantages and disadvantages. As is well known, DFT does not rigorously predict the eigenvalues of the N-1 particle system, which are measured in a photoemission experiment, even if the exact density functional were used. However, experience has shown that DFT within the local density approximation (LDA) is usually qualitative and systematic when the electronic correlations are not too strong. In the case of strong correlation, LDA fails to predict features within the spectra that arise from correlation effects, such as a Mott-Hubbard gap. Regardless, LDA is very useful in that it is a first-principles method and it usually lends insight even when the correlation is strong. CICC is an empirical technique which involves constructing a model Hamiltonian for the transition metal and the nearest oxygen shell. The model Hamiltonian usually includes the on-site coulomb repulsions between the *d* electrons in addition to hybridization among the *d* and *p* electrons. The Hamiltonian is then diagonalized within some truncated many-particle basis set. Some of the model parameters are usually fit to the experimental results, while others are estimated or roughly calculated. The main advantage of this technique is that can capture strong correlation effects, and it rigorously gives eigenvalues of the N-1 particle system. The main disadvantage is that it is not a first-principles technique. Additionally, the periodicity of the solid has been removed which is usually not detrimental to the high energy physics, but can be detrimental on lower energy scales.

Ideally, one would have a technique which shares the advantages and lacks the disadvantages of the above techniques, and this is largely achieved within the LDA+DMFT (dynamical mean-field theory) method[21-23]. DMFT is a powerful approximation used to solve models of strongly correlated electrons[18]. DMFT effectively maps the many-body lattice problem onto a *single-site* many-body problem which hybridizes with an effective bath function that emulates the lattice. Specifically, the Hubbard model is mapped onto an Anderson impurity model subject to a self-consistency condition, and thus a complicated many-body problem is replaced by simpler one at the

expense of neglecting the *k*-dependence of the self-energy. Given that the CICC is a single site approach which simply ignores the rest of the lattice, DMFT can be viewed as a direct extension of the CICC. DMFT by itself is solely a method to solve the many-body problem, and it must be merged with the LDA in order to determine the parameters which are fit or guessed in the CICC.

One begins by defining the orbitals to which the correlations will be explicitly applied, such as the *d* or *f* atomic-like orbitals. In our calculations, we use a linear muffin-tin orbital (LMTO) basis[100], and we define the *d* states within the muffin-tin as the correlated state. The main idea of LDA+DMFT is to replace the Kohn-Sham potential within the correlated subspace with an accurate approximation for the self-energy of the *d* states in order to recover correlation effects and the true excitation spectra. Explicitly, the following Dyson-Kohn-Sham equation is solved.

$$\left[H_{KS} + \sum_{\alpha,\beta,R} \left| d_{\alpha,R} \right\rangle \left(\Sigma_{\alpha,\beta}(i\omega) - \Sigma_{dc} \right) \left\langle d_{\beta,R} \right| \right] \psi_{k,\omega} = \varepsilon_{k,\omega} \psi_{k,\omega} \tag{95}$$

where the first term is simply the Kohn-Sham Hamiltonian and the second term is the self-energy operator for the correlated *d* states. The indices α and β run over the ten spin orbitals for the *d* states, while *R* runs over all the sites in the lattice. $\Sigma_{\alpha\beta}(i\omega)$ is the frequency dependent self-energy for the *d* electrons calculated within DMFT on the imaginary axis, and Σ_{dc} is the "double counting" correction to the self-energy. The double counting self-energy is a static contribution which is supposed to be accounted for within the LDA. No exact expression is known for this quantity and we use the conventional expression $\Sigma_{dc} = \delta_{\alpha\beta}\left(N_d - \frac{1}{2}\right)$, where N_d is the total number of electrons in the *d* shell[23]. $\varepsilon_{k,\omega}$ and $\psi_{k,\omega}$ are the frequency dependent eigenvalues and quasiparticle wavefunctions, respectively. This equation must be solved at every *k*-point for a grid of imaginary frequencies. The self-energy is not known a priori, and DMFT is used to calculate it.

We begin by guessing the self energy, and solving the Dyson-Kohn-Sham equation. Then, the local *d* Greens functions are computed with the following relation.

$$G_{\alpha\beta}(i\omega_n) = \sum_k \frac{\psi^*_{k\alpha\omega}\psi_{k\beta\omega}}{i\omega_n - \varepsilon_{k\omega}} \tag{96}$$

Dysons equation is then used to construct the free local Greens function, also known as the bath function, which is identically the unperturbed Greens function of the effective Anderson impurity model.

$$\hat{G}_o^{-1}(i\omega_n) = \hat{G}^{-1}(i\omega_n) + \hat{\Sigma}(i\omega_n) \tag{97}$$

where the Greens functions and self-energy have been written as *10x10* matrices. Now the resulting AIM must be solved in order to construct a new self-energy, and a variety of techniques may be used. In this study we use both Hartree-Fock and multiband iterated perturbation theory (IPT)[18] on the imaginary axis to solve the impurity problem. It should be noted that solving LDA+DMFT within Hartree-Fock is equivalent to performing LDA+U. The IPT corresponds to the second order perturbation theory, with the important difference that the *Hartree-Fock* Greens function is used in place of the free propagators. This is motivated by the fact this approach reproduces *both* the weak-coupling and the strong-coupling solution for a half-filled, particle-hole symmetric model. While this property does not directly apply to the situation at hand, IPT is still a higher order correction which goes beyond Hartree-Fock and introduces frequency dependence to the self-energy. The self-energy within IPT is written in terms of the Hartree-Fock Greens function as follows:

$$\Sigma_\alpha^{IPT}(i\omega_n) = \Sigma_\alpha^{HF} + U^2 \int_0^\beta \left(e^{i\omega_n \tau} \tilde{G}_{o,\alpha}(\tau) \sum_{\beta\neq\alpha} \tilde{G}_{o,\beta}(\tau) \tilde{G}_{o,\beta}(\beta-\tau) \right) d\tau \tag{98}$$

where

$$\tilde{G}_{o,\alpha}(i\omega_n) = \left(G_{o,\alpha}^{-1}(i\omega_n) - \Sigma_\alpha^{HF}(i\omega_n) \right)^{-1} \tag{99}$$

and

$$\Sigma_\alpha^{HF} = U \sum_{\beta\neq\alpha} n_\beta \tag{100}$$

The new self-energy is then put back into the Dyson-Kohn-Sham equation and the procedure is iterated to self-consistency. We should note that in principle one should iterate both the density and the Greens function to self consistency. This can be achieved by simply updating the density every few iterations. However, if the changes in the *d*

density matrix are small, updating the density will only be a small effect. Most LDA+DMFT calculations to date have neglected this, and we also assume a static density.

$LiCoO_2$ is a low spin, band insulator with filled t_{2g} states due to the appreciable crystal field splitting induced by the octahedral oxygen environment. The strong hybridization between the e_g states and the oxygen states moves electron density into the e_g orbital and hole density into the oxygen states in the ground state. Both the photoemission and inverse photoemission spectra for $LiCoO_2$ have been measured in numerous studies[47, 51]. The spectrum has been compared to LDA calculations[48], and a CICC calculation has been fit to the experimental spectrum[47]. The removal spectrum consists of the main line, the oxygen *2p* states, the satellite, and the oxygen *2s* states (see Figure 46). The LDA spectrum successfully reproduces the main line and the oxygen *2s* states, but the oxygen *2s* states and the band gap are under-predicted. Under-predicting the band gap is a usual LDA error and is anticipated. However, the satellite is totally absent, suggesting that perhaps correlations are important in producing it. The CICC was able to reproduce the photoemission spectrum with reasonable parameters[47]. The occupation of the ground state is found to be roughly $0.47\left|t_{2g}^6\right\rangle + 0.44\left|t_{2g}^6 e_g^1 L_{e_g}^1\right\rangle + 0.09\left|t_{2g}^6 e_g^2 L_{e_g}^2\right\rangle$, where L designates a hole in the oxygen states. The state $\left|t_{2g}^6 e_g^1 L_{e_g}^1\right\rangle$ is higher in energy than $\left|t_{2g}^6\right\rangle$ due to the increased *d* coulomb repulsion and the energy difference among the *d* and *p* electrons, but the configurations mix strongly due to the strong hybridization between the e_g and oxygen states. This is in qualitative agreement to what is found using LDA. The occupation of the main line is found roughly to be $0.17\left|t_{2g}^5\right\rangle + 0.5\left|t_{2g}^5 e_g^1 L_{e_g}^1\right\rangle + 0.3\left|t_{2g}^5 e_g^2 L_{e_g}^2\right\rangle$, while the composition of the satellite is only qualitatively described as predominantly $\left|t_{2g}^5\right\rangle$. Given that the energy difference between $\left|t_{2g}^5\right\rangle$ and $\left|t_{2g}^5 e_g^1 L_{e_g}^1\right\rangle$ is within a few eV, the authors point out that hybridization plays a large role in the splitting of the states.

LDA+DMFT calculations as described above were performed using both Hartree-Fock (ie. LDA+U) and IPT solutions for the impurity model at a temperature of 70 meV. The spectral function for the t_{2g} and e_g states are shown for each case (see Figure 47 and

Figure 48). The $U = 0$ calculation is very similar to the LDA calculation in Figure 46, as it should be, displaying a gap of roughly 0.9 eV, and mixing between the oxygen states and both the t_{2g} and e_g states. It should be clear that there is no sign of the satellite in the LDA spectrum, and the closest features are the spectral density for both the t_{2g} and e_g states which results from hybridization with the oxygen.

The LDA+U results are straightforward to interpret, as $\Sigma_\alpha - \Sigma_{dc} = U\left(\frac{1}{2} - n_\alpha\right)$ for the case of a diagonal density matrix, where n is the occupation of a given spin orbital. Therefore, the potential which is added to the Kohn-Sham equation simply shift states which project out α character down by $\frac{U}{2}$ if α is occupied and upward by $\frac{U}{2}$ if α is unoccupied. The e_g orbitals have an occupancy of roughly 0.35 within LDA while the t_{2g} orbitals are essentially full so the e_g states will weakly shift upward and the t_{2g} states will shift downward by roughly $\frac{U}{2}$. As U is increased, the splitting among the t_{2g} and e_g states clearly increases, and thus the band gap is pushed closer to the experimental value of 2.7 eV [47]. Additionally, the t_{2g} spectral density of the main line can be seen merging into the t_{2g} spectral density which resulted from hybridization with the oxygen. However, there is no sign of the satellite in these results.

The band gap is decreased for the LDA+DMFT solution as compared to the LDA+U solution for all U. This can be understood by examining the self-energy for the IPT solution (see Figure 49). The frequency dependence of the t_{2g} self-energy tends towards higher energies at low frequencies, while the opposite effect is observed for the e_g electrons. This effectively reduces the difference between the t_{2g} and e_g self-energy and thus screens the gap. Therefore, we anticipate a smaller band gap for IPT as compared to the HF solution.

The LDA+DMFT calculations do produce the satellite. As U is increased, the splitting between the t_{2g} spectral density of the main line and the t_{2g} spectral density which was initially mixed with the oxygen increases and creates the satellite. Thus the satellite is composed of Co t_{2g} character. When we start with $U = 0$, there are no correlations and as a result the only presence of the satellite is due to hybridization. As U increases, the splitting among the configurations will increase which is what we observe in our DMFT calculations. These results compliment the CICC as the importance of

hybridization can clearly be seen. However, it should be noted that the satellite is not captured by the Hartree-Fock solution within LDA+DMFT and therefore the correlations or equivalently the frequency dependence of the self-energy is important in creating the satellite.

In conclusion, we show that LDA+DMFT solved within IPT are able to predict the high energy satellite in $LiCoO_2$ which is not predicted by LDA and LDA+U calculations. Using $U = 5$eV, LDA+DMFT(IPT) produces the satellite, while improving the band gap to 1.7 eV.

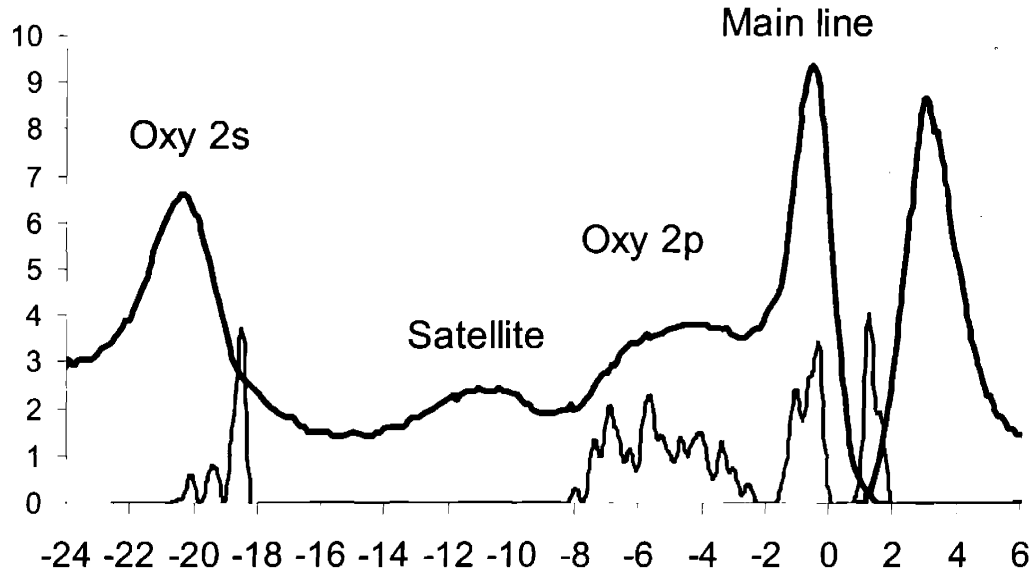

Figure 46 Photoemission / Inverse Photoemission as measured in experiment[47] (blue) and the LDA DOS (red).

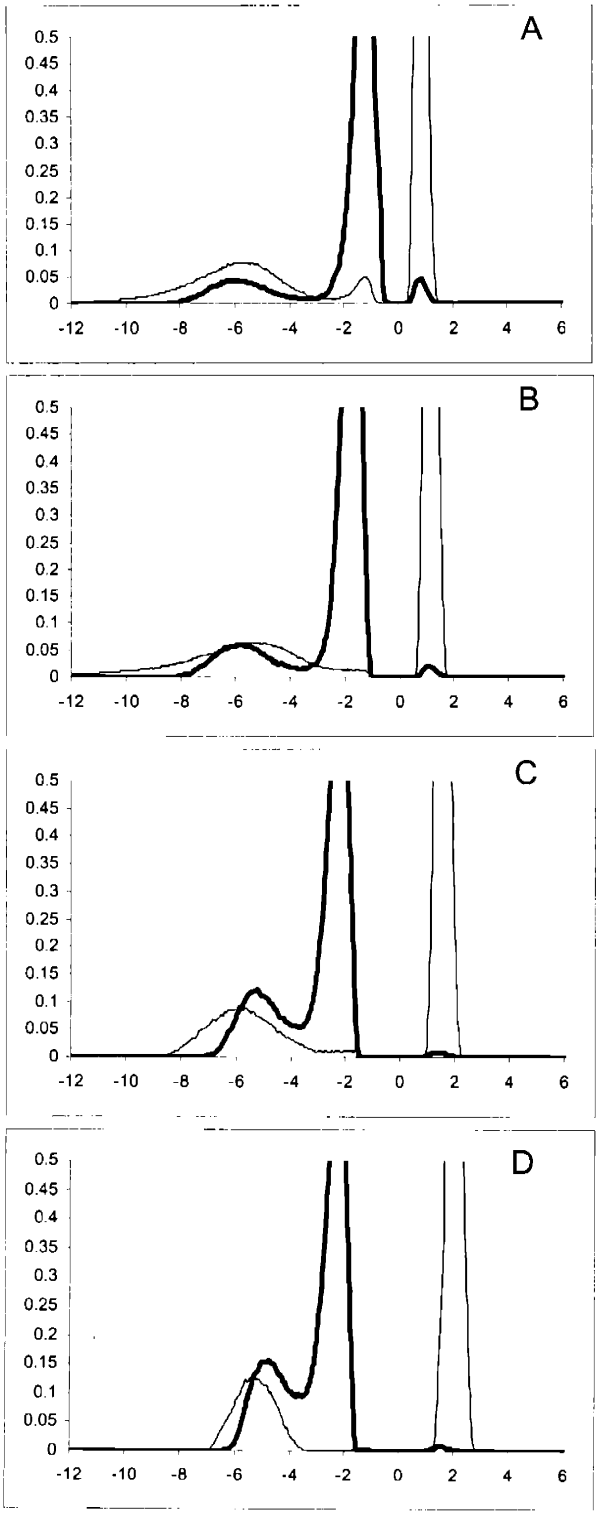

Figure 47 Spectral function for the e_g (red) and t_{2g} (blue) electrons calculated within LDA+U for A.) U = 0. B.) U = 2 eV. C.) U = 4 eV. D.) U = 5 eV.

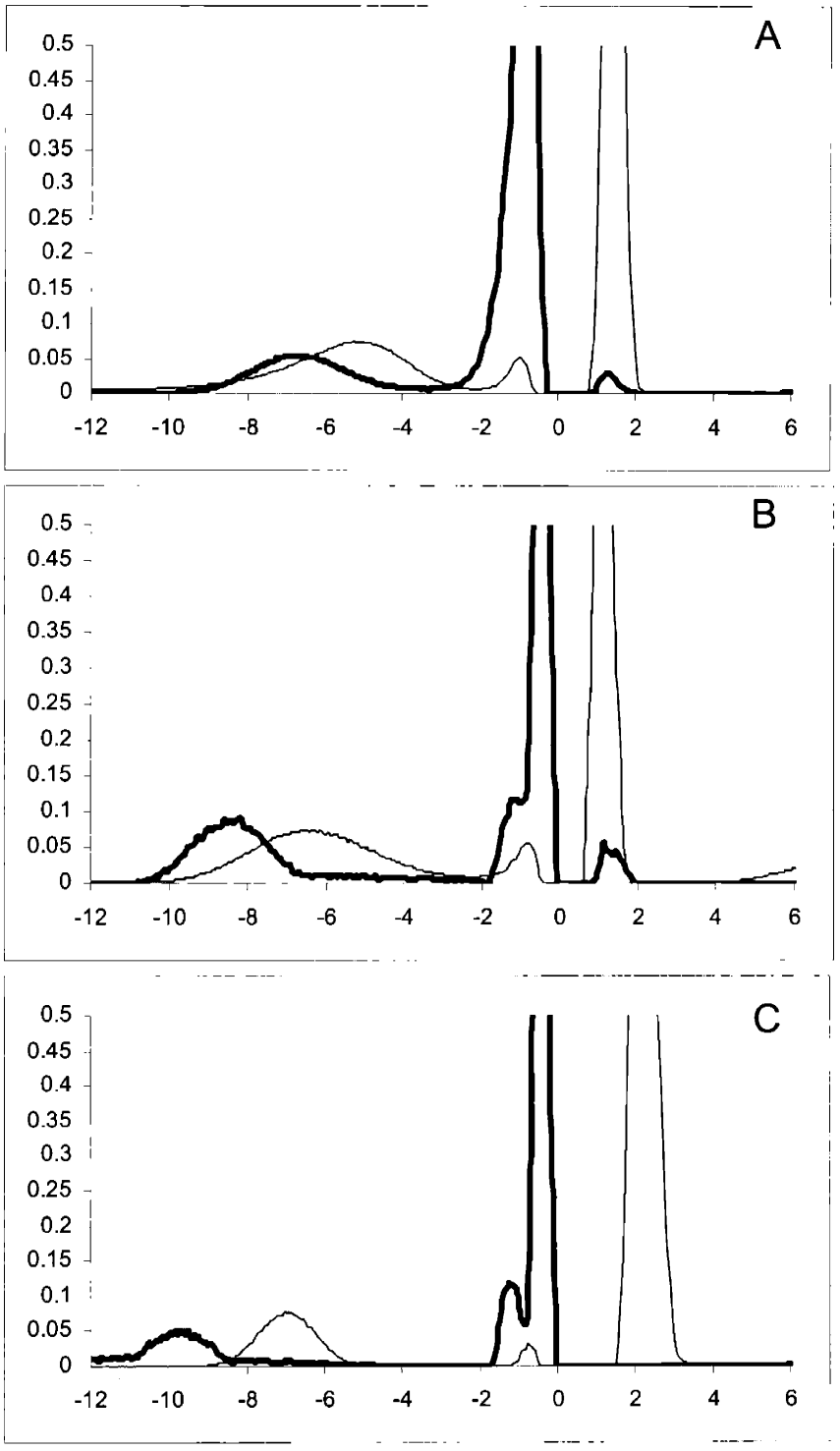

Figure 48 Spectral function for the e_g (red) and t_{2g} (blue) electrons calculated within LDA+DMFT for A.) U = 2 eV. B.) U = 4 eV. C.) U = 5 eV.

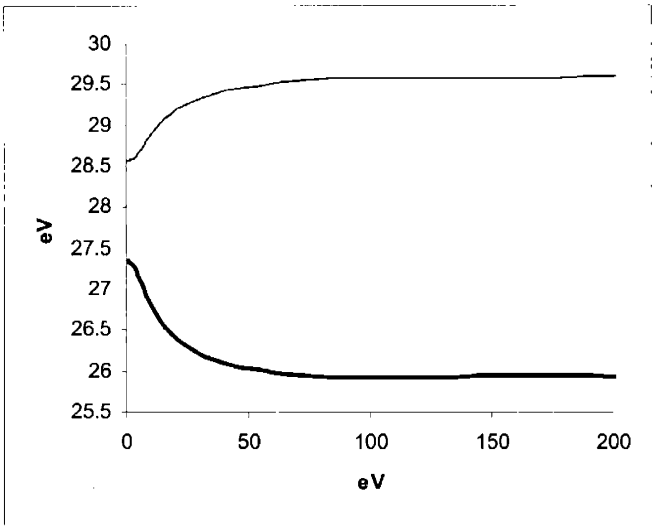

Figure 49 Real part of the self-energy as a function of imaginary frequency for both the t_{2g} (blue) and e_g (red) orbitals (U = 5 eV).

Chapter 9

Conclusions

In this thesis, the dynamical mean-field theory and the LDA are used to further the understanding of the electronic properties of Li_xCoO_2. The first problem addressed is the rehybridization mechanism within Li_xCoO_2. LDA calculations demonstrate that when holes are doped into the t_{2g} orbitals of $LiCoO_2$, they are dressed by electron density in the e_g orbitals and hole density on the oxygen orbitals. The mechanism of this rehybridization phenomena has been identified as a competition between the e_g-oxygen hybridization and the Co on-site coulomb repulsion. The hybridization prefers to occupy the e_g orbital while the Coulomb repulsion tends to empty the e_g orbital to avoid the on-site repulsion with the t_{2g} orbitals which are already present. As holes are doped into the t_{2g} orbitals, the system can lower its energy by increasing the hybridization given that there is less density within the t_{2g} orbitals to interact with the resulting increase in e_g density. This hypothesis was confirmed by postulating and solving a simple, modified Hubbard model which is representative of Li_xCoO_2. Additionally, we demonstrated that the presence of hybridization screens the low energy excitations of the system. These findings should qualitatively apply to any transition-metal-oxide in which holes (electrons) are being doped into the t_{2g} states. Specifically, these findings are useful in the context of hydrated Na_xCoO_2, which was recently found to be superconducting.

The second topic of this thesis was the anomalous metal-insulator transition in Li_xCoO_2. Extensive experimental work has characterized a first-order metal-insulator transition for $0.75 < x < 0.95$, with an insulating state for $x > 0.95$ and a metallic state for $x < 0.75$. However, neither the mechanism for the transition nor the mechanism for the insulating state had been determined. In this thesis, LDA supercell calculations were used to demonstrate that the Li vacancy potential binds a hole in the dilute limit and creates a Mott insulator of impurity states. This result qualitatively explains why an insulator

forms for $x > 0.95$, which was hereto unknown. Additionally, we conclude that the metal-insulator transition is associated with a decomposition of the impurity band. This transition is perhaps the first known example of a first-order Mott transition in a doped semi-conductor.

The final topic involved a five band DMFT calculation for the photoemission spectra of $LiCoO_2$. Experimental measurement of the spectra indicated that the LDA failed to reproduce a high energy satellite in the spectrum. Although this satellite was successfully captured with an empirical cluster calculation, no first-princples methods had been able to capture this. LDA+DMFT calculations were able to successfully capture the satellite. Given the important role that the empirical cluster calculations have played in understanding photoemission spectra over the last 20 years, it is promising that a (nearly) first-principles technique is now available which can capture these sorts of many-body effects.

In conclusion, the understanding of the electronic properties of Li_xCoO_2 has been furthered within this thesis. The DMFT has continued to prove itself as an invaluable tool to study strongly correlated systems, and it appears to be on its way to becoming a regular electronic structure tool.

Chapter 10

Bibliography

1 A. L. Fetter and J. D. Walecka, *Quantum theory of many-particle systems* (McGraw-Hill, San Francisco,, 1971).

2 G. D. Mahan, *Many-particle physics* (Kluwer Academic/Plenum Publishers, New York, 2000).

3 R. D. Mattuck, *A guide to Feynman diagrams in the many-body problem* (Dover Publications, New York, 1992).

4 J. W. Negele and H. Orland, *Quantum many-particle systems* (Addison-Wesley Pub. Co., Redwood City, Calif., 1988).

5 N. W. Ashcroft and N. D. Mermin, *Solid state physics* (Holt Rinehart and Winston, New York,, 1976).

6 M. Born and K. u. Huang, *Dynamical theory of crystal lattices* (Clarendon Press, Oxford,, 1968).

7 O. K. Andersen, Physical Review B (Solid State) **12**, 3060 (1975).

8 E. Wigner and F. Seitz, Physical Review **43**, 804 (1933).

9 W. Kohn, Reviews of Modern Physics **71**, 1253 (1999).

10 J. Kanamori, Prog. Theor. Phys. **30**, 275 (1963).

11 M. C. Gutzwiller, Physical Review Letters **10**, 159 (1963).

12 J. Hubbard, Proc. Roy. Soc. London **276**, 238 (1963).

13 J. Hubbard, Proc. Roy. Soc. London **281**, 401 (1964).

14 P. W. Anderson, Physical Review **124**, 41 (1961).

15 P. Hohenberg and W. Kohn, Physical Review **136**, B864 (1964).

16 W. Kohn and L. J. Sham, Physical Review **140**, A1133 (1965).

17 R. G. Parr and W. Yang, *Density-functional theory of atoms and molecules* (Clarendon Press ;Oxford University Press, Oxford [England]New York, 1989).

18 A. Georges, G. Kotliar, W. Krauth, et al., Reviews of Modern Physics **68**, 13 (1996).

19 W. Metzner and D. Vollhardt, Physical Review Letters **62**, 324 (1989).

20 M. Imada, A. Fujimori, and Y. Tokura, Reviews of Modern Physics **70**, 1039 (1998).

21 K. Held, I. A. Nekrasov, G. Keller, et al., Cond. Mat. **0112079** (2001).

22 K. Held, I. A. Nekrasov, N. Blümer, et al., Int. J. Mod. Phys. B **15**, 2611 (2001).

23 V. I. Anisimov, A. I. Poteryaev, M. A. Korotin, et al., Journal of Physics-Condensed Matter **9**, 7359 (1997).

24 V. I. Anisimov, F. Aryasetiawan, and A. I. Lichtenstein, Journal of Physics-Condensed Matter **9**, 767 (1997).

[25] F. Gebhard, *The mott metal-insulator transition : models and methods* (Springer, Berlin ; New York, 1997).
[26] D. Vollhardt, Reviews of Modern Physics **56**, 99 (1984).
[27] N. F. Mott, *Metal-insulator transitions* (Taylor & Francis, London ; New York, 1990).
[28] P. P. Edwards and M. J. Sienko, Physical Review B **17**, 2575 (1978).
[29] I. G. Austin and N. F. Mott, Advances in Physics **50**, 757 (2001).
[30] F. X. Hart and J. B. Bates, Journal of Applied Physics **83**, 7560 (1998).
[31] S. Levasseur, M. Menetrier, and C. Delmas, Journal of the Electrochemical Society **149**, A1533 (2002).
[32] D. Carlier, I. Saadoune, M. Menetrier, et al., Journal of the Electrochemical Society **149**, A1310 (2002).
[33] S. Levasseur, M. Menetrier, and C. Delmas, Chemistry of Materials **14**, 3584 (2002).
[34] S. Levasseur, M. Menetrier, E. Suard, et al., Solid State Ionics **128**, 11 (2000).
[35] D. Carlier, A. Van der Ven, C. Delmas, et al., Chemistry of Materials **15**, 2651 (2003).
[36] A. Van der Ven and G. Ceder, Electrochemical and Solid State Letters **3**, 301 (2000).
[37] A. Van der Ven and G. Ceder, Physical Review B **59**, 742 (1999).
[38] A. Van der Ven, M. K. Aydinol, G. Ceder, et al., Physical Review B **58**, 2975 (1998).
[39] A. Van der Ven, M. K. Aydinol, and G. Ceder, Journal of the Electrochemical Society **145**, 2149 (1998).
[40] M. Menetrier, I. Saadoune, S. Levasseur, et al., Journal of Materials Chemistry **9**, 1135 (1999).
[41] H. Tukamoto and A. R. West, Journal of the Electrochemical Society **144**, 3164 (1997).
[42] K. Takada, H. Sakurai, E. Takayama-Muromachi, et al., Nature **422**, 53 (2003).
[43] F. A. Cotton, *Chemical applications of group theory* (Wiley, New York, 1990).
[44] K. Terakura, T. Oguchi, A. R. Williams, et al., Physical Review B **30**, 4734 (1984).
[45] D. J. Singh, P. Blaha, K. Schwarz, et al., Physical Review B **60**, 16359 (1999).
[46] V. I. Anisimov, M. A. Korotin, M. Zolfl, et al., Physical Review Letters **83**, 364 (1999).
[47] J. Vanelp, J. L. Wieland, H. Eskes, et al., Physical Review B **44**, 6090 (1991).
[48] M. T. Czyzyk, R. Potze, and G. A. Sawatzky, Physical Review B **46**, 3729 (1992).
[49] G. A. Sawatzky, Private Communication.
[50] G. Onida, L. Reining, and A. Rubio, Reviews of Modern Physics **74**, 601 (2002).
[51] J. C. Dupin, D. Gonbeau, I. Martin-Litas, et al., Journal of Electron Spectroscopy and Related Phenomena **120**, 55 (2001).
[52] L. A. Montoro, M. Abbate, and J. M. Rosolen, Electrochemical and Solid State Letters **3**, 410 (2000).
[53] W. S. Yoon, K. B. Kim, M. G. Kim, et al., Journal of Physical Chemistry B **106**, 2526 (2002).

[54] V. R. Galakhov, E. Z. Kurmaev, S. Uhlenbrock, et al., Solid State Communications **99**, 221 (1996).
[55] V. R. Galakhov, V. V. Karelina, D. G. Kellerman, et al., Physics of the Solid State **44**, 266 (2002).
[56] G. G. Amatucci, J. M. Tarascon, and L. C. Klein, J. Electrochem. Soc. **143**, 1114 (1996).
[57] J. Molenda, A. Stoklosa, and T. Bak, Solid State Ionics **36**, 53 (1989).
[58] D. Carlier, Private Communication.
[59] N. Imanishi, M. Fujiyoshi, Y. Takeda, et al., Solid State Ionics **118**, 121 (1999).
[60] M. Abbate, R. Potze, G. A. Sawatzky, et al., Physical Review B **49**, 7210 (1994).
[61] S. Sugano, Y. Tanabe, and H. Kamimura, *Multiplets of transition-metal ions in crystals* (Academic Press, New York,, 1970).
[62] C. Fouassier, C. Delmas, and P. Hagenmuller, Materials Research Bulletin **10**, 443 (1975).
[63] I. Terasaki, Y. Sasago, and K. Uchinokura, Physical Review B **56**, 12685 (1997).
[64] F. C. Zhang and T. M. Rice, Physical Review B **37**, 3759 (1988).
[65] C. Honerkamp, Physical Review B **68** (2003).
[66] B. Kumar and B. S. Shastry, Physical Review B **68** (2003).
[67] Q. Wang, D. Lee, and P. A. Lee, Cond. Mat. **0304377** (2003).
[68] D. J. Singh, Physical Review B **68**, 020503 (2003).
[69] D. J. Singh, Physical Review B **61**, 13397 (2000).
[70] G. Kresse and J. Furthmuller, Computational Materials Science **6**, 15 (1996).
[71] G. Kresse and J. Furthmuller, Physical Review B **54**, 11169 (1996).
[72] G. Kresse and D. Joubert, Physical Review B **59**, 1758 (1999).
[73] P. E. Blochl, Physical Review B **50**, 17953 (1994).
[74] J. W. Lynn, Q. Huang, C. M. Brown, et al., Cond. Mat. **0307263** (2003).
[75] J. D. Jorgensen, M. Avdeev, D. G. Hinks, et al., Cond. Mat. **0307627** (2003).
[76] P. W. Anderson, Science **235**, 1196 (1987).
[77] C. Umrigar, D. E. Ellis, D. Wang, et al., Physical Review B **26**, 4935 (1982).
[78] C. Wolverton and A. Zunger, Physical Review Letters **81**, 606 (1998).
[79] J. E. Hirsch, Physical Review B **28**, 4059 (1983).
[80] J. E. Hirsch and R. M. Fye, Physical Review Letters **56**, 2521 (1986).
[81] P. P. Edwards, C. N. R. Rao, and N. F. Mott, *Metal-insulator transitions revisited* (Taylor & Francis, London, UK ; Bristol, PA, USA, 1995).
[82] P. P. Edwards and C. N. R. Rao, *The metallic and nonmetallic states of matter* (Taylor & Francis, London ; Philadelphia, 1985).
[83] N. F. Mott, *Metal-insulator transitions* (Taylor & Francis; Barnes & Noble Books, London, New York, 1974).
[84] Z. H. Chen, Z. H. Lu, and J. R. Dahn, Journal of the Electrochemical Society **149**, A1604 (2002).
[85] H. Gabrisch, R. Yazami, and B. Fultz, Electrochemical and Solid State Letters **5**, A111 (2002).
[86] J. Graetz, A. Hightower, C. C. Ahn, et al., Journal of Physical Chemistry B **106**, 1286 (2002).
[87] J. N. Reimers and J. R. Dahn, Journal of the Electrochemical Society **139**, 2091 (1992).

[88] T. Ohzuku and A. Ueda, Journal of the Electrochemical Society **141**, 2972 (1994).
[89] G. G. Amatucci, J. M. Tarascon, and L. C. Klein, Journal of the Electrochemical Society **143**, 1114 (1996).
[90] C. Kittel, *Introduction to solid state physics* (Wiley, New York, 1996).
[91] M. K. Aydinol, A. F. Kohan, G. Ceder, et al., Physical Review B **56**, 1354 (1997).
[92] C. A. Marianetti, G. Kotliar, and G. Ceder, Cond. Mat. **0312514** (2003).
[93] M. H. Hettler, M. Mukherjee, M. Jarrell, et al., Physical Review B **61**, 12739 (2000).
[94] G. Biroli and G. Kotliar, Physical Review B **65** (2002).
[95] S. Biermann, F. Aryasetiawan, and A. Georges, Physical Review Letters **90** (2003).
[96] P. Sun and G. Kotliar, Physical Review B **66** (2002).
[97] V. Dobrosavljevic, A. A. Pastor, and B. K. Nikolic, Europhysics Letters **62**, 76 (2003).
[98] N. F. Mott, Canad. J. Phys. **34**, 1356 (1956).
[99] A. Fujimori and F. Minami, Physical Review B-Condensed Matter **30**, 957 (1984).
[100] S. Y. Savrasov, Physical Review B **54**, 16470 (1996).